DTU Nanotech
Department of Micro- and Nanotechnology

Bachelor Thesis

Theory of Electrokinetic Effects in Nanofluidic Channels

Kristian Lund Jensen
s072164

Jesper Toft Kristensen
s061645

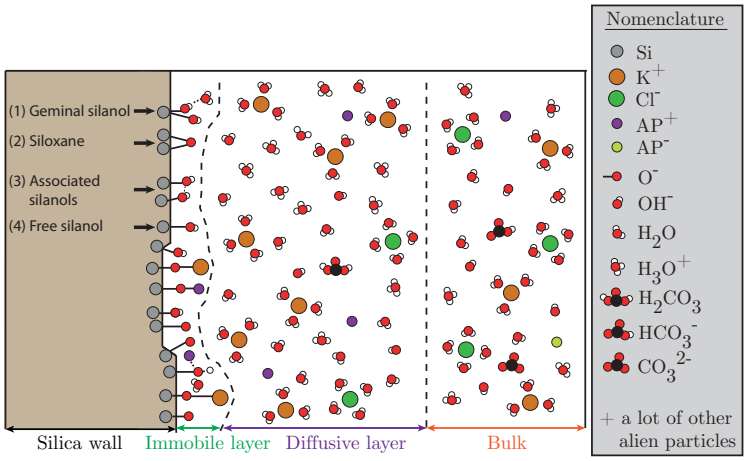

Supervisor: Henrik Bruus

Department of Micro- and Nanotechnology
Technical University of Denmark

21 June 2010

The picture on the front page shows a sketch of a silica wall contacting an electrolyte.

Abstract

In this thesis we develop two solid/liquid interface models for calculating the ζ potential and surface charge density in a silica nanochannel contacting an aqueous salt solution. We generalize the models to include an arbitrary number of solutes and be valid for diffusive layer overlap in a high aspect ratio silica nanochannel. We use one of the models to calculate the conductance versus salt concentration of a nanochannel, and show that it is essential to include the inherent ions in the water together with absorbed CO_2 for low salt concentrations. This has not been seen in any previous solid/liquid interface model used for conductance calculations. We are the first to show a model that predicts a conductance which can be characterized by four regimes: the bulk regime, departure, valley, and plateau. We will show that for low KCl bulk concentrations in a bare silica nanochannel the fixed concentration of inherent hydrons dominates the conductance. We show how to expand our models to account for coated silica surfaces which has not been done before. Furthermore, we investigate how the conductance depends on aminosilane coverage. We fit one of our models to experimental conductance data for a bare silica nanochannel and find good correlation. From the fit we determine the dissociation constant for the deprotonation of free silanol surface groups and obtain a value within 3% of the literature value.

Resumé

I denne afhandling udvikler vi to overflademodeller til beregning af ζ potentialet og overfladeladningstætheden i en silika nanokanal i kontakt med en vandig saltopløsning. Vi generaliserer modellerne så de kan inkludere et arbitrært antal opløste stoffer og er gyldige for overlap af de diffusive lag i en silika nanokanal med højt dimensionsforhold. Vi beregner konduktansen mod salt koncentrationen af en nanokanal og viser at det er essentielt at inkludere de naturligt forekommende hydrogen ioner i vandet samt optagelse af CO_2 fra luften for lave salt koncentrationer. Dette er ikke set før i litteraturen og vi er de første til at vise en model, der forudsiger en konduktans, der kan karakteriseres ved fire regimer: Volumen-, fravigelses-, dal- og plateau-regimet. Vi demonstrerer at konduktansen for lave KCl salt koncentrationer i en bar silika nanokanal er domineret af de naturligt forekommende hydrogen ioner. Vi viser hvordan man udvider vores modeller til at tage højde for belægning af aminosilan på silika overflader hvilket ikke er blevet gjort før. Endvidere undersøger vi hvordan konduktansen afhænger af belægningsgraden af aminosilan. Gennem parameterjustering tilpasser vi en af vores modeller til eksperimentelle konduktansdata for en bar silika nanokanal og finder gode overensstemmelser mellem model og forsøg. Fra parameterjusteringen bestemmer vi dissociationskonstanten for deprotonisering a frie silanol ovarfladegrupper og opnår en værdi, der ligger indenfor 3% af literaturværdien.

Preface

The present thesis is submitted as fulfillment of the prerequisites for obtaining the B.Sc. Eng. in Physics and Nanotechnology degree at the Technical University of Denmark (DTU). The work has been carried out at the Department of Micro- and Nanotechnology (DTU Nanotech) in the Theoretical Microfuidics Group (DTU–TMF group) headed by Prof. Henrik Bruus. The duration of this 15 ECTS credits project for each student is a 5 month period from February 2010 to June 2010.

The research was conducted under supervision of DTU Prof. Henrik Bruus at the University of California, Santa Barbara (UCSB) as Prof. Henrik Bruus was on sabbatical visiting the UCSB Nanolab at the Department of Mechanical Engineering. We are deeply grateful to Dr. Sumita Pennathur for letting us become a part of the UCSB Nanolab and helping us during our stay even though she hardly knew us before our arrival to UCSB. We wish to thank everyone in the UCSB Nanolab for making our stay unforgettable and being such great lab-buddies. It has truly been a unique experience to work (and almost live) in the lab surrounded by fantastic people. Specifically from the Nanolab we would like to thank Alex Russell, Andrew Crumrine, David A. Herrick, David Boy, Francesco Bonotto, Jared Frey, Jess Sustarich, Mariateresa Napoli, Nolan Pasko, Sumita Pennathur, Tom Wynne, Trent Huang, and the rest of this amazing group. Furthermore, our theoretical work would not have been of the same value without the experimental data from David A. Herrick and Andrew Crumrine, who both have worked countless hours in the lab obtaining it. We thank Tom Wynne for being patient with us during our many lab discussions and for bringing us along on a hike in the mountains of Santa Barbara.

We are deeply appreciative to our TMF group consisting of BS student Christian Laut Ebbesen, Prof. Henrik Bruus aka. California Rick aka. Enrico Spumante, MS student Kasper Kristensen, PhD student Mathias Bækbo Andersen, MS student Mikkel Settnes, PhD student Rune "Dick" Barnkob, PhD student Søren "BS Chuck" Vedel, and the rest of this wonderful group for educating group meetings on the highest level and many wonderful laughs during the stay including our weekly visits at the beach side bar. We thank Mathias Bækbo Andersen for our many valuable discussions and for lending us some of his MatLab code so we could finish the project in time. We are deeply thankful for being allowed to live in the TMF house on the Bækbo-grant in the last 2-3 weeks of our project which served as a monastery in a critical time.

We wish to thank Prof. Henrik Bruus for showing us around in the city of San Francisco and Kasper Kristensen for making the trip to Los Angeles happen, both were unforgettable visits — we'll be back! We thank the restaurants and cafees of Isla Vista for great food, coffee, and environment during the writing process. We recognize that this thesis would not have been anything at all without the great Prof. Henrik Bruus who was a extraordinary mentor and the best guide for us in many ways. His profound understanding of physics and pedagogical ways of teaching have been deeply embedded in us for the rest of our lives. Finally, we wish to express our profound gratitude and love to our families for support and missing us during our stay.

Due to demands from the Danish Ministry of Education, we are required to write who is responsible for which parts of the thesis. Kristian is responsible for the even pages and Jesper for the odd pages.

Kristian Lund Jensen
Silvergreens in Isla Vista
University of California, Santa Barbara
California, 20 June 2010

Jesper Toft Kristensen
Silvergreens in Isla Vista
University of California, Santa Barbara
California, 20 June 2010

Contents

List of Figures

List of Tables

List of Symbols

Symbol	Description	Unit
$\partial_i = \frac{\partial}{\partial x_i}$	Partial derivative after ith co-ordinate	
$\boldsymbol{\nabla}$	Nabla or gradient operator	
$\boldsymbol{\nabla}\cdot$	Divergence operator	
$\boldsymbol{\nabla}\times$	Rotation operator	
∇^2	Laplace operator	
$\cdot$	Scalar product	
$\times$	Multiplication sign	
$\ln(\cdot)$	Natural logarithm function	
$\log_{10}(\cdot)$	Logarithm function of base 10	
$\mathrm{sgn}(\cdot)$	Signum function	
$\ll$	Much smaller than	
$\gg$	Much greater than	
$\sim$	Of the same order	
$\approx$	Approximately equal to	
$\equiv$	Equivalent by definition	
$\propto$	Proportional to	
$\mathbf{0}$	Zero vector	
a_i	Activity of ith ion	
a_i^j	Activity of ith ion in the jth plane	
$\mathbf{B}$	Magnetic flux density	T
c_i	Actual concentration of ith specie	m^{-3}
c_i^{b}	Actual bulk concentration of ith specie	m^{-3}

Continued on next page

Continued from previous page

Symbol	Description	Unit
c_*^{b}	Charge molarity of ions in bulk	m^{-3}
$c_i^{\max}$	Largest possible actual concentration of ith specie	m^{-3}
c_{X}	Formal concentration of the acid X	m^{-3}
$c_{\mathrm{X},z}$	Concentration of X^z	m^{-3}
C_1, C_2	Inner and outer Stern capacitance	$\mathrm{F\ m}^{-2}$
C_{s}	Stern capacitance	$\mathrm{F\ m}^{-2}$
$\mathbf{D}$	Electric flux density	$\mathrm{C\ m}^{-2}$
e	Elementary charge	C
$\mathbf{E}$	Electric field	$\mathrm{V\ m}^{-1}$
$\mathbf{E}_{\mathrm{ext}}$	External electric field	$\mathrm{V\ m}^{-1}$
F	Faraday's constant	$\mathrm{C\ mol}^{-1}$
$\mathbf{F}$	Force	N
$\mathbf{g}$	Gravitational acceleration	$\mathrm{N\ kg}^{-1}$
G	Gibbs free energy	J
h	Height in a nanochannel	m
H	Height in a microchannel	m
$\mathbf{H}$	Magnetic field strength	$\mathrm{A\ m}^{-1}$
$I_{\mathrm{adv}}, I_{\mathrm{mig}}$	Advection and electromigration current	A
$\mathcal{I}$	Ionic strength	m^{-3}
$\mathbf{J}_{\mathrm{el}}$	Electric current density	$\mathrm{A\ m}^{-2}$
$\mathbf{J}_{\mathrm{adv}}, \mathbf{J}_{\mathrm{mig}}$	Advection and electromigration current density	$\mathrm{A\ m}^{-2}$
k_{B}	The Boltzmann constant	$\mathrm{J\ K}^{-1}$
k_{K}	The Kohlrausch coefficient	$\mathrm{S\,m}^{-1}\,\mathrm{M}^{-3/2}$
K_i	Equilibrium constant of ith reaction	
K_{w}	Self-ionization constant of water	M^2

Continued on next page

Continued from previous page

Symbol	Description	Unit
L	Length of channel	m
MARD	Mean absolute relative difference	
N	Absolute value of valence	
N_A	Avogadro's number	mol^{-1}
$\mathcal{N}$	Number of ions or ion pairs	
pH	Acidity of solution	
$\mathrm{pH_b}$	Acidity of bulk solution	
$\mathrm{pH_o}$	Acidity of solution at the o-plane	
$\langle \mathrm{pH} \rangle_i$	Weighted pH of the ith particle	
$\mathrm{p}K_i$	$-\log_{10}(K_i)$	
$\mathbf{P}$	Polarization	$\mathrm{C\ m}^{-2}$
PZC	pH where silica surface has zero charge density	
q	Charge	C
$\mathbf{r}$	Position vector	m
$S_\mathrm{adv}, S_\mathrm{mig}, S_\mathrm{tot}$	Advection, electromigration, and total conductance	Ω^{-1}
$S_\mathrm{bulk}, S_\mathrm{bulk}^\mathrm{KCl}$	Bulk conductance and KCl bulk conductance	Ω^{-1}
t	Time	s
T	Temperature	K
v, $\mathbf{v}$	Scalar velocity and velocity vector	$\mathrm{m\ s}^{-1}$
w	Channel width	m
x, y, z	Cartesian co-ordinates	m
X^z	Charge state of family X with valence z	
Z_i, Z_coat	Valence of ith ion and valence of coated site	
α_ion	Effective ion size	m
α_bl	Number of free silanols blocked, including the coated site, by a coating molecule	

Continued on next page

Continued from previous page

Symbol	Description	Unit
β	Dimensionless viscosity ratio	
γ_i	Activity coefficient of ith specie	
Γ_i, Γ_{tot}	Density of ith site state, total number of chargeable sites	m^{-2}
δ	Surface charge density	$\mathrm{C\ m}^{-2}$
$\delta_{\mathrm{o}}, \delta_{\beta}, \delta_{\mathrm{d}}$	Surface charge density in the o-, β-, and d-plane, respectively	$\mathrm{C\ m}^{-2}$
ϵ, ϵ_0	Electric permittivity	$\mathrm{F\ m}^{-1}$
ϵ_{r}	Relative electric permittivity	
ζ,ζ_{c}	Zeta potential and critical zeta potential	V
η	Dynamic viscosity	Pa s
θ_i	Surface coverage of ith site state	
θ_{coat},θ_{amin}	Surface coverage of coated sites and aminosilane	
Ω	Region of interest	
$\partial\Omega$	Surface of the region of interest	
λ_{D}	Debye length	m
λ_{D}^*	Standard Debye length	m
Λ	Equivalent conductivity	$\mathrm{S\ m}^{-1}\ \mathrm{M}^{-1}$
Λ_{o}	Equivalent conductivity at infinite dilution	$\mathrm{S\ m}^{-1}\ \mathrm{M}^{-1}$
μ	Chemical potential	J
μ_i	Mobility of ith ion	$\mathrm{m}^2\ \mathrm{V}^{-1}\ \mathrm{s}^{-1}$
ρ	Mass density	$\mathrm{kg\ m}^{-3}$
ρ_{el}	Electric charge density	$\mathrm{C\ m}^{-3}$
σ_{el}	Electric conductivity	$\mathrm{S\ m}^{-1}$
ϕ	Electric potential	V
$\phi_{\mathrm{ext}}, \phi_{\mathrm{int}}$	External and internal electric potential	V
ϕ_{m}	Electric potential in mid channel	V
$\phi_{\mathrm{o}}, \phi_{\beta}, \phi_{\mathrm{d}}$	Electric potential in the o-, β-, and d-plane, respectively	V

Chapter 1

Introduction

1.1 Nanofluidics

Nanofluidics is typically defined as the study of fluids in structures with one or more dimensions in the range 0–100 nm [1]. It is a much younger field compared to microfluidics, but the theory central to the nanofluidic field originates from well-established fields such as colloidal and interface sciences. The Nanoscale Device Laboratory known as the Nanolab is a part of the Mechanical Engineering Department at University of California, Santa Barbara (UCSB) under the direction of Dr. Sumita Pennathur. The experimental work of this thesis is carried out in the UCSB Nanolab. The UCSB Nanolab primarily focuses on applications of nanofluidics in biological engineering applications where the small dimensions in nanochannels are a big advantage primarily since it allows for very small sampling volumes, it gives very low diffusion times, and the reaction kinetics are enhanced when compared to e.g microchannels. Furthermore, nanofluidics shows promising prospects in converting hydrostatic energy into electrical energy which we will refer to as energy harvesting [2, 3]. Applications have been proposed which can convert the pressure created in each step from walking into energy charging a mobile device. For a review of energy applications for nanofluidics we recommend Ref. [4]. In nanochannels the surface to volume ratio is large, so in order to engineer them it is essential to understand the physics governing the surface. Specifically, the surface charge density and surface potential, the latter known as the ζ potential, are parameters determining the behavior of the channels by affecting the liquid ions inside them. In this thesis our focus will be on an electrical characterization of nanochannels through a theoretical study and it will lead to the determination of the ζ potential and surface charge density by measuring the conductance of the nanochannel. This thesis will mainly be theoretical and the concrete system in our study will be a silica nanochannel filled with KCl solution.

In our work we will focus on high aspect ratio rectangular silica nanochannels where the height is much smaller than the width of the channel $h \ll w$. It requires very high pressures to drive a liquid through a nanochannel because the flow rate Q_{p} scales linearly with the

applied pressure Δp and with the cube of the height h

$$Q_{\mathrm{p}} \propto \frac{h^3 w}{L} \Delta p, \quad h < w, \tag{1.1}$$

where L is the channel length. Reducing the height with an order of magnitude requires the pressure to increase with 3 orders of magnitude to maintain the same flow rate. Therefore, other methods are used to drive the liquid through a nanochannel one of which is the electrokinetic phenomenon electro-osmosis which provides the flow rate

$$Q_{\mathrm{eo}} \propto \frac{hw}{L} \Delta V, \quad \lambda_{\mathrm{D}} \ll \frac{h}{2}, \tag{1.2}$$

where ΔV is an externally applied electric potential and λ_{D} is the Debye screening length, a central length parameter in nanofluidics to be defined later. The example shows how electrokinetics which is the main subject of this thesis is of great interest in nanochannels.

When a silica nanochannel surface contacts an aqueous solution the SiOH surface groups react with the hydrons in the water. They either deprotonate to create negative SiO^- sites or become protonated creating SiOH_2^+ sites. The large surface to volume ratio makes it essential to understand the nanochannel surface in terms of charge and potential since everything else can be derived from these. A theoretical description of the surface in terms of chemical reactions is done by Charmas *et al.* for a silica surface in Ref. [5]. The bulk composition of the solution is important because it influences the nanochannel system through ionic strength and pH which are both determining for the chemical equilibrium reactions of the surface. Persat *et al.* [6] provide the theory of how to calculate the composition of a solution with an arbitrary number of solutes being either acids, bases, or salts.

1.2 Overview of Solid/Liquid Interface Models

We will here give an overview of how the model of a surface contacting a liquid was perceived through history. For a thorough discussion on the general historical development of electrokinetic phenomena we recommend Ref. [7]. The first important theoretical approach toward describing the observed electrokinetic phenomena in channels was by Hermann von Helmholtz in 1879 who introduced a rigid layer of adsorbed counterions in a particular distance from the surface. This allowed him to model the ions in the wall together with the counterions as a capacitor as shown in Fig. 1.1(a). Later, the model independently introduced by Louis–Georges Gouy in 1910 and David Leonard Chapman in 1913 introduced the concept of a diffusive screening layer, also known as the Debye layer, but with no capacitor as shown in Fig. 1.1(b). Neither of these approaches alone predicted the right outcome of experiments until Stern in 1924 [8] combined the two models into the Gouy–Chapman–Stern model shown in Fig. 1.1(c) where an immobile monoatomic layer, also known as the Stern layer, of screening ions is modeled as a capacitor. Stern then used the Gouy–Chapman diffusive theory to describe the counterion distribution away from the immobile layer. The Gouy–Chapman–Stern model is today the most common in describing

a surface contacting an electrolyte. It is common to refer to these models in terms of the number of planes, or layers, parallel to the surface where charge can reside. Therefore, the Gouy–Chapman–Stern model is a two-layer model. We will build our theory using the Gouy–Chapman–Stern model approach.

When the aqueous solution next to the surface consists of a high concentration of metal cations such as Na^+ or K^+ the Gouy–Chapman–Stern model was in the mid 1970's refined based on ideas of Yates *et al.* [9] and Chan *et al.* [10] to the metal adsorption model also known as the triple-layer model shown in Fig. 1.1(d). This model introduced a layer (layer 3) inside the immobile region where adsorbed metal cations could reside.

In 1980 the four-layer model was developed by Bowden *et al.* [11, 12] who used layer 3 for the adsorption of doubly ionized metal cations such as Ca^{2+}. The singly ionized cations and anions were situated in a new layer (layer 4). Then, Bousse *et al.* [13] used the same four layer model on a singly ionized electrolyte now to account for the difference in adsorption distance between cations (layer 3) and anions (layer 4) from the silica surface. With beginning in 1995 a series of papers were introduced by Charmas *et al.* with the goal of developing a full thermodynamic description of the four-layer model. The first paper in the series [5] stated the governing equations for the triple-layer model and the four-layer model in general condensed forms obtained from previous work which we adopt in our thesis and modify to fit our system.

Throughout this thesis the word electrolyte will be taken to mean any particle or collection of particles with a nonzero charge. The individual ions in an aqueous solution as well as the solution itself are thus both electrolytes.

In Appendix B we provide all parameters used for the numerical calculations and generation of the plots in the thesis. Finally, we have focused on explaining the physics rather than engulfing the reader in numerical details. Therefore, in Appendix C we provide all the MatLab scripts with detailed comments central to our work and we will be referring to them as we go along.

1.3 Outline of Thesis

Chapter 2: Basic Electrokinetic Theory

In this chapter we will state the governing equations for a nanochannel system. We will introduce the ζ potential and derive the general Grahame equation expressing the surface charge density.

Chapter 3: Chemical Models of Bulk and Surfaces

In this chapter we start out by discussing how to calculate the solute concentrations of all

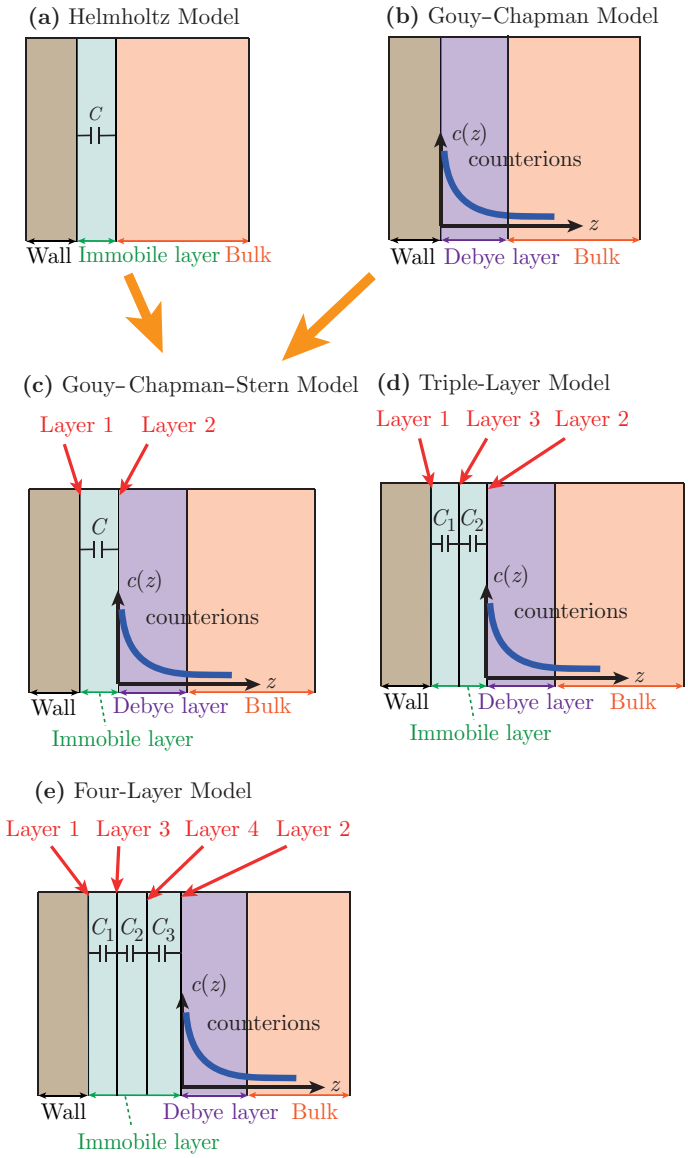

Figure 1.1: The theory of a surface contacting an electrolyte in different historical versions. The figures are indexed consistently with their historical appearance in literature. **(a)** shows the Helmholtz model from 1879. The wall (brown) contacts an electrolyte creating an immobile layer (green) modeled as a capacitor. Next to the immobile layer is the bulk region (orange). **(b)** shows the Gouy–Chapman model first introduced in 1910. The wall (brown) contacts an electrolyte creating a diffusive layer, also known as the Debye layer, of elevated counterion concentration (purple). Next to this layer is the bulk (orange). The two orange arrows pointing toward **(c)** indicates that the Gouy–Chapman–Stern model is a fusion of **(a)** and **(b)**. **(d)** and **(e)** show the triple-layer model and four-layer model, respectively. The red arrows identify and label the planes where charge can reside.

species dissolved in an aqueous solution. We introduce the concept of pH and we discuss how to account for CO_2 absorption in an aqueous solution. We move on to discussing which assumptions are used when modeling a silica surface contacting an electrolyte and derive the 2pK-model together with the metal adsorption model. We will show how to implement coating of silica nanochannels in our models and how the potentials, surface charge densities, and coverages calculated from the metal adsorption model depend on pH. Finally, we study how the pH varies transverse to negatively charged walls in a nanochannel and define the weighted pH.

Chapter 4: Electrical Conductance of Nanochannels

In this chapter we will derive the conductance of a rectangular nanochannel and calculate it numerically for various KCl salt concentrations using the 2pK-model. We will characterize the conductance by four regimes: the bulk regime, departure, valley, and plateau. We will explain the shape of the conductance curve from the concentration profiles inside the nanochannel and study which surface related parameters in the 2pK-model are most relevant with respect to being used as fitting parameters. Finally, we will calculate how aminosilane coating of the silica surface changes the conductance of a nanochannel.

Chapter 5: Characterization of the Silica Nanochannel Surface by Conductance Measurements

In this chapter we describe how to experimentally measure the conductance of a nanochannel. Then we will fit the conductance calculated by the 2pK-model to experimental data provided by two experimentalists from the UCSB Nanolab. Finally, we discuss the fitting results.

Chapter 6: Conclusion and Outlook

In this chapter we draw the conclusions of our work and present an outlook for future studies of how to characterize the silica nanochannel surface using the theory developed in this thesis.

Chapter 2

Basic Electrokinetic Theory

In the present chapter the necessary theoretical framework for an electrohydrodynamic approach to nano- and microfluidic systems will be established by introducing the governing equations of fluid mechanics, electrodynamics and statistical physics. In Appendix A.1 we use the theory developed in this chapter in a basic study of an electrolyte at arbitrary ionic strength interacting with a containing wall.

In Fig. 2.1(a) a micro- and a nanochannel are seen connected to a reservoir containing an aqueous electrolyte solution. A horizontal xy co-ordinate system has been defined in the far right of the figure. For each channel the origin of the third co-ordinate z, transverse to the flow direction, is taken to be symmetrically placed midways between the lower and upper bounding channel walls. The cross-sections of the micro- and nanochannel dubbed sec. A-A and sec. B-B, respectively, can be seen in Fig. 2.1(b). The cross-sections show typical concentration profiles for anions and cations and potential distributions in the transverse dimension z together with channel-defining parameters. The micro- and nanochannel have height H and h, respectively. For the microchannel, and what is generally characteristic for channels with a large smallest dimension, the concentration profiles and the potential profile drop to bulk levels in the middle of the channel. The bulk levels are mathematically referred to as infinity. In the nanochannel the potential profile and hence the concentration profiles are elevated from their bulk values in the middle of the channel due to the confinement.

2.1 Governing Equations

Throughout this thesis it is assumed that the continuum hypothesis is valid. It states that the macroscopic properties of a fluid are the same if the fluid were perfectly continuous in structure. Since the fluidic channel widths used in todays research have already approached 10 nm it is worth discussing this continuum approach. Ref. [1] shows that the smallest system dimension allowable for a continuous description is ~ 3 nm. The smallest dimension in this thesis is one order of magnitude higher than this so we consider the continuum hypothesis valid. When stating the relevant equations the Eulerian picture of the fluid

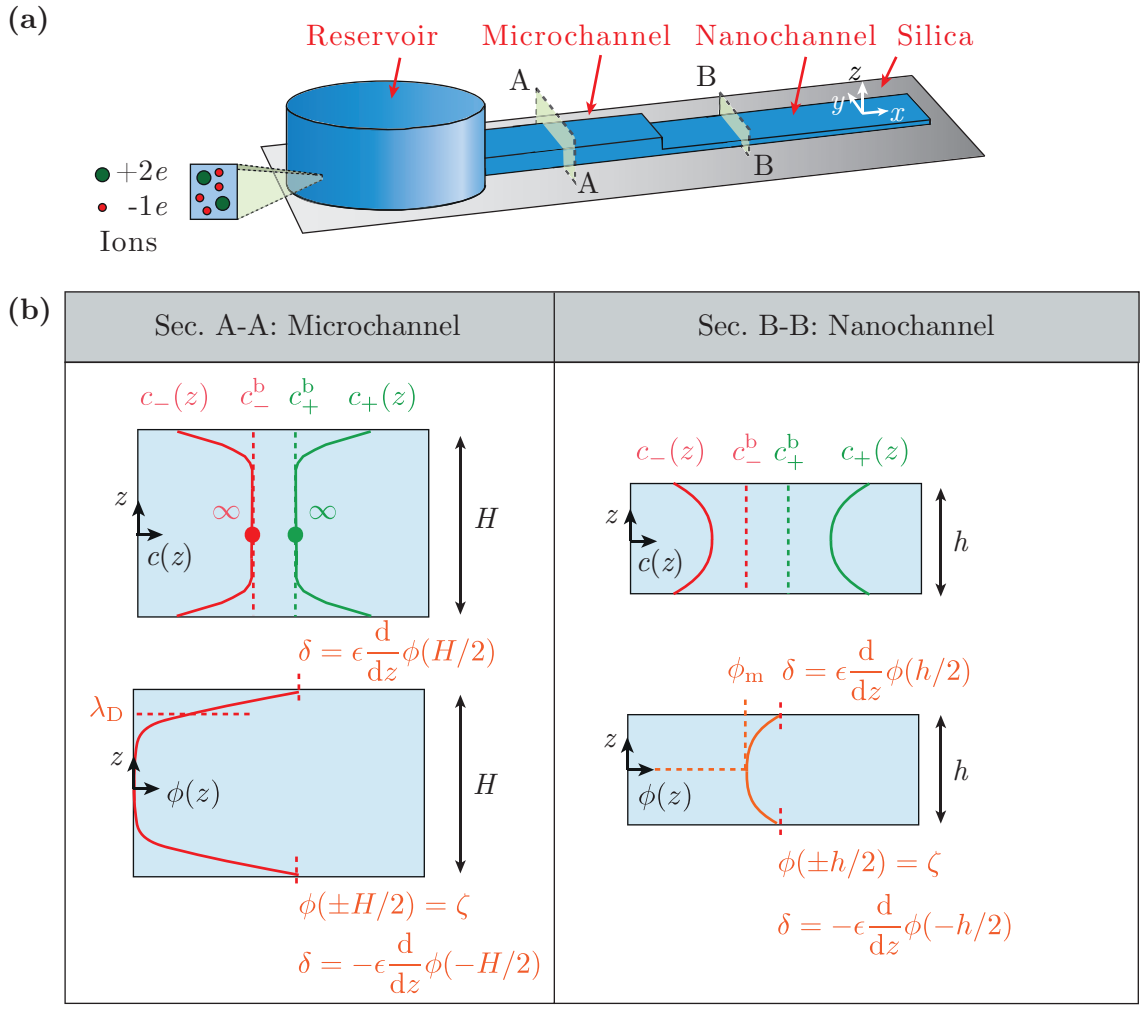

Figure 2.1: **(a)** a sketch of a reservoir, microchannel, and nanochannel all placed on a silica substrate. The xy-plane is defined in the far right of the figure and for each channel the origin of the third co-ordinate z, transverse to the flow direction, is taken to be symmetrically placed midways between the lower and upper bounding channel walls. Two cross-sections: sec. A-A and sec. B-B of the microchannel and nanochannel, respectively, have been highlighted. **(b)** shows the cross-section for the microchannel (left, sec. A-A) and the nanochannel (right, sec. B-B). For each channel a cross-section of typical concentration profiles (top) for co-ions (red) and counterions (green) have been shown together with the electric potential profile (bottom). $c_+(z)$ and $c_-(z)$ are the concentrations of the cation and anion in the channel, respectively. c_+^b and c_-^b are the concentrations of the cation and anion in the bulk, respectively. The figure shows the parameters: $c_\pm(z), c_\pm^b, \lambda_D, \delta, \zeta$, and ϕ_m.

will be adopted, where a certain domain of interest is spatially fixed and the temporal development of the fluid is described. With these assumptions in place the governing equations are ready to be introduced.

2.1.1 The Continuity Equation

Assuming that a given compressible fluid cannot spontaneously generate and/or lose mass in the interior of the domain delineating it at any given time the continuity equation, expressing mass conservation, reads

$$\partial_t \rho(\mathbf{r}, t) = -\boldsymbol{\nabla} \cdot \big[\rho(\mathbf{r}, t)\mathbf{v}(\mathbf{r}, t)\big], \tag{2.1}$$

where $\rho(\mathbf{r}, t)$ is the mass density of the fluid at the spatial point $\mathbf{r}$ at time t and $\mathbf{v}(\mathbf{r}, t)$ the velocity field of the fluid. For an incompressible fluid its density in both time and space can be assumed constant and thus Eq. (2.1) becomes

$$\boldsymbol{\nabla} \cdot \mathbf{v}(\mathbf{r}, t) = 0. \tag{2.2}$$

The explicit spatial and temporal dependence notation will be suppressed throughout the thesis and used only when necessary.

2.1.2 The Electrodynamic Equations

Assuming any present current to be weak and slowly varying in time both the magnetic field strength $\mathbf{H}$ and the magnetic flux density $\mathbf{B}$ can be neglected,

$$\boldsymbol{\nabla} \cdot \mathbf{D} = \rho_{\text{el}}, \tag{2.3a}$$
$$\boldsymbol{\nabla} \times \mathbf{E} = \mathbf{0}, \tag{2.3b}$$
$$\mathbf{D} = \epsilon_0 \mathbf{E} + \mathbf{P} = \epsilon \mathbf{E}, \tag{2.3c}$$
$$\mathbf{J}_{\text{el}} = \sigma_{\text{el}} \mathbf{E} \quad \text{(Ohm's law)}, \tag{2.3d}$$
$$\mathbf{F} = q\mathbf{E} \quad \text{(Lorentz's force law)}, \tag{2.3e}$$

where $\mathbf{D}$, ρ_{el}, $\mathbf{E}$, ϵ_0, $\mathbf{P}$, ϵ, $\mathbf{J}_{\text{el}}$, σ_{el}, $\mathbf{F}$, and q are the electric displacement field, the free spatial charge density, the electric field, the electric permittivity of vacuum, the polarization field, the electric permittivity, the electric current density, the electric conductivity, the electric force, and the charge, respectively. It is noted that since the rotation of $\mathbf{E}$ is zero the field itself is conservative and can be written as the gradient of some scalar potential function, here the electric potential ϕ,

$$\mathbf{E} = -\boldsymbol{\nabla}\phi. \tag{2.4}$$

For a homogeneous liquid the permittivity tensor is a constant scalar ϵ and we get the Poisson equation,

$$\nabla^2 \phi(\mathbf{r}) = -\frac{1}{\epsilon} \rho_{\text{el}}(\mathbf{r}). \tag{2.5}$$

2.1.3 The Navier–Stokes Equation

The Navier–Stokes equation for an incompressible fluid in an electric field reads,

$$\rho\left[\partial_t \mathbf{v} + (\mathbf{v}\cdot\boldsymbol{\nabla})\,\mathbf{v}\right] = -\boldsymbol{\nabla} p + \eta\nabla^2\mathbf{v} + \rho\mathbf{g} + \rho_{\mathrm{el}}\mathbf{E}, \tag{2.6}$$

where $\rho\partial_t\mathbf{v}$ is the local acceleration, $\rho\,(\mathbf{v}\cdot\boldsymbol{\nabla})\,\mathbf{v}$ the advective acceleration, $-\boldsymbol{\nabla}p$ the pressure gradient force, $\eta\nabla^2\mathbf{v}$ the viscous force due to shear stress, $\rho\mathbf{g}$ the gravitational force density and $\rho_{\mathrm{el}}\mathbf{E}$ the electric force density. The term $\beta\eta\boldsymbol{\nabla}\,(\boldsymbol{\nabla}\cdot\mathbf{v})$ has been dropped as the fluid is incompressible. This will be the general way of stating the Navier–Stokes equation in the chapters to follow.

2.1.4 The Chemical Potential

Modeling the solute ions in a given low-concentration electrolyte contained in a control volume as an ideal gas, statistical mechanics provides an equation describing the differential change in free energy from an incremental addition of an ion. In the case where the free energy in question is Gibbs free energy G the chemical potential μ is formally defined as

$$\mu \equiv \left(\frac{\partial G}{\partial \mathcal{N}}\right)_{T,p}, \tag{2.7}$$

where the temperature T and the pressure p are kept constant. For the purposes of presenting the fundamental equations it will be assumed that the fluid is made up of only one electrolyte with opposite valences $\pm N$ with N thus defined as always being a positive integer. In this case it can be shown that the chemical potential for both the negative and positive ionic concentrations at a spatial point $\mathbf{r}$ can be compactly written as,

$$\mu_{\pm}(\mathbf{r}) = \mu_{0,\pm} + k_{\mathrm{B}}T\ln\left(\frac{c_{\pm}(\mathbf{r})}{c_{\mathrm{o}}}\right) \pm Ne\phi(\mathbf{r}), \tag{2.8}$$

where $\pm$ refers to positive and negative ions, respectively, and where c_{o} and $\mu_{\mathrm{o},\pm}$ are the concentration and chemical potential, respectively, which would be present without the potential $\phi(\mathbf{r})$. k_{B}, $c_{\pm}(\mathbf{r})$, and e are the Boltzmann constant, the concentration of the ion at point $\mathbf{r}$, and the elementary charge, respectively.

2.1.5 The Poisson–Boltzmann Equation

In thermodynamic equilibrium the chemical potentials $\mu_{\pm}$ must be constant throughout the system, since otherwise, the system would be able to reduce its Gibbs free energy by reorganizing its constituents contradicting the state of equilibrium. Therefore we have

$$\boldsymbol{\nabla}\mu_{\pm}(\mathbf{r}) = \mathbf{0}, \tag{2.9}$$

and Eq. (2.8) becomes

$$k_{\mathrm{B}}T\boldsymbol{\nabla}\ln\left(\frac{c_{\pm}(\mathbf{r})}{c_{\mathrm{o}}}\right) = \mp Ne\boldsymbol{\nabla}\phi(\mathbf{r}). \tag{2.10}$$

One way of solving the equation is to approximate the wall of the chamber as being an infinite planar wall which occupies the half-space $z < 0$. The potential at the wall is known as the ζ potential. At infinity, assume that the potential decays to zero, that is, $\phi(\infty) = 0$, and let the concentration at infinity of both the positive and negative ion be c_o, such that $c_\pm(\infty) = c_\mathrm{o}$. Due to equal valences this latter statement ensures overall charge neutrality. With these boundary conditions Eq. (2.10) is readily integrated to yield the ionic concentrations

$$c_\pm(\mathbf{r}) = c_\mathrm{o} \exp\left[\mp \frac{Ne}{k_\mathrm{B}T}\phi(\mathbf{r})\right]. \tag{2.11}$$

Since the valence numbers are always counted positive the charge density ρ_el at any given point is

$$\rho_\mathrm{el}(\mathbf{r}) = Ne\left[c_+(\mathbf{r}) - c_-(\mathbf{r})\right] = -2Nec_\mathrm{o}\sinh\left[\frac{Ne}{k_\mathrm{B}T}\phi(\mathbf{r})\right], \tag{2.12}$$

where the negative charge is treated with an explicit sign. Noting that ρ_el equals the free charge density, combining Eq. (2.12) with Poisson's equation, Eq. (2.5), yields the so-called Poisson–Boltzmann equation

$$\nabla^2\phi(\mathbf{r}) = 2\frac{Nec_\mathrm{o}}{\epsilon}\sinh\left[\frac{Ne}{k_\mathrm{B}T}\phi(\mathbf{r})\right]. \tag{2.13}$$

To solve this equation we use that the potential decays to zero infinitely far from the wall

$$\phi(\infty) = \partial_z\phi(\infty) = 0, \tag{2.14}$$

and that it decreases monotonically to zero away from the wall. The solution is the so-called Gouy–Chapman solution given by

$$\phi(z) = \frac{4k_\mathrm{B}T}{Ne}\mathrm{arctanh}\left[\tanh\left(\frac{Ne\zeta}{4k_\mathrm{B}T}\right)\exp\left(-\frac{z}{\lambda_\mathrm{D}}\right)\right], \tag{2.15}$$

whereby the characteristic length scale, the Debye length λ_D, is introduced and will be derived presently. In the Debye–Hückel limit where the electric potential energy is much smaller than the thermal energy,

$$Ne|\zeta| \ll k_\mathrm{B}T, \tag{2.16}$$

Eq. (2.13) can be Taylor expanded to give

$$\nabla^2\phi(\mathbf{r}) = 2\frac{(Ne)^2 c_\mathrm{o}}{\epsilon k_\mathrm{B}T}\phi(\mathbf{r}) \equiv \frac{1}{(\lambda_\mathrm{D})^2}\phi(\mathbf{r}), \quad \lambda_\mathrm{D} \equiv \sqrt{\frac{\epsilon k_\mathrm{B}T}{2(Ne)^2 c_\mathrm{o}}}. \tag{2.17}$$

Eq. (2.17) can be solved in a parallel plate channel with surfaces at $z = 0$ and $z = h$ assuming that the potential at both plates is ζ

$$\phi(z) = \zeta\frac{\cosh\left(\frac{z-h/2}{\lambda_\mathrm{D}}\right)}{\cosh\left(\frac{h}{2\lambda_\mathrm{D}}\right)}, \quad 0 < z < h. \tag{2.18}$$

2.2 The Surface Charge Density in a Parallel Plate Channel

Consider two infinite parallel plates symmetrically placed at $z = +h/2$ and $z = -h/2$, respectively. Furthermore, consider a liquid containing $\mathcal{N}$ ions each of concentration c_i and valence Z_i in between the plates. Each plate can exchange charge with the liquid and thereby gain a potential ζ. The surface charge density δ can be expressed via the electric potential as

$$\delta\left(\pm\frac{h}{2}\right) = \pm\mathrm{sgn}\left(\zeta\right)\epsilon\partial_z\phi\left(x, y, \pm\frac{h}{2}\right), \tag{2.19}$$

where $\mathrm{sgn}(\cdot)$ is the signum function. So, knowing the gradient of the electric potential at the surface implies knowing the surface charge density. An expression for the ith ion concentration as a function of the electric potential was derived in Eq. (2.11) and is here stated on the form

$$c_i(\mathbf{r}) = c_i^{\mathrm{b}} \exp\left(-\frac{Z_i e}{k_{\mathrm{B}}T}\phi(\mathbf{r})\right). \tag{2.20}$$

The charge density generalized for $\mathcal{N}$ ions is then

$$\rho_{\mathrm{el}}(\mathbf{r}) = e\sum_{i=1}^{\mathcal{N}} Z_i c_i(\mathbf{r}), \tag{2.21}$$

which used in Poisson's equation gives

$$\nabla^2\phi(\mathbf{r}) = -\frac{e}{\epsilon}\sum_{i=1}^{\mathcal{N}} Z_i c_i(\mathbf{r}). \tag{2.22}$$

Assuming a Boltzmann distribution of the ions the concentration of an ion at any point $\mathbf{r}$ can be related to its bulk concentration c_i^{b} and the equation becomes the Poisson–Boltzmann equation

$$\nabla^2\phi(\mathbf{r}) = -\frac{e}{\epsilon}\sum_{i=1}^{\mathcal{N}} Z_i c_i^{\mathrm{b}} \exp\left(-\frac{Z_i e}{k_{\mathrm{B}}T}\phi(\mathbf{r})\right), \tag{2.23}$$

with the bulk value of zero as reference for the electric potential. In steady state the potential is translation invariant in the x and y directions and thus only depends on z, that is, $\phi(\mathbf{r}) = \phi(z) \equiv \phi$, so

$$\mathrm{d}_z^2\phi \equiv \phi'' = -\frac{e}{\epsilon}\sum_{i=1}^{\mathcal{N}} Z_i c_i^{\mathrm{b}} \exp\left(-\frac{Z_i e}{k_{\mathrm{B}}T}\phi\right). \tag{2.24}$$

Using that $\phi''\phi' = \left(\frac{1}{2}\left[\phi'\right]^2\right)'$ the equation becomes

$$\left(\frac{1}{2}\left[\phi'\right]^2\right)' = -\phi'\frac{e}{\epsilon}\sum_{i=1}^{\mathcal{N}} Z_i c_i^{\mathrm{b}} \exp\left(-\frac{Z_i e}{k_{\mathrm{B}}T}\phi\right) = \left(\frac{k_{\mathrm{B}}T}{\epsilon}\sum_{i=1}^{\mathcal{N}} c_i^{\mathrm{b}} \exp\left(-\frac{Z_i e}{k_{\mathrm{B}}T}\phi\right)\right)'. \tag{2.25}$$

Integrating both sides in z and exploiting the symmetry condition at the mid channel $\phi'|_{z=0} = 0$ we get

$$\phi' = \pm \left\{ \frac{2k_B T}{\epsilon} \sum_{i=1}^{\mathcal{N}} c_i^b \left[\exp\left(-\frac{Z_i e}{k_B T} \phi \right) - \exp\left(-\frac{Z_i e}{k_B T} \phi_m \right) \right] \right\}^{\frac{1}{2}}, \tag{2.26}$$

where we denote the potential at $z = 0$ as ϕ_m (m for mid channel). Using Eq. (2.19) the surface charge density for an arbitrary composition of electrolytes can be found by evaluating the gradient at the surface where the potential is the ζ potential

$$\delta = \operatorname{sgn}(\zeta) \left\{ 2\epsilon k_B T \sum_{i=1}^{\mathcal{N}} c_i^b \left[\exp\left(-\frac{Z_i e}{k_B T} \zeta \right) - \exp\left(-\frac{Z_i e}{k_B T} \phi_m \right) \right] \right\}^{\frac{1}{2}}. \tag{2.27}$$

Eq. (2.27) is general but assume now that $\phi_m = 0$ which is the case if the channel height is much larger than the Debye length. Then

$$\delta = \operatorname{sgn}(\zeta) \left\{ 2\epsilon k_B T \sum_{i=1}^{\mathcal{N}} c_i^b \left[\exp\left(-\frac{Z_i e}{k_B T} \zeta \right) - 1 \right] \right\}^{\frac{1}{2}}, \quad \lambda_D \ll h. \tag{2.28}$$

If however, the Debye length becomes large compared to the height the diffusive layers can overlap which is known as diffusive layer overlap.

2.3 Ionic Concentrations

We now introduce the ionic strength and derive the Debye length in terms of this. A sketch of the system parameters discussed in this section can be seen in Fig. 2.1. If the wall is assumed neutral before any electrolyte contacts it, then far away from the wall the ζ potential cannot be felt by any ion, and the system has arranged itself in such a way that charge neutrality preserves here. Therefore, the total charge density ρ_{el} satisfies

$$\rho_{el}(\infty) = e \sum_{i=1}^{\mathcal{N}} Z_i c_i^b = 0. \tag{2.29}$$

The ionic strength $\mathcal{I}$ is a useful concept defined as

$$\mathcal{I} \equiv \frac{1}{2} \sum_{i=1}^{\mathcal{N}} (Z_i)^2 c_i^b. \tag{2.30}$$

In the Debye–Hückel limit the Poisson–Boltzmann equation Eq. (2.23) can be expressed as

$$\nabla^2 \phi(\mathbf{r}) = -\frac{e}{\epsilon} \sum_{i=1}^{\mathcal{N}} Z_i c_i^b \left(1 - \frac{Z_i e}{k_B T} \phi(\mathbf{r}) \right). \tag{2.31}$$

Exploiting the charge neutrality in the bulk, Eq. (2.29), Eq. (2.31) simplifies to

$$\nabla^2\phi(\mathbf{r}) = \frac{e^2}{\epsilon k_\mathrm{B}T}\sum_{i=1}^{\mathcal{N}}\left(Z_i\right)^2 c_i^\mathrm{b}\phi(\mathbf{r}) = \frac{1}{\left\{\lambda_\mathrm{D}\left(\mathcal{I}\right)\right\}^2}\phi(\mathbf{r}), \tag{2.32}$$

where the Debye length in terms of the ionic strength Eq. (2.30) is

$$\lambda_\mathrm{D}(\mathcal{I}) = \sqrt{\frac{\epsilon k_\mathrm{B}T}{2e^2}}\sqrt{2}\left(\sum_{i=1}^{\mathcal{N}}\left(Z_i\right)^2 c_i^\mathrm{b}\right)^{-\frac{1}{2}} = \sqrt{\frac{\epsilon k_\mathrm{B}T}{2\mathcal{I}e^2}}. \tag{2.33}$$

2.4 Chapter Summary

In this chapter we have stated the governing equations for our system shown in Fig. 2.1. In Section 2.1.5 we introduced the ζ potential and stated the analytical Gouy–Chapman, Eq. (2.15), and Debye–Hückel, Eq. (2.18), solutions for the electric potential in a parallel plate channel. In Section 2.2 we derived the general Poisson–Boltzmann equation, Eq. (2.23), together with the general surface charge density δ, Eq. (2.27). The theory presented in this chapter is the theoretical foundation for the remaining of the thesis.

Chapter 3

Chemical Models of Bulk and Surfaces

In the present chapter we show how to calculate the ζ potential and the surface charge density on a discretized amorphous silica surface with a total number of chargeable sites $\Gamma_{\text{tot}} = 5\ \text{sites}\,\text{nm}^{-2}$ [16] contacting an electrolyte containing a salt which is KCl in this thesis. We start the chapter by discussing how to calculate the solute concentrations of all added species in an aqueous solution, we introduce the concept of pH, and show how to account for CO_2 absorption in an aqueous solution. We continue to derive two models of the system which form the basis of the remaining chapters: the 2pK-model strictly only valid for low salt concentrations, and the metal adsorption model valid in the entire salt concentration range. We will discuss how to implement surface coating on the silica channel surfaces in our models. Furthermore, we provide a study of how the plane potentials and surface charge densities calculated from the metal adsorption model, depend on the bulk pH of the electrolyte. We round off this chapter with a study on how the pH varies transverse to the channel walls.

3.1 Aqueous Solutions

A solute in an aqueous solution can separate reversibly into smaller constituents with the dissociation constant measuring the propensity of the constituents to the compound. Consider the dissociation of the solute $\mathrm{A}_x\mathrm{B}_y$

$$\mathrm{A}_x\mathrm{B}_y \leftrightharpoons x\mathrm{A} + y\mathrm{B}, \quad K_{\text{d}} \equiv \frac{(a_{\mathrm{A}})^x\,(a_{\mathrm{B}})^y}{a_{\mathrm{A}_x\mathrm{B}_y}}, \tag{3.1}$$

where a_i is the activity of the ith particle and K_{d} is the dissociation constant for the reaction. For an acid-base reaction K_{d} is typically dubbed K_{a} and is normally scaled down to give the pK_{a} value

$$\mathrm{p}K_{\text{a}} \equiv -\log_{10}(K_{\text{a}})\,. \tag{3.2}$$

3.1.1 Calculation of Solute Concentrations

The formal concentration of a solute in a solution is the total amount of added solute to a volume of solution. The solute dissociates into different charge states and the concentration of each of these is the actual concentration of the particular charge state. The Santiago group at Stanford University has developed a script [14] for calculating the actual concentration of all charge states for any number of added solutes. The Santiago script modified for our purposes can be found in Appendix C.1. It takes as input the formal concentration of all solutes written on an acid dissociation form therefore requiring the pK_a values for each dissociation. The underlying theory of the Santiago script is found in Ref. [6] and we have discussed the governing equations behind the Santiago script in Appendix A.3. The Santiago script facilitates the inclusion of absorbed CO_2 and other solutes when calculating the actual concentrations of all ions in the bulk reservoirs.

3.1.2 pH of an Aqueous Solution

pH and pOH are a measure of the acidity and basicity, respectively, of a solution with[1]

$$\mathrm{pH} \equiv -\log_{10}(a_{\mathrm{H}}) \quad \text{and} \quad \mathrm{pOH} \equiv -\log_{10}(a_{\mathrm{OH}}), \tag{3.3}$$

where a_{H} is strictly speaking the activity of hydronium ions H_3O^+, but in this thesis referred to as the activity of hydrons H^+, and a_{OH} is the activity of hydroxide ions OH^-. We assume that the activity a_i of ion i in an aqueous solution is defined as [15]

$$a_i \equiv \gamma_i \frac{c_i}{1\ \mathrm{M}}, \quad \text{with} \quad \ln(\gamma_i) = -AZ_i^2 \left[\frac{\mathcal{I}^{\frac{1}{2}}}{1+\mathcal{I}^{\frac{1}{2}}} - 0.3\mathcal{I} \right], \tag{3.4}$$

where c_i and γ_i are the actual concentration of ion i and its activity coefficient, respectively. $A = 1.825 \times 10^6/(\epsilon_r T)^{3/2}$ so the error in assuming

$$a_i = \frac{c_i}{1\ \mathrm{M}}, \tag{3.5}$$

for water at room temperature will stay below 10 % for ionic strengths up to 100 mM. The approximation modifies the modern version of the pH and pOH to

$$\mathrm{pH} = -\log_{10}(c_{\mathrm{H}}) \quad \text{and} \quad \mathrm{pOH} = -\log_{10}(c_{\mathrm{OH}}), \tag{3.6}$$

respectively, where c_{H} and c_{OH} are inserted in units of molar. In water the hydrons and hydroxide ions satisfy

$$\mathrm{pH} + \mathrm{pOH} = 14. \tag{3.7}$$

From this relation, the pH alone determines both the concentration of hydrons and hydroxide ions.

[1] The concept of pH was originally introduced by the Danish chemist Søren Peder Lauritz Sørensen at the Carlsberg Laboratories in Denmark, and was refined in 1924 to this modern version.

3.1.3 CO_2 Absorption

Deionized water is expected to have a pH at 7 under the assumption that only water molecules are present subject to autoprotolysis. If the solution is in contact with the atmosphere the pH is lowered because atmospheric CO_2 is absorbed in the solution in much greater amounts than the rest of the atmosphere gasses primarily forming carbonic acid H_2CO_3. In the literature the absorption of CO_2 is seldom taken into account in the solid/liquid interface models and in Chapter 4 we will show that for very low salt concentrations the lowered pH from CO_2 absorption becomes very important when measuring the conductance of a nanochannel.

The equilibrium between gaseous CO_2 in the atmosphere and dissolved CO_2 in an aqueous solution is [17]

$$\mathrm{CO_{2(g)}} \rightleftharpoons \mathrm{CO_{2(aq)}}, \quad H_{\mathrm{CO_2}} = \frac{c_{\mathrm{CO_{2(aq)}}}}{p_{\mathrm{CO_{2(g)}}}} = 3.5 \times 10^{-2}\,\mathrm{M\,atm^{-1}}, \tag{3.8}$$

where $H_{\mathrm{CO_2}}$ is the Henry's law coefficient and $p_{\mathrm{CO_{2(g)}}}$ is the partial pressure of CO_2 in the gas phase. The formation reaction for carbonic acid from CO_2 in an aqueous solution is given by [6]

$$\mathrm{CO_{2(aq)} + H_2O_{(l)}} \rightleftharpoons \mathrm{H_2CO_{3(aq)}}, \quad K_{\mathrm{H_2CO_3}} = \frac{c_{\mathrm{H_2CO_{3(aq)}}}}{c_{\mathrm{CO_{2(aq)}}}} = 2.6 \times 10^{-3}. \tag{3.9}$$

We will here assume a formal concentration of carbonic acid of 1.18×10^{-5} M at 25℃ [6]. The dissociation reactions for carbonic acid are [6]

$$\mathrm{H_2CO_{3(aq)}} \rightleftharpoons \mathrm{HCO^-_{3(aq)} + H^+_{(aq)}}, \quad K_{\mathrm{CO_3},-1} = \frac{c_{\mathrm{H_{(aq)}}}\, c_{\mathrm{HCO^-_{3(aq)}}}}{c_{\mathrm{H_2CO_{3(aq)}}}} = 1.7 \times 10^{-4}\,\mathrm{M}, \tag{3.10}$$

$$\mathrm{HCO^-_{3(aq)}} \rightleftharpoons \mathrm{CO^{2-}_{3(aq)} + H^+_{(aq)}}, \quad K_{\mathrm{CO_3},-2} = \frac{c_{\mathrm{H_{(aq)}}}\, c_{\mathrm{CO^{2-}_{3(aq)}}}}{c_{\mathrm{HCO^-_{3(aq)}}}} = 4.7 \times 10^{-11}\,\mathrm{M}. \tag{3.11}$$

We implement Eqs. (3.10) and (3.11) in the Santiago script and get a pH of 5.68 for deionized water with absorbed CO_2. This correlates with our own experimental measurements.

3.2 Modeling the Solid/Liquid Interface of a Silica Channel

We now turn our discussion to a specific system where the wall is a heterogenous amorphous silica surface and the electrolyte is an aqueous solution with added KCl. The solution has been exposed to CO_2 from the atmosphere neglecting the presence of other atmospheric gasses. The solid/liquid interface as we perceive it is shown in Fig. 3.1. The amorphous nature of the wall makes the distance between each silicon wall atom vary as well as the bond length. From the top of the wall is shown 4 different bond types. (1) a geminal silanol bond where one silicon atom binds to two hydroxide molecules; (2) two silicon atoms binding to the same oxygen atom forming a siloxane bond; (3) two free silanol groups loosely

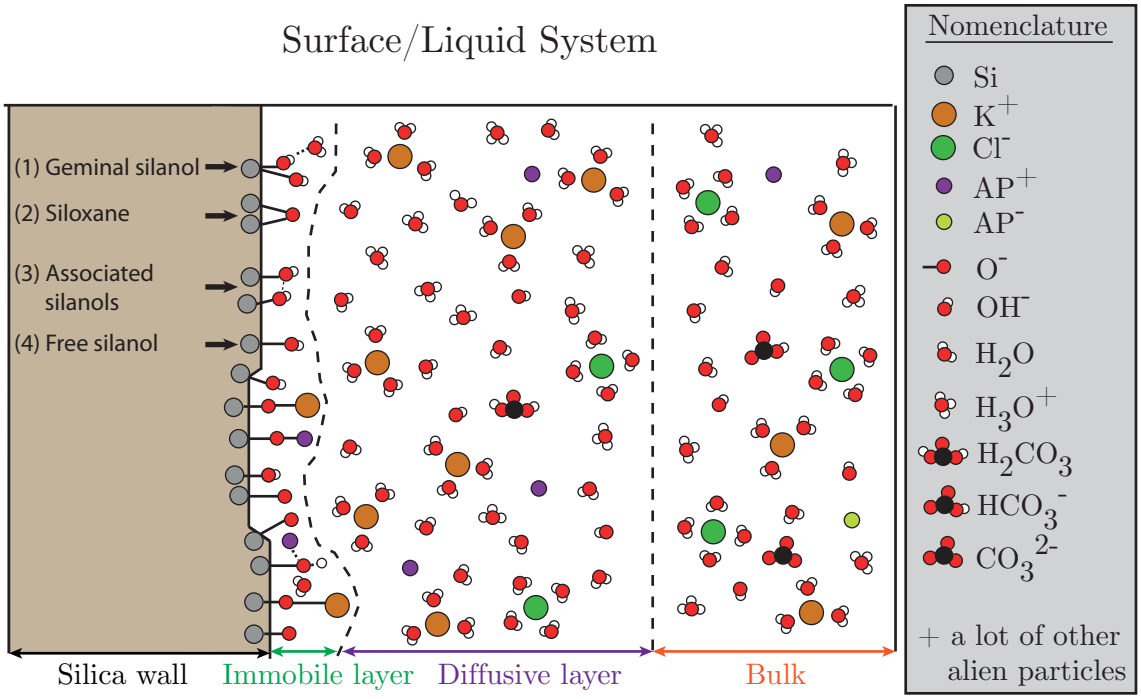

Figure 3.1: A sketch of the surface/liquid system contacting an aqueous solution of KCl. The silica nanochannel surface is the brown area. Four different wall binding types have been shown and labeled at the top of the wall. A nomenclature has been provided to the right in the figure. AP^+ and AP^- stands for a positively and negatively charged alien particle, respectively. At the bottom, four areas of main interest have been identified: the silica wall (black), the immobile layer (green), the diffusive layer (purple), and the bulk region (orange).

binding to each other becoming associated silanols; and (4) a free silanol group which is the most commonly occurring binding type [18]. It is clear from the figure that in order to theoretically capture the physics of the nanochannel surface we need some simplified models so we will start out by discussing our assumptions.

First, we model the ions in the electrolyte as point particles with no spatial extend. In Appendix A.4 we show that it is not necessary to account for finite-sized particles (steric effects) for the ζ potentials and bulk concentrations considered in our thesis. Each ion creates various fields around itself e.g. an electric potential field which affects other particles introducing inter-ionic effects. On a microscopic level the exact effects are difficult to deal with and cannot easily be solved in larger molecular systems using today's methods. We can avoid this complication by assuming the validity of the Poisson–Boltzmann equation which is a mean-field approximation. We assume that the thickness of the immobile layer is constant along the surface and that the dielectric permittivity ϵ does not vary in space. Furthermore, we assume that the electric potential energy arising from the charged sites

System	Model
Particles	
Spatially finite particles (steric effects)	Point particles
Many interactions including correlated interaction effects	No correlated interaction effects but mean-field interaction through Poisson–Boltzmann. Ideal gas
Dissolved molecules from atmosphere	Only considers dissolved CO_2 from atmosphere
Steady-state ion distribution	
Result of all possible microscopic and macroscopic effects in electrolyte	Result only of thermal and electric potential energy
Dielectric permittivity ϵ varies in space	Dielectric permittivity ϵ is constant in space
Silica surface topology	
Different silanol surface groups with different equilibrium equations and dissociation constants (heterogeneous)	Only free chargeable silanol SiOH groups all with the same dissociation constant (homogeneous)
Different bond lengths depending on e.g. neighboring molecules	Same bond length along the surface
Can gain charge e.g. by adsorption of unwanted particles	Gains charge purely by protonization and deprotonization
Thickness of immobile layer varies along surface	Thickness of immobile layer is constant

Table 3.1: The system properties (left column) and the corresponding assumptions in our models (right column). The system has been divided into three major categories: particles, steady-state ion distribution, and silica surface topology.

at the wall together with the thermal energy determine the steady-state ion distribution. Before the surface contacts any electrolyte it is assumed homogeneous consisting only of equally spaced free chargeable silanol groups (SiOH). The potential $\phi(\mathbf{r})$ is given with reference to the bulk potential $\phi(\infty) = 0$. The only way for the wall to attain charge is through protonization and deprotonization of free silanol groups. We have summarized our discussion of our model assumptions in Table 3.1. In the left column the nanochannel liquid/interface system is described with respect to the different major categories of interest: particles, steady-state ion distribution, and silica surface topology. The right column compares these same categories with our models.

Chemical reactions are induced when the electrolyte contacts the wall and hydrons can leave the free silanol SiOH groups to enter the electrolyte thereby creating a negatively charged SiO^- site

$$\mathrm{SiOH} \rightleftharpoons \mathrm{SiO^-} + \mathrm{H^+}, \quad K_- = \frac{\Gamma_{\mathrm{SiO^-}} a^{\mathrm{o}}_{\mathrm{H}}}{\Gamma_{\mathrm{SiOH}}} \quad \text{(deprotonization)}, \tag{3.12}$$

where K_-, $\Gamma_{\mathrm{SiO^-}}$, $a^{\mathrm{o}}_{\mathrm{H}}$, and Γ_{SiOH} is the equilibrium constant of the reaction, $\mathrm{SiO^-}$ site density, the activity of hydrons at the o-plane, and the SiOH site density, respectively. Conversely, hydrons from the electrolyte can react with a free silanol SiOH site to form a positively charged $\mathrm{SiOH_2^+}$ site

$$\mathrm{SiOH_2^+} \rightleftharpoons \mathrm{SiOH} + \mathrm{H^+}, \quad K_+ = \frac{\Gamma_{\mathrm{SiOH}} a^{\mathrm{o}}_{\mathrm{H}}}{\Gamma_{\mathrm{SiOH_2^+}}} \quad \text{(protonization)}, \tag{3.13}$$

where K_+ and $\Gamma_{\mathrm{SiOH_2^+}}$ is the equilibrium constant of the reaction and the $\mathrm{SiOH_2^+}$ site density, respectively.

Incidentally, we note that the concentration of hydrons appears in both Eq. (3.12) and Eq. (3.13) so it should be expected that the acidity of the electrolyte indirectly determines the surface charge density which we will show is also the case. The pH value for which the net surface charge density on the silica wall is zero is referred to as the point of zero charge PZC. The first model we develop considers only the chemical reactions in Eqs. (3.12) and (3.13) and will be named the 2pK-model because it accounts for two surface reactions each with one pK value. Fig. 3.2(a) shows the model which is based on the same principles as the Gouy–Chapman–Stern model presented in Section 1.2. The silica surface is assumed homogenous and immediately next to it a monoatomic layer of immobile ions will form due to strong Coulomb interactions with the wall. In practice it cannot be controlled which ions comprise the immobile layer so we visualize it as a blue area not drawn to scale. The immobile layer has capacitance per unit area C_{s} and will not completely screen the wall so other counterions will be attracted forming a diffusive screening layer of mobile ions. C_{s} was experimentally found for an amorphous silica surface in contact with an aqueous solution in Ref. [9] to have the same order of magnitude and be no greater than 0.2 $\mathrm{F/m^2}$. We will use this value throughout the thesis unless otherwise stated. Recent studies have indicated that C_{s} depends on the ionic strength Eq. (2.30) of the solution.[2] We note that the potential away from the immobile layer satisfies the Poisson–Boltzmann equation Eq. (2.23).

The 2pK-model can safely be used for electrolytes if the salt concentration is below ~ 1 mM [16]. Above this concentration a significant amount of metal ions in the solution will adsorb to the silica surface similar to hydrons but physically further away from the wall. Therefore, inspired by Ref. [16], we will use a model which we name the metal adsorption model taking into account both Eq. (3.12), Eq. (3.13), and the additional surface reaction

$$\mathrm{SiO^-} + \mathrm{M^+} \rightleftharpoons \mathrm{SiOM}, \qquad K_{\mathrm{M}} = \frac{\Gamma_{\mathrm{SiOM}}}{\Gamma_{\mathrm{SiO^-}}\, a^{\beta}_{\mathrm{M}}} \quad \text{(metal adsorption)}, \tag{3.14}$$

where $\mathrm{M^+}$, K_{M}, Γ_{SiOM}, and a^{β}_{M} is a singly ionized metal cation, the equilibrium constant of the reaction, the SiOM site density, and the activity of the metal cation in the β-plane, respectively. This model is shown in Fig. 3.2(b). Since the metal cations attach to the surface physically further away than the hydrons a new plane inside the immobile layer is

[2] Mathias Bækbo Andersen, PhD student, DTU Nanotech.

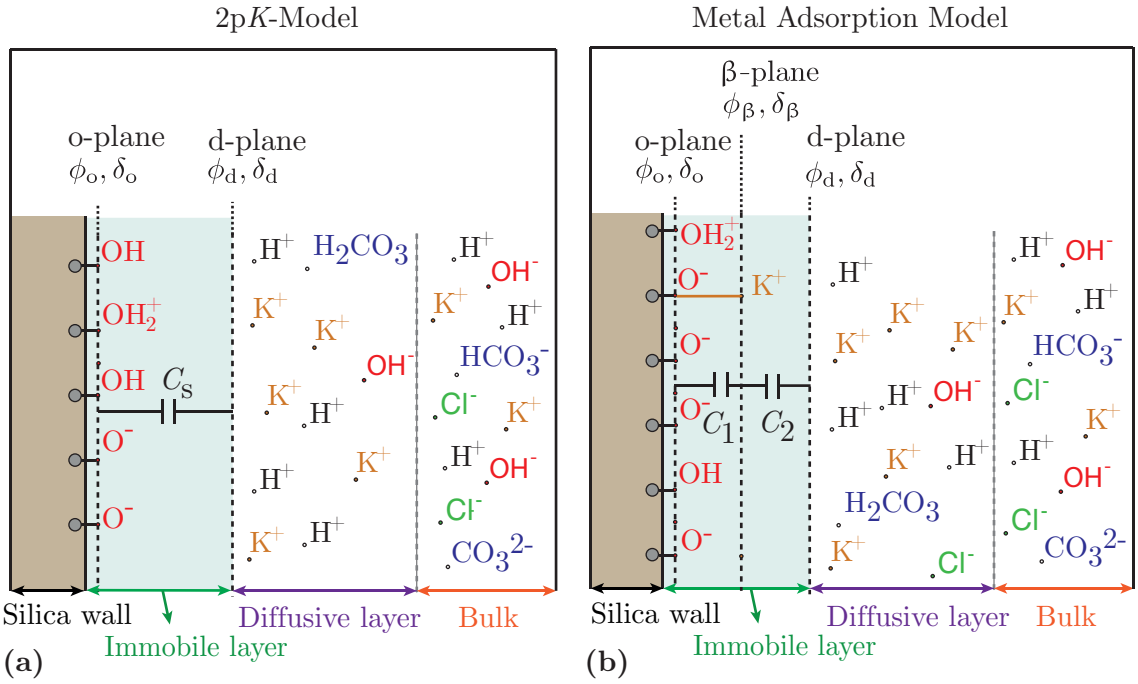

Figure 3.2: A sketch of our models of the silica surface contacting an aqueous solution of KCl. **(a)** shows the 2pK-model and **(b)** the metal adsorption model. The silica nanochannel surface is the brown area. At the bottom, four areas of main interest have been identified on each figure: the silica wall (black arrow), the immobile layer, also known as the Stern layer, (green arrow), the diffusive layer (purple arrow), and the bulk area (orange arrow). The dashed lines represent planes where charge can reside. In both figures are shown the silica surface (o-plane) and the plane where the diffusive layer begins (d-plane). C_s is the capacitance of the immobile layer known as the Stern capacitance. For figure **(b)** is also shown the center plane of the immobile layer (β-plane). C_1 and C_2 are the capacitances of the inner and outer Stern layer. The surface charge density for the o-, β-, and d-plane is denoted δ_o, δ_β, and δ_d, respectively, with corresponding electric potentials ϕ_o, ϕ_β, and ϕ_d, respectively.

created named the β-plane. As discussed in Section 1.2 this model can also be referred to as a triple-layer model. The o-plane and the β-plane form a parallel plate capacitor with capacitance per unit area C_1 also known as the inner Stern capacitance in series with a parallel plate capacitor between the β-plane and the d-plane with capacitance per unit area C_2 also known as the outer Stern capacitance. For the pH range of interest we can safely neglect the adsorption of anions A^- onto the surface since this requires a considerable number of $SiOH_2^+$ sites, only present for very low pH.

In the two following sections we will develop our two models starting with the 2pK-model.

3.3 The 2pK-Model

The 2pK-model sketched in Fig. 3.2(a) accounts for the two chemical reactions in Eqs. (3.12) and (3.13). The conservation of number of chargeable sites at the silica surface yields

$$\Gamma_{\text{tot}} = \Gamma_{\text{SiOH}} + \Gamma_{\text{SiO}^-} + \Gamma_{\text{SiOH}_2^+}. \tag{3.15}$$

The site density for site state i can be expressed as a surface coverage θ_i

$$\theta_{\text{SiOH}} \equiv \frac{\Gamma_{\text{SiOH}}}{\Gamma_{\text{tot}}}, \tag{3.16a}$$

$$\theta_{\text{SiO}^-} \equiv \frac{\Gamma_{\text{SiO}^-}}{\Gamma_{\text{tot}}}, \tag{3.16b}$$

$$\theta_{\text{SiOH}_2^+} \equiv \frac{\Gamma_{\text{SiOH}_2^+}}{\Gamma_{\text{tot}}}, \tag{3.16c}$$

changing Eq. (3.15) to

$$1 = \theta_{\text{SiOH}} + \theta_{\text{SiO}^-} + \theta_{\text{SiOH}_2^+}. \tag{3.17}$$

Assuming the hydrons to be Boltzmann distributed gives for the equilibrium constants in Eqs. (3.12) and (3.13)

$$K_- = \frac{\theta_{\text{SiO}^-}}{\theta_{\text{SiOH}}} c_{\text{H}}^{\text{b}} \exp\left(-\frac{e}{k_{\text{B}}T}\phi_{\text{o}}\right), \tag{3.18a}$$

$$K_+ = \frac{\theta_{\text{SiOH}}}{\theta_{\text{SiOH}_2^+}} c_{\text{H}}^{\text{b}} \exp\left(-\frac{e}{k_{\text{B}}T}\phi_{\text{o}}\right). \tag{3.18b}$$

The surface charge density in the o-plane is determined only by the SiO^- and $SiOH_2^+$ sites so

$$\delta_{\text{o}} = e\Gamma_{\text{tot}}\left(\theta_{\text{SiOH}_2^+} - \theta_{\text{SiO}^-}\right). \tag{3.19}$$

Global charge neutrality demands that the net charge density at the wall is balanced by an equal amount of diffusive counterions at the d-plane so

$$\delta_{\text{o}} + \delta_{\text{d}} = 0. \tag{3.20}$$

The voltage drop between the o-plane and the d-plane is

$$\phi_{\mathrm{o}} - \phi_{\mathrm{d}} = \frac{\delta_{\mathrm{o}}}{C_{\mathrm{s}}}. \tag{3.21}$$

Throughout this thesis we take the ϕ_{d} potential (d for diffusive plane) to equal the ζ potential which is justified for low concentrations see Ref. [5]. The surface charge density at the d-plane where the diffusive layer begins can be thought of as a projection of the charges in the diffusive layer onto the plane. The surface charge density is given by the Gouy–Chapman expression in Eq. (2.28) with an opposite sign where $\phi_{\mathrm{m}} = 0$. From Eq. (3.20) it also has to equal $-\delta_{\mathrm{o}}$ so

$$\delta_{\mathrm{d}} = -\delta_{\mathrm{o}} = -\mathrm{sgn}\left(\phi_{\mathrm{d}}\right)\left\{2\epsilon k_{\mathrm{B}}T\sum_{i=1}^{\mathcal{N}} c_i^{\mathrm{b}}\left[\exp\left(-\frac{Z_i e}{k_{\mathrm{B}}T}\phi_{\mathrm{d}}\right) - 1\right]\right\}^{\frac{1}{2}}. \tag{3.22}$$

In Appendix A.5 we have developed a general expression for the surface coverages, inspired by Ref. [5], for the metal adsorption model to be introduced and discussed in the next section. For this current model the coverage of the ith site state takes the form

$$\theta_i = \frac{\mathcal{K}_i f_i}{1 + \sum_j \mathcal{K}_j f_j}, \quad i,j = \{\mathrm{SiOH}, \mathrm{SiOH}_2^+\}, \tag{3.23}$$

where

$$\mathcal{K}_{\mathrm{SiOH}} \equiv (K_-)^{-1}, \quad f_{\mathrm{SiOH}} \equiv c_{\mathrm{H}}^{\mathrm{b}} \exp\left(-\frac{e}{k_{\mathrm{B}}T}\phi_{\mathrm{o}}\right), \tag{3.24a}$$

$$\mathcal{K}_{\mathrm{SiOH}_2^+} \equiv (K_- K_+)^{-1}, \quad f_{\mathrm{SiOH}_2^+} \equiv \left(f_{\mathrm{SiOH}}\right)^2. \tag{3.24b}$$

Note that the conservation of total number of chargeable sites Eq. (3.17) together with Eq. (3.23) gives

$$\theta_{\mathrm{SiO^-}} = \left(1 + \sum_i \mathcal{K}_i f_i\right)^{-1}, \quad i = \{\mathrm{SiOH}, \mathrm{SiOH}_2^+\}. \tag{3.25}$$

There are three nonlinear equations in the three unknowns ϕ_{o}, ϕ_{d}, and δ_{o} describing the system: the Gouy–Chapman surface charge density Eq. (3.22), the capacitor relation Eq. (3.21), and the surface charge density in the o-plane Eq. (3.19) with the coverages of SiOH_2^+ and $\mathrm{SiO^-}$ sites Eqs. (3.23) and (3.25), respectively, inserted. The equations are

$$\delta_{\mathrm{o}} = \mathrm{sgn}\left(\phi_{\mathrm{d}}\right)\left\{2\epsilon k_{\mathrm{B}}T\sum_{i=1}^{\mathcal{N}} c_i^{\mathrm{b}}\left[\exp\left(-\frac{Z_i e}{k_{\mathrm{B}}T}\phi_{\mathrm{d}}\right) - 1\right]\right\}^{\frac{1}{2}}, \tag{3.26a}$$

$$\phi_{\mathrm{o}} = \phi_{\mathrm{d}} + \frac{\delta_{\mathrm{o}}}{C_{\mathrm{s}}}, \tag{3.26b}$$

$$\delta_{\mathrm{o}} = \tag{3.26c}$$

$$\Gamma_{\mathrm{tot}} e \left(\frac{(K_+)^{-1}\left(c_{\mathrm{H}}^{\mathrm{b}}\right)^2 \exp\left(-\frac{2e}{k_{\mathrm{B}}T}\phi_{\mathrm{o}}\right) - K_-}{K_- + c_{\mathrm{H}}^{\mathrm{b}} \exp\left(-\frac{e}{k_{\mathrm{B}}T}\phi_{\mathrm{o}}\right) + (K_+)^{-1}\left(c_{\mathrm{H}}^{\mathrm{b}}\right)^2 \exp\left(-\frac{2e}{k_{\mathrm{B}}T}\phi_{\mathrm{o}}\right)}\right).$$

Input		Output	
Lab input		Parameter	Symbol
Parameter	Symbol	Potentials	(ϕ_o, ϕ_d)
Channel geometry (height, width, length)	(h, w, L)	(o-plane, d-plane)	
Temperature	T	Surface charge densities	(δ_o, δ_d)
Formal concentrations of all species	c_{formal}	(o-plane, d-plane)	
Literature Input		Actual concentrations	c_{actual}
Parameter	Symbol	of all species	
pK_a for the silica channel wall reaction: $SiOH \rightleftharpoons SiO^- + H^+$	pK_-	Transverse concentration profile for the ith ion	$c_i(z)$
pK_a for the silica channel wall reaction: $SiOH_2^+ \rightleftharpoons SiOH + H^+$	pK_+	Silica surface point of zero charge	PZC
Stern capacitance	C_s	Bulk solution acidity	pH_b
Total number of chargeable sites SiOH	Γ_{tot}	Debye length	λ_D
Charge states for all species in the bulk	-	Transverse potential profile	$\phi(z)$
Dissociation constant for all bulk reactions	pK_a		

Table 3.2: Input/output parameters for the 2pK-model. The inputs are divided into values obtained from laboratory measurements (lab input) and values obtained from the literature (literature input).

We solve the equations in MatLab for ϕ_d using the built-in function `fzero`. All the plane potentials and surface charge densities can be calculated as follows:

1 Use our modified Santiago script in Appendix C.1 to find the bulk pH and the actual concentrations of all charge states of the species in the electrolyte see Section 3.1.

2 Use our script in Appendix C.3 to solve ϕ_d with a start guess.

3 Calculate δ_o by inserting ϕ_d from step 2 and the concentrations from step 1 into Eq. (3.26a). Insert then δ_o into Eq. (3.26b) and thereby calculate ϕ_o.

Following this procedure we now know ϕ_o, ϕ_d, and δ_o. A table of all the parameters going into the 2pK-model (input) and the most relevant parameters calculated by the model (output) can be seen in Table 3.2. The inputs are divided into values obtained from laboratory measurements (lab input) and values obtained from the literature (literature input). We later investigate which input values are best fit parameters see Section 4.3.1. We note that the concise form of the site coverages Eqs. (3.23)–(3.25) increases the numerical stability in MatLab with respect to the start guess and its general form allows for an easy implementation of additional surface reactions.

3.4 The Metal Adsorption Model

The metal adsorption model sketched in Fig. 3.2(b) accounts for the chemical reactions in Eqs. (3.12), (3.13), and (3.14). Define the surface coverage of SiOM sites

$$\theta_{\mathrm{SiOM}} \equiv \frac{\Gamma_{\mathrm{SiOM}}}{\Gamma_{\mathrm{tot}}}. \tag{3.27}$$

Let ϕ_β be the potential in the β-plane and assume that the metal cations are Boltzmann distributed, then the equilibrium constant Eq. (3.14) can be written

$$K_{\mathrm{M}} = \frac{\theta_{\mathrm{SiOM}}}{\theta_{\mathrm{SiO^-}}} \frac{1}{c_{\mathrm{M}}^{\mathrm{b}}} \exp\left(\frac{e\phi_\beta}{k_{\mathrm{B}}T}\right), \tag{3.28}$$

where $c_{\mathrm{M}}^{\mathrm{b}}$ is the bulk concentration of the metal cations. The new surface site state SiOM leads to an extension of the conservation of number of chargeable sites Eq. (3.17)

$$1 = \theta_{\mathrm{SiOH}} + \theta_{\mathrm{SiO^-}} + \theta_{\mathrm{SiOH_2^+}} + \theta_{\mathrm{SiOM}}. \tag{3.29}$$

By defining δ_β as the β-plane surface charge density, the global charge neutrality states

$$\delta_{\mathrm{o}} + \delta_\beta + \delta_{\mathrm{d}} = 0. \tag{3.30}$$

An adsorbed metal ion $\mathrm{M^+}$ in the β-plane will occupy an $\mathrm{SiO^-}$ site at the surface and therefore, the SiOM site corresponds to a negative charge in the o-plane confer Fig. 3.2(b). The o-plane surface charge density is therefore

$$\delta_{\mathrm{o}} = e\Gamma_{\mathrm{tot}} \left(\theta_{\mathrm{SiOH_2^+}} - \theta_{\mathrm{SiO^-}} - \theta_{\mathrm{SiOM}}\right). \tag{3.31}$$

The surface charge density in the β-plane is only determined by adsorbed metal cations

$$\delta_\beta = e\Gamma_{\mathrm{tot}}\theta_{\mathrm{SiOM}}. \tag{3.32}$$

The Gouy–Chapman surface charge density Eq. (2.28) can be thought of as the charge density screened by the diffusive layer, i.e. $\delta_{\mathrm{o}} + \delta_\beta$, and hence δ_{d} becomes

$$\delta_{\mathrm{d}} = -\left(\delta_{\mathrm{o}} + \delta_\beta\right) = -\mathrm{sgn}\left(\phi_{\mathrm{d}}\right) \left\{ 2\epsilon k_{\mathrm{B}}T \sum_{i=1}^{\mathcal{N}} c_i^{\mathrm{b}} \left[\exp\left(-\frac{Z_i e}{k_{\mathrm{B}}T}\phi_{\mathrm{d}}\right) - 1\right] \right\}^{\frac{1}{2}}. \tag{3.33}$$

In the 2pK-model the region between the o-plane and the d-plane was interpreted as a capacitor with the Stern capacitance C_{s}. With the additional charged β-plane the region can now be modeled as two capacitors in series. The region from the o-plane to the β-plane dubbed the inner immobile layer is a capacitor with surface charge density δ_{o} and capacitance per unit area C_1. The region from the β-plane to the d-plane is dubbed the outer immobile layer and is the second capacitor with surface charge density $-\delta_{\mathrm{d}}$ and capacitance per unit area C_2. The relation between ϕ_{o} and ϕ_β becomes

$$\phi_{\mathrm{o}} - \phi_\beta = \frac{\delta_{\mathrm{o}}}{C_1}, \tag{3.34}$$

and that between ϕ_β and ϕ_d

$$\phi_\beta - \phi_d = -\frac{\delta_d}{C_2}. \tag{3.35}$$

C_2 is assumed independent of the type of adsorbed metal ion and is treated as an intrinsic property of a silica surface contacting an aqueous solution. On the contrary, we can give some qualitative arguments why C_1 should change with the type of adsorbed metal ion. In the capacitor picture $C_1 = \epsilon_1/d_1$, where ϵ_1 and d_1 is the permittivity and thickness of the inner immobile layer, respectively. d_1 can be related to the bonding length of adsorbed metal cations to the surface and it is possible for ϵ_1 to change e.g. when adsorbed metal ions expel water molecules from the region.

The governing equations of the metal adsorption model are Eq. (3.18) and Eqs. (3.28)–(3.35). The number of coupled equations will be reduced to effectively solve the system in MatLab. First, Eqs. (3.18), (3.28), and (3.29) are used to derive the surface coverages on the form

$$\theta_i = \frac{\mathcal{K}_i f_i}{1 + \sum_j \mathcal{K}_j f_j}, \quad i,j = \{\mathrm{SiOH_2^+}, \mathrm{SiOH}, \mathrm{SiOM}\}, \tag{3.36}$$

where

$$\mathcal{K}_{\mathrm{SiOH}} \equiv (K_-)^{-1}, \quad f_{\mathrm{SiOH}} \equiv c_{\mathrm{H}}^{\mathrm{b}} \exp\left(-\frac{e}{k_{\mathrm{B}}T}\phi_o\right), \tag{3.37}$$

$$\mathcal{K}_{\mathrm{SiOM}} \equiv K_{\mathrm{M}}, \quad f_{\mathrm{SiOM}} \equiv c_{\mathrm{M}}^{\mathrm{b}} \exp\left(-\frac{e}{k_{\mathrm{B}}T}\phi_\beta\right), \tag{3.38}$$

$$\mathcal{K}_{\mathrm{SiOH_2^+}} \equiv (K_- K_+)^{-1}, \quad f_{\mathrm{SiOH_2^+}} \equiv \left(c_{\mathrm{H}}^{\mathrm{b}}\right)^2 \exp\left(-\frac{2e}{k_{\mathrm{B}}T}\phi_o\right) = \left(f_{\mathrm{SiOH}}\right)^2. \tag{3.39}$$

This derivation can be seen in Appendix A.5. From Eq. (3.36) and the conservation of number of chargeable sites Eq. (3.29)

$$\theta_{\mathrm{SiO^-}} = \left(1 + \sum_i \mathcal{K}_i f_i\right)^{-1}, \quad i = \{\mathrm{SiOH}, \mathrm{SiOH_2^+}, \mathrm{SiOM}\}. \tag{3.40}$$

Using Eqs. (3.36) and (3.40) in Eqs. (3.31) and (3.32) we get

$$\delta_o = e\Gamma_{\mathrm{tot}} \left(\frac{\mathcal{K}_{\mathrm{SiOH_2^+}} f_{\mathrm{SiOH_2^+}} - \mathcal{K}_{\mathrm{SiOM}} f_{\mathrm{SiOM}} - 1}{1 + \mathcal{K}_{\mathrm{SiOM}} f_{\mathrm{SiOM}} + \mathcal{K}_{\mathrm{SiOH}} f_{\mathrm{SiOH}} + \mathcal{K}_{\mathrm{SiOH_2^+}} f_{\mathrm{SiOH_2^+}}}\right), \tag{3.41}$$

$$\delta_\beta = e\Gamma_{\mathrm{tot}} \left(\frac{\mathcal{K}_{\mathrm{SiOM}} f_{\mathrm{SiOM}}}{1 + \mathcal{K}_{\mathrm{SiOM}} f_{\mathrm{SiOM}} + \mathcal{K}_{\mathrm{SiOH}} f_{\mathrm{SiOH}} + \mathcal{K}_{\mathrm{SiOH_2^+}} f_{\mathrm{SiOH_2^+}}}\right). \tag{3.42}$$

Inserting Eq. (3.41) in Eq. (3.34) gives

$$C_1 (\phi_o - \phi_\beta) = e\Gamma_{\mathrm{tot}} \left(\frac{\mathcal{K}_{\mathrm{SiOH_2^+}} f_{\mathrm{SiOH_2^+}} - \mathcal{K}_{\mathrm{SiOM}} f_{\mathrm{SiOM}} - 1}{1 + \mathcal{K}_{\mathrm{SiOM}} f_{\mathrm{SiOM}} + \mathcal{K}_{\mathrm{SiOH}} f_{\mathrm{SiOH}} + \mathcal{K}_{\mathrm{SiOH_2^+}} f_{\mathrm{SiOH_2^+}}}\right). \tag{3.43}$$

	Electrolyte	
	NaCl	KCl
C_1 [F m^{-2}]	1.07 ± 0.13	1.16 ± 0.14
$\log_{10} K_-$	-6.73 ± 0.11	-6.64 ± 0.20
$\log_{10} K_\mathrm{M}$	-0.25 ± 0.20	0.06 ± 0.30

Table 3.3: Summary of the fitting parameters obtained from Ref. [16]. The authors fit the metal adsorption model to experimental data for $\Gamma_\mathrm{tot} = 5$ sites nm^{-2} and $C_2 = 0.2\,\mathrm{F\,m^{-2}}$. The surface is amorpheous sillica.

Using Eqs. (3.41) and (3.42) in the equation for global charge neutrality Eq. (3.30) leads to

$$\delta_\mathrm{d} = -e\Gamma_\mathrm{tot}\left(\frac{\mathcal{K}_{\mathrm{SiOH_2^+}} f_{\mathrm{SiOH_2^+}} - 1}{1 + \mathcal{K}_\mathrm{SiOM} f_\mathrm{SiOM} + \mathcal{K}_\mathrm{SiOH} f_\mathrm{SiOH} + \mathcal{K}_{\mathrm{SiOH_2^+}} f_{\mathrm{SiOH_2^+}}}\right). \tag{3.44}$$

Eqs. (3.43), (3.44), and the capacitor relation (3.35) with δ_d given in Eq. (3.33) are solved in MatLab for the three unknowns ϕ_o, ϕ_β, and ϕ_d using the built-in function `fsolve`. Similar to the 2pK-model all the plane potentials and surface charge densities can be calculated as follows:

1 Use our modified Santiago script in Appendix C.1 to find the bulk pH and the actual concentrations of all charge states of the species in the electrolyte see Section 3.1.

2 Use our script in Appendix C.4 with the fitting parameters provided in Table 3.3 to calculate $\phi_\mathrm{o}, \phi_\beta$, and ϕ_d using start guesses.

3 Calculate $\delta_\mathrm{o}, \delta_\beta$, and δ_d by inserting the potentials from step 2 and concentrations from step 1 into Eq. (3.41), Eq. (3.42), and Eq. (3.44).

Following this procedure we now know the potentials and surface charge densities in all the planes. A table of all the parameters going into the metal adsorption model (input) and most relevant parameters calculated by the model (output) can be seen in Table B.4 in Appendix B.

Note that the knowledge of pK_- and pK_+ gives the value of the point of zero charge. We will show why using the 2pK-model: the point of zero charge is defined as

$$\delta_\mathrm{o}\,(\mathrm{pH} = \mathrm{PZC}) = 0. \tag{3.45}$$

Thus, PZC is the pH value for which the net surface charge density is zero. Since in this case no charge reside in the d-plane either, the potential does not change from the zero bulk level to the wall, so from Eq. (3.26c) with $\phi_\mathrm{o} = 0$ we have

$$\left(c_\mathrm{H}^\mathrm{b}\right)^2 = K_- K_+ \quad (\mathrm{pH} = \mathrm{PZC})\,, \tag{3.46}$$

which yields

$$\mathrm{PZC} = \frac{1}{2}\left(\mathrm{p}K_- + \mathrm{p}K_+\right). \tag{3.47}$$

Eq. (3.47) can also be derived from the metal adsorption model requiring taking into account the anion adsorption during the derivation and exploiting the experimental observation that the point of zero charge is independent of the solution salinity. To see this derivation we refer to Ref. [5].

3.5 Modeling Coated Silica Surfaces

The surface charge of a silica surface contacting an aqueous solution depends on pH as seen in Fig. 3.4, and will later be shown also to depend on the salt concentration of the solution confer Fig. 4.12(a) for $\theta_{\mathrm{amin}} = 0$. Furthermore, as we show in Section 4.3 the surface charge has a great impact on the conductance of a nanochannel for low salt concentrations, i.e. salt concentrations below ∼1 mM. The ability to control the surface charge density is therefore of great importance in electrokinetic applications and in order to get a more well-defined surface charge density the surface is coated by flushing the nanochannels with coating solutions containing the coating molecules. The kind of coatings treated here is larger molecules adsorbing to the silica surface sites and possibly blocking nearby sites due to their large size. A sketch of the system having been flushed with a 3-aminopropyldimethylethoxysilane coating solution is shown in Fig. 3.3(a). This adsorbed coating molecule will throughout the thesis be referred to as aminosilane. The coating molecules can be negative e.g. carboxyethylsilanetriol, neutral e.g. 3-cyanopropyldimethylchlorosilane, or positive e.g. aminosilane, so the surface can in principle be coated to have any desired charge density.[3]

Modeling coated silica nanochannel surfaces has not been introduced in the literature before to our best knowledge and we will now present our way of implementing coated surfaces in our models. The coating molecules are modeled with no spatial extend and unable to change their charge states through any chemical reaction although we note that the charge of the coatings in reality depends on pH [19]. A sketch of the 2pK-model with aminosilane coating, shown as the positively charged NH_3^+ group, is seen in Fig. 3.3(b). For simplicity it is assumed that the surface is only coated with one type of coating. The surface coverage of coated sites is defined as

$$\theta_{\mathrm{coat}} \equiv \frac{\Gamma_{\mathrm{coat}}}{\Gamma_{\mathrm{tot}}}, \tag{3.48}$$

where Γ_{coat} is the coating site density. θ_{coat} will be constant because the coated molecules do not participate in any chemical reactions. The surface charge density at the silica surface for the coated channel is

$$\delta_{\mathrm{o}} = e\Gamma_{\mathrm{tot}}\left(\theta_{\mathrm{SiOH_2^+}} + Z_{\mathrm{coat}}\theta_{\mathrm{coat}} - \theta_{\mathrm{SiO^-}}\right), \tag{3.49}$$

[3] Theoretically, the maximum number of coatable sites is Γ_{tot} and as the density of coated sites increases it becomes harder to add new coating molecules to the surface. Therefore, the maximum number of coatable sites is expected to be lower.

where Z_{coat} is the sign carrying valence of the coated site. For aminosilane we assume $Z_{\text{coat}}^{\text{amin}} = 1$. With the addition of coated sites the conservation of total number of chargeable sites Eq. (3.17) becomes

$$1 = \theta_{\text{SiOH}_2^+} + \theta_{\text{SiOH}} + \theta_{\text{SiO}^-} + \alpha_{\text{bl}}\theta_{\text{coat}}, \tag{3.50}$$

where α_{bl} is a factor describing the number of blocked free silanols including the coated site itself due to a coated molecule confer the red circle in the bottom of Fig. 3.3(a). α_{bl} varies along the surface and is related to the area covered by the coating molecule. For aminosilane we assume $\alpha_{\text{bl}} = 1$. Since $\alpha_{\text{bl}}\theta_{\text{coat}}$ will be constant the fraction of free silanols becomes $1 - \alpha_{\text{bl}}\theta_{\text{coat}} = \theta_{\text{SiOH}_2^+} + \theta_{\text{SiOH}} + \theta_{\text{SiO}^-}$, and the surface coverages in Eqs. (3.23) and (3.25) must be scaled down to

$$\theta_i = \frac{(1 - \alpha_{\text{bl}}\theta_{\text{coat}})\,\mathcal{K}_i f_i}{1 + \sum_j \mathcal{K}_j f_j}, \quad i, j = \{\text{SiOH}_2^+, \text{SiOH}\}, \tag{3.51}$$

and

$$\theta_{\text{SiO}^-} = \frac{1 - \alpha_{\text{bl}}\theta_{\text{coat}}}{1 + \sum_j \mathcal{K}_j f_j}, \quad j = \{\text{SiOH}_2^+, \text{SiOH}\}. \tag{3.52}$$

A study on how aminosilane coating influences the conductance of a nanochannel will be carried out in Section 4.3.2.

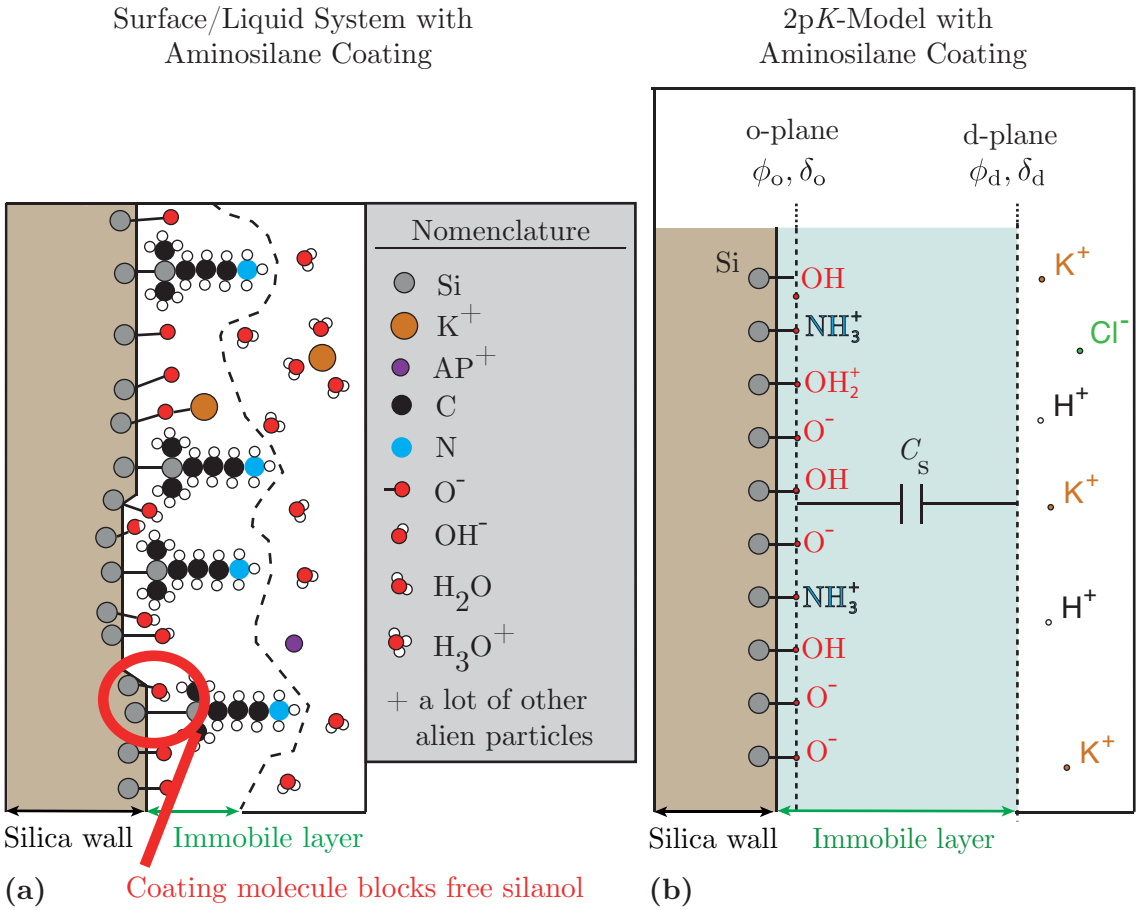

Figure 3.3: **(a)** The system coated with aminosilane which is shown as the molecules mainly composed of carbon atoms (black circles) and a charged NH_3^+ end group (blue circle with three white circles attached to it). The red circle with text box in the bottom of the figure shows a coated molecule blocking a free silanol site. A nomenclature is provided in the right of the figure and at the bottom, the silica wall region and immobile layer are outlined. **(b)** The 2pK-model where the silica wall is coated with aminosilane (NH_3^+). The o-plane and d-plane with their respective potentials and surface charge densities are shown and at the bottom, the silica wall region and immobile layer are outlined. The Stern capacitance C_s is shown in the center of the immobile region. In both figures the diffusive layer and bulk region has been left out for clarity.

3.6 Metal Adsorption Model Dependence on pH

In this section we study the solution of the metal adsorption model versus the bulk pH. By adjusting the surface dissociation constants in Eqs. (3.12), (3.13), and (3.14) we adjust the ratio of charged sites to neutral sites and thereby the surface charge density. We will show that the number of positive sites SiOH_2^+ governed by K_+ in Eq. (3.13) are orders of magnitude lower than negative sites SiO^- governed by K_- in Eq. (3.12) over the pH range of interest. The positive sites only dominate the surface for very low pH values. We choose to include an indication of how the coverages change when adjusting the pK_- value which we expect induces a noticeable effect on the coverages. Furthermore, in the next chapter we calculate the conductance of a nanochannel versus bulk salt concentration using the 2pK-model, and we find that the pK_- value dominates the conductance curve behavior so we are going to use pK_- as a fitting parameter later.

3.6.1 Surface Dissociation Constants

The ith logarithmic surface dissociation constant pK_i depends in general on thermodynamic variables such as temperature and the heat of reaction as studied in Ref. [20]. It is customary to use the surface dissociation constants as best fit parameters confer Table 3.3 which will also be done in our work. Henderson–Hasselbalch expressions are obtained by taking the logarithm of the dissociation constants in Eqs. (3.12) and (3.13)

$$\mathrm{pH_o} = \mathrm{p}K_- + \log_{10}\left(\frac{\Gamma_{\mathrm{SiO^-}}}{\Gamma_{\mathrm{SiOH}}}\right) \Rightarrow \frac{\mathrm{d}\left(\frac{\Gamma_{\mathrm{SiO^-}}}{\Gamma_{\mathrm{SiOH}}}\right)}{\mathrm{dpH_o}} = 10^{\mathrm{pH_o}-\mathrm{p}K_-}\ln(10) > 0, \tag{3.53}$$

$$\mathrm{pH_o} = \mathrm{p}K_+ + \log_{10}\left(\frac{\Gamma_{\mathrm{SiOH}}}{\Gamma_{\mathrm{SiOH_2^+}}}\right) \Rightarrow \frac{\mathrm{d}\left(\frac{\Gamma_{\mathrm{SiOH}}}{\Gamma_{\mathrm{SiOH_2^+}}}\right)}{\mathrm{dpH_o}} = 10^{\mathrm{pH_o}-\mathrm{p}K_+}\ln(10) > 0, \tag{3.54}$$

where $\mathrm{pH_o}$ is the pH in the o-plane. We will now discuss the qualitative trends of these equations when changing pK_- and $\mathrm{pH_o}$ which will serve as a reference for the next section.

Consider pK_- constant for a given solution. From the left equation in Eq. (3.53) We note that if $\mathrm{pH_o}$ is greater than pK_- there must be more negative SiO^- sites relative to neutral SiOH sites. Consider now a fixed value of $\mathrm{pH_o}$: for a lower pK_- value the ratio of SiO^- sites to SiOH sites is higher. Therefore, we can make the silica surface more negatively charged by lowering pK_-. Also, the right equation in Eq. (3.53) shows that an increase in $\mathrm{pH_o}$ always gives an increase in SiO^- sites relative to SiOH sites. Similarly, from the right equation in Eq. (3.54), when $\mathrm{pH_o}$ is increased the number of neutral SiOH sites relative to positive SiOH_2^+ sites increases lowering the surface charge density.

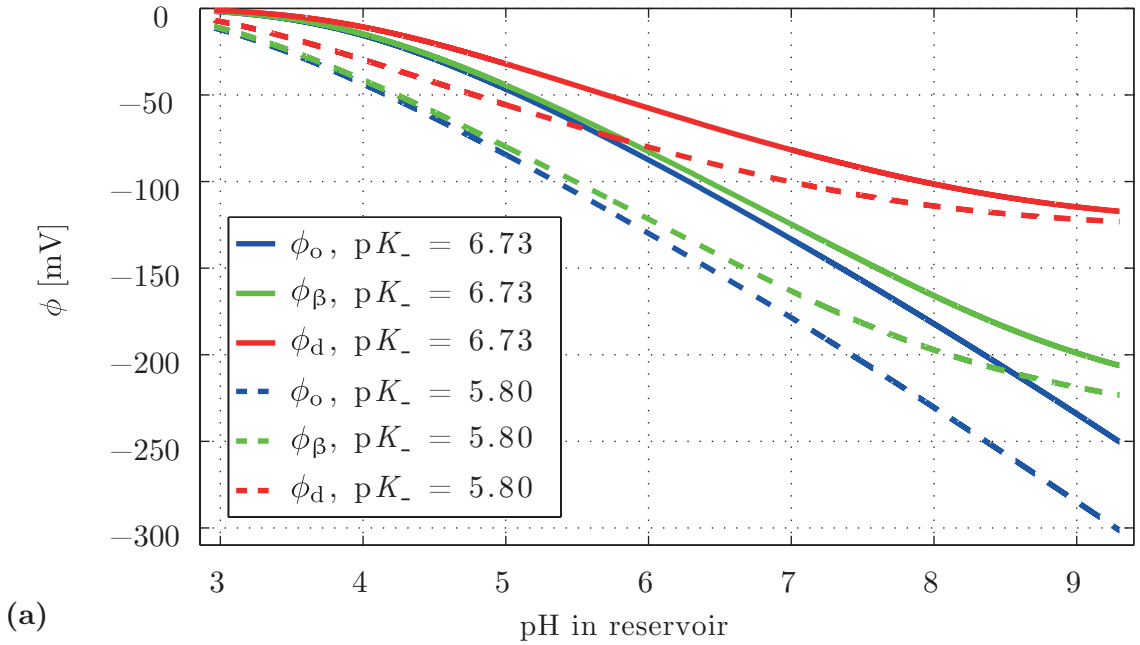

(a)

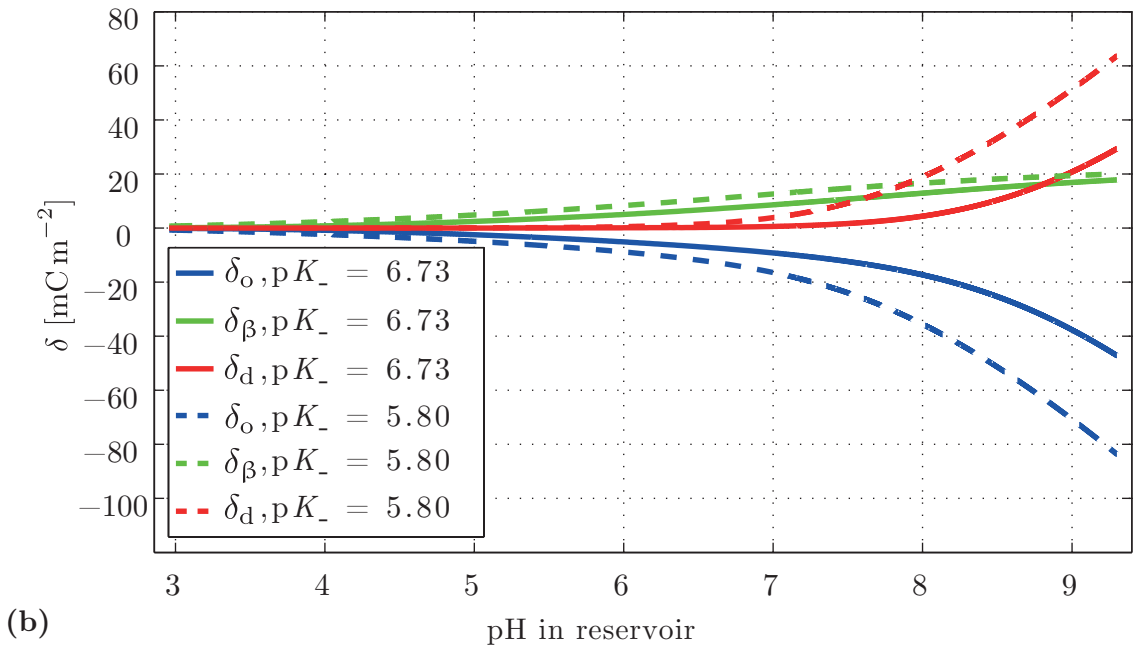

(b)

Figure 3.4: **(a)** plane potentials and **(b)** plane surface charge densities plotted versus bulk pH. In both plots pH is changed by adding NaOH or HCl to a 1 mM NaCl solution. Used model parameters are in Table 3.3.

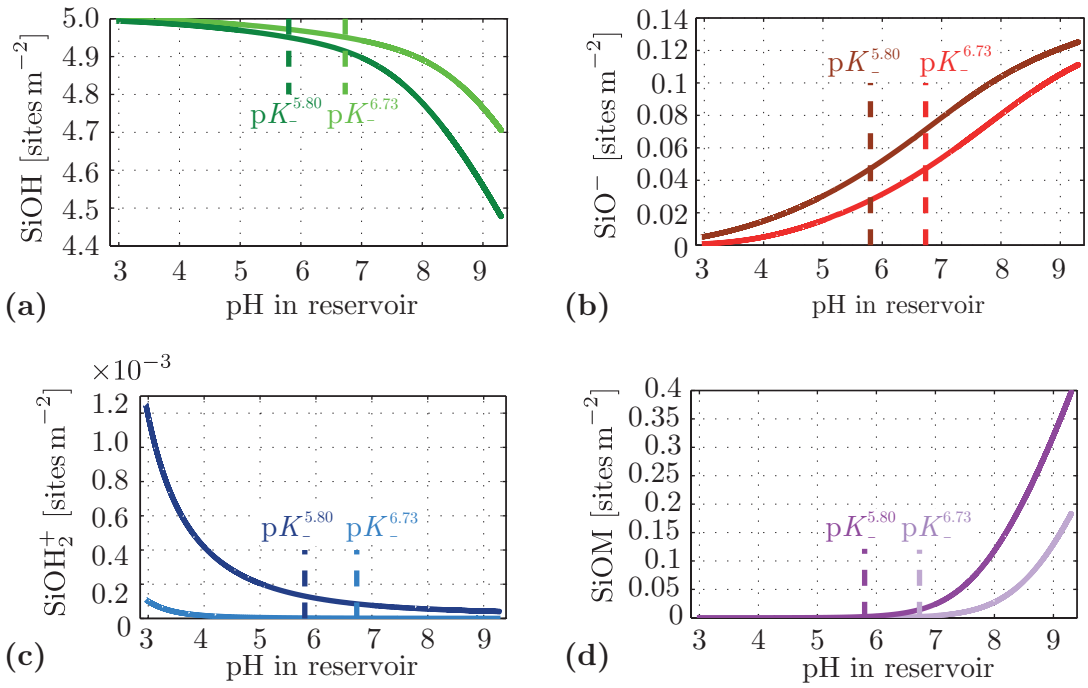

Figure 3.5: **(a)** SiOH, **(b)** SiO^-, **(c)** $SiOH_2^+$, and **(d)** SiOM site densities plotted versus bulk pH. In all plots pH is changed by adding NaOH or HCl to a 1 mM NaCl solution. Used model parameters are in Table 3.3. pK_-^x means $pK_- = x$.

3.6.2 Plots of Potentials, Surface Charge Densities, and Coverages

Plots of the potentials and surface charge densities versus the solution bulk pH is seen in Fig. 3.4 and plots of the coverages of all site states in Fig. 3.5. All plots show results for $pK_- = 6.73$ and $pK_- = 5.80$. Referring to Fig. 3.4(a) the size of the o-plane potential is for both pK_- values the highest potential as expected. Moreover, we expect the potential to decrease in size from the o-plane to the d-plane because this corresponds to moving away from the charged silica surface toward the bulk, which is in good agreement with the plots.

First, we will explain the pH dependence of the system versus bulk pH. In Fig. 3.5(b) it is seen that the density of SiO^- sites increases with pH (red curves). A higher density of negative sites on the silica surface creates more sites for metal cation adsorption so the surface charge density in the β-plane δ_β is expected to increase as well, see the green curves in Fig. 3.4(b). In general, when more negative sites are created the charge density δ_o on the silica surface must become more negative, see the blue curves in Fig. 3.4(b). Finally, when more SiO^- sites are created when increasing the bulk pH the number of positive $SiOH_2^+$ sites must decrease, see Fig. 3.5(c), which is in agreement with our discussion in the previous section.

We now explain the observed change in pH dependence of the system when pK_- is lowered. From the discussion in the previous section we know that lowering the pK_- value will in general lead to a higher density of SiO^- sites and hence a more negative δ_o over the pH range of interest which is seen in Fig. 3.4(b) as the blue dashed curve being more negative than the blue full curve. A more negative wall increases the number of screening ions in the diffusive layer so δ_d will increase as verified by the red dashed curve being greater than the red full curve in the figure. With a more negative wall the number of adsorbed metal cations in the β-layer increases so δ_β will increase as verified by the green dashed curve being greater than the green full curve in the figure. Finally, we note that a lower pK_- value leads to a more negative ϕ_d potential, i.e. ζ potential, see Fig. 3.4(a). We note that for p$K_- = 6.73$ and pH $\simeq 8.8$ there is as much charge from the adsorbed metal ions as there is charge from the ions in the diffusive layer screening the silica surface with a surface charge density of ~ 16 mC m^{-2}. The same situation occurs at pH $\simeq 7.7$ for p$K_- = 5.8$ with close to the same surface charge density.

We now turn to the plots of the site densities seen in Fig. 3.5. From Fig. 3.5(a) we observe that the density of neutral sites decreases with pK_-. This is a result of the increased number of SiO^- sites, see Fig. 3.5(b), relative to SiOH sites, as expected from Eq. (3.53). From Fig. 3.5(c) we can now confirm our statement in the beginning of Section 3.6 that the density of positive $SiOH_2^+$ sites is orders of magnitude lower than the other site densities. We note that at pH = 3 the $SiOH_2^+$ site density for p$K_- = 5.80$ is 12 times larger than that obtained from p$K_- = 6.73$. Fig. 3.5(d) shows the increased metal ion adsorption with pH which is a result of the increased SiO^- site density.

3.7 pH Profiles in Silica Nanochannels

In this section we will study how the pH varies in a channel and to our best knowledge be the first to introduce the concept of weighted pH in a channel.

As discussed in Section 3.1.2 the concentration of hydrons in an aqueous solution determine the pH. The hydrons in the nanochannel are assumed Boltzmann distributed with respect to the thermal energy k_BT and the transverse electric potential energy $e\phi(z)$. When the ζ potential is non-zero, $\phi(z)$ varies with z and hence the hydron concentration will vary with z. Therefore, inside the nanochannel there will be a spatially varying pH transverse to the channel walls given by

$$\mathrm{pH}(z) = -\log_{10}\left[c_H(z)\right] = \mathrm{pH_b} + \frac{e}{k_BT\ln(10)}\phi(z), \tag{3.55}$$

where $\mathrm{pH_b}$ is the bulk pH. A plot of the transverse pH profile (red full) is seen in Fig. 3.6 with the bulk pH level (red dashed) for a 100 nm high channel with negatively charged walls. $\phi(z)$ is solved using the ζ potential calculated from the metal adsorption model and the procedure for solving the potential profile transverse the channel is discussed in Appendix A.6. We have carried out a convergence study of the numerically solved potential in Appendix A.6.2. The hydrons are counterions and spend most time near the

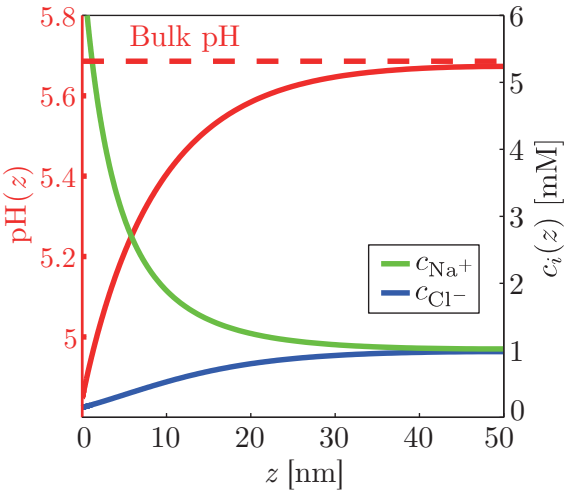

Figure 3.6: Plot of the pH profile (red full) with the bulk pH level (red dashed) in a 100 nm high channel containing a 1 mM NaCl solution and absorbed CO_2 together with concentration profiles of sodium (green) and chloride (blue) ions. The ζ potential was calculated to -49.4 mV. Used model parameters are in Table 3.3.

i	CO_3^{2-}	Cl^-, HCO_3^-	H_2CO_3	Na^+
Z_i	-2	-1	0	1
$\langle pH \rangle_i$	5.61	5.56	5.47	5.31
pH_b	5.68			

Table 3.4: Weighted pH values for a 1 mM NaCl solution with absorbed CO_2 for different ionic valences. Bulk pH is shown in the bottom row. $Z_i = 0$ is equivalent to the mean pH of the channel. The channel height is 100 nm. Used model parameters are in Table 3.3.

silica surface. Hence, all counterions experience a lower pH on average. This is seen in the figure where the counterion Na^+ (green) has a high concentration in a low pH region near the channel surface. The co-ions are expelled from the wall and in this case experience a higher pH than counterions on average. This is seen in the figure where the co-ion Cl^- (blue) has a high concentration in a high pH region near the mid channel. Conversely, if the channel walls are positive the hydrons are co-ions and spend more time in the center of the channel so the pH will be higher near the wall. Consequently, on average, counter-ions experience a higher pH than co-ions. Due to the spatially varying pH profile we cannot assign to each particle a single pH value felt inside the nanochannel using only the classical definition of pH in Eq. (3.55). However, by weighting each particle's concentration with the surrounding hydron concentration throughout the channel we are able to assign one weighted pH to each particle describing the amount of hydrons experienced by each particle on average:

$$\langle \mathrm{pH} \rangle_i \equiv -\log_{10}\left(\frac{\int_0^h c_\mathrm{H}(z) c_i(z) \mathrm{d}z}{\int_0^h c_i(z) \mathrm{d}z} \right), \tag{3.56}$$

where h is the nanochannel height. All ions are assumed Boltzmann distributed and the channel is symmetric around $z = h/2$ so

$$\begin{aligned}\langle \mathrm{pH}\rangle_i &= -\log_{10}\left\{\frac{\int_0^{\frac{h}{2}} c_{\mathrm{H}}^{\mathrm{b}} \exp\left[-\frac{e}{k_{\mathrm{B}}T}\phi(z)\right] c_i^{\mathrm{b}} \exp\left[-\frac{Z_i e}{k_{\mathrm{B}}T}\phi(z)\right] \mathrm{d}z}{\int_0^{\frac{h}{2}} c_i^{\mathrm{b}} \exp\left[-\frac{Z_i e}{k_{\mathrm{B}}T}\phi(z)\right] \mathrm{d}z}\right\} \\ &= \mathrm{pH}_{\mathrm{b}} - \log_{10}\left\{\frac{\int_0^{\frac{h}{2}} \exp\left[-\frac{(1+Z_i)e}{k_{\mathrm{B}}T}\phi(z)\right] \mathrm{d}z}{\int_0^{\frac{h}{2}} \exp\left[-\frac{Z_i e}{k_{\mathrm{B}}T}\phi(z)\right] \mathrm{d}z}\right\}, \end{aligned} \tag{3.57}$$

which for a neutral particle reduces to

$$\langle \mathrm{pH}\rangle_i = \mathrm{pH}_{\mathrm{b}} - \log_{10}\left\{\frac{2}{h}\int_0^{\frac{h}{2}} \exp\left[-\frac{e}{k_{\mathrm{B}}T}\phi(z)\right] \mathrm{d}z\right\} \quad \text{(neutral particle)}. \tag{3.58}$$

We note that the weighted pH is independent of the ith ion's bulk concentration but depends on its valence. In Table 3.4 we have provided values of the weighted pH for the particles present in the system shown in Fig. 3.6 calculated from the script in Appendix C.5. Since the particle with zero valence is evenly distributed throughout the channel it experiences what can be thought of as an average pH which in this case is 5.47. The negative co-ions experience a higher pH and the positive counterion a lower pH than the average value which is expected from the previous discussion. Also, since the ion with largest negative valence is expelled most from the wall it here experiences the highest pH. We note that with a negatively charged wall the weighted pH of any negative ion can never exceed that of the bulk since the hydron concentration anywhere in the channel will always be that in the bulk or higher.

The silica nanochannel pH profile is one of the subjects of current research in the UCSB Nanolab, where the intensity of charged fluorescent quantum dots in silica nanochannels are being used to measure the pH using total internal reflection fluorescence.

3.8 Chapter Summary

In this chapter we started out by discussing how to calculate the solute concentrations of all species dissolved in an aqueous solution, we introduced the concept of pH, and we discussed how to account for CO_2 absorption in our system. We moved on to discussing the system consisting of a silica nanochannel contacting an electrolyte. We discussed the assumptions used to simplify the system summarized in Table 3.1. We continued deriving our two models of the system starting with the 2pK-model Eq. (3.26) with input/output parameters in Table 3.2 followed by the metal adsorption model Eqs. (3.33), (3.35), (3.43), and (3.44) with input/output parameters in Table B.4 in Appendix B. We then discussed coating of silica nanochannels with aminosilane and how to implement it in the 2pK-model. We studied how the potentials, surface charge densities, and coverages calculated from the metal adsorption model depend on pH and pK_-. By decreasing pK_- the ratio of negatively charged sites to neutral sites increased which lowered δ_{o} and the ϕ_{d} potential i.e. the ζ

potential. We then studied how the pH varied transverse to negatively charged walls in a nanochannel see Fig. 3.6 and introduced the weighted pH Eq. (3.57) in order to, with a single value, describe the hydron concentration experienced by each particle on average. Table 3.4 gives the weighted pH values for particles of different valences in the nanochannel.

Chapter 4

Electrical Conductance of Nanochannels

In this chapter we study the conductance dependence on KCl bulk concentration in a silica nanochannel for a solution containing KCl dissolved in deionized water with absorbed CO_2 from atmosphere exposure. The system can be seen with channel dimensions $h \times w \times L =$ 200 nm $\times$ 5 µm $\times$ 1.2 cm and defining parameters in Fig. 4.1. The channel geometry is chosen based on the channels used in the experiments described in Chapter 5. We will use the 2pK-model developed in Section 3.3 to calculate the ζ potential, and from this, the steady state potential distributions used in the conductance calculations. When calculating the surface charge density in the diffusive layer δ_{d} for the 2pK-model in Section 3.3 the electric potential in the center of the channel ϕ_{m} was assumed zero confer Eq. (2.28). In other words, we assumed no diffuse layer overlap equivalent to assuming $\lambda_{\mathrm{D}} \ll h$ but this assumption will generally not hold for nanochannels containing a solution of very low bulk concentrations[1] ($\lesssim$ 0.1 mM). In the present chapter we will calculate the conductance for very low bulk concentrations which leads to very high Debye lengths so we need to account for diffusive layer overlap. In Appendix A.9 we present a method of how to include diffusive layer overlap in the 2pK-model by self-consistently calculate ϕ_{m} when solving the ϕ_{d} potential. Due to the CO_2 absorption the bulk pH is 5.68 confer Section 3.1.3. We will show that the bulk pH becomes important for the nanochannel conductance behavior at low salt concentrations. The conductance of a nanochannel has been reported in the literature to plateau for low KCl bulk concentrations [21, 22]. We will show that the 2pK-model leads to the same conclusion and furthermore that it predicts a conductance valley before the plateau which has not yet been predicted by any other model to our best knowledge. The reason why, is that the absorption of CO_2 is seldom taken into account in the literature and most models neglect the presence of inherent hydrons and hydroxide ions in the water, even for salt concentrations below the lowest concentration of either of these [2, 3, 21, 22]. We will show that for low KCl bulk concentrations the presence of hydrons in a silica nanochannel is essential in describing the plateau regime.

[1] A 0.1 mM KCl solution has a Debye length of about 30 nm. For deionized water with absorbed CO_2 $\lambda_{\mathrm{D}} \sim 211$ nm (pH = 5.68). Without absorbed CO_2 $\lambda_{\mathrm{D}} \sim 963$ nm (pH = 7.00).

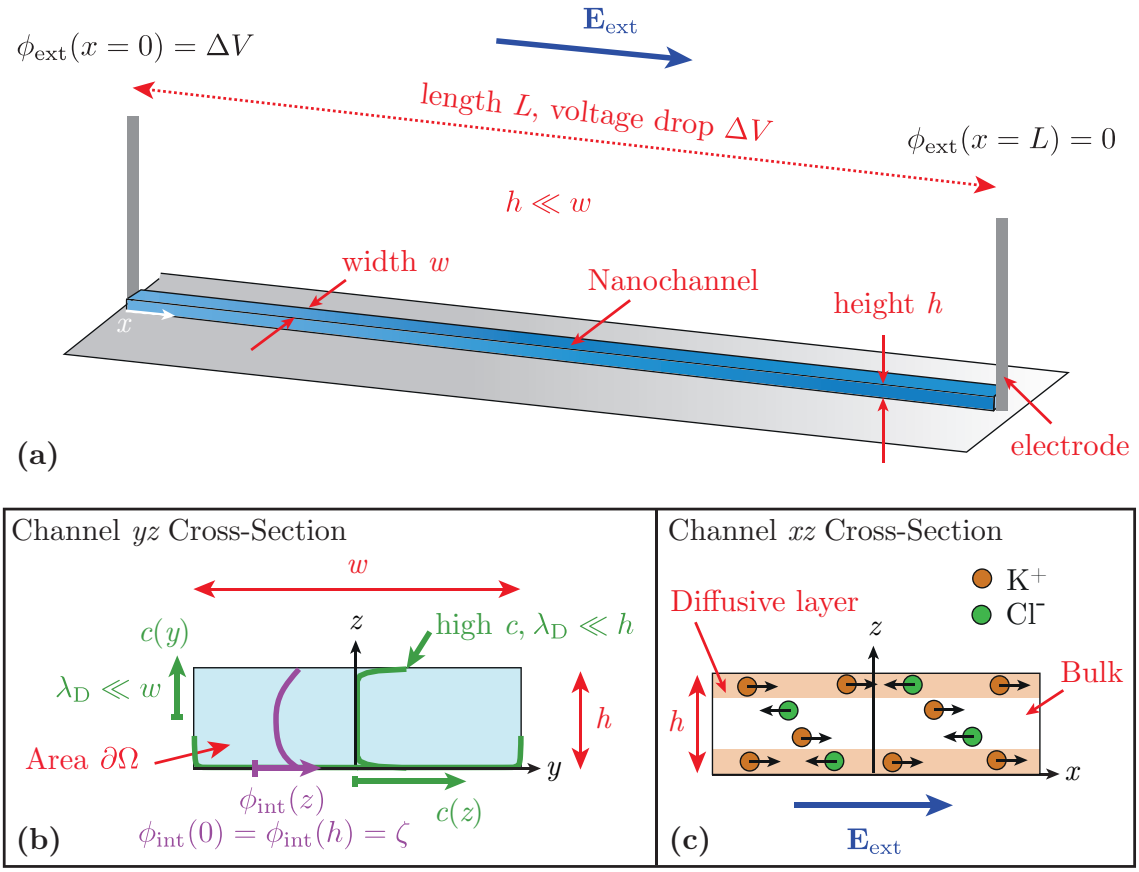

Figure 4.1: **(a)** a high aspect ratio silica rectangular nanochannel with metal electrodes at each end containing a solution of KCl dissolved in deionized water exposed to the atmosphere (reservoirs are not shown). Channel dimensions are defined together with the electric field and potentials. The x-direction is shown in the left side of the channel. **(b)** yz cross-section with area $\partial\Omega$ of the nanochannel showing the concentration profile along the large channel width in the y-direction where $\lambda_{\text{D}} \ll w$ and the concentration profile along the shallow channel height in the z-direction for a high KCl bulk concentration where $\lambda_{\text{D}} \ll h$. The internal potential $\phi_{\text{int}}(z)$ is shown. **(c)** xz cross-section showing the potassium counterions (orange circles) and chloride co-ions (green circles) in the bulk region and diffusive layer region. The direction of the external electric field $\mathbf{E}_{\text{ext}}$ is shown in the bottom (dark blue arrow) and the black arrows with center in each ion show the direction of movement due to the applied field.

4.1 Conductance of a Rectangular Nanochannel

In this section we will derive the conductance for the rectangular nanochannel shown in Fig. 4.1. The following discussion refers to parameters shown in the figure. The channel has a high aspect ratio $h \ll w$ so we assume that the ions in the channel only interact with the two nearest walls separated by a distance h transverse to the flow direction. The potential due to the charged channel walls therefore only depends on z and is denoted the internal potential $\phi_{\text{int}}(z)$. Metal electrodes are positioned at each end of the channel and when a voltage ΔV is applied between them an external electric field $\mathbf{E}_{\text{ext}}$ is set up in the longitudinal channel direction x such that the associated external potential $\phi_{\text{ext}}(x = 0) = \Delta V$ at the beginning of the channel and $\phi_{\text{ext}}(x = L) = 0$ at the end. Electrochemical processes will occur at the metal electrodes such that no screening diffusive layers are set up around them and the current will keep flowing. We therefore assume that the external potential ϕ_{ext} does not affect the distribution of ions in the channel. Neglecting fringe effects we can assume a translationally invariant ion distribution in the xy-plane. This implies a constant ζ potential along the wall, that the charge density is given by

$$\rho_{\text{el}}(z) = -\epsilon \partial_z^2 \phi_{\text{int}}(z), \tag{4.1}$$

and that the external electric field is constant along the channel and is given by

$$\mathbf{E}_{\text{ext}} = -\boldsymbol{\nabla}\phi_{\text{ext}} = \frac{\Delta V}{L}\mathbf{e}_x. \tag{4.2}$$

The conductance is the ability of a system to conduct an electric current defined by the ratio of a current through the system to the potential difference across it

$$S \equiv \frac{I}{\Delta V}. \tag{4.3}$$

The external electric field yields two contributions to the electrical current in the nanochannel. First, the field sets in motion the electrolyte ions creating an electric current called the electromigration current I_{mig}. In the neutral bulk there are on average as many ions moving in one direction as oppositely charged ions in the other, resulting in no net movement of the bulk liquid, see Fig. 4.1(c). In the non-neutral diffusive layers more counterions are moved in one direction as co-ions in the other. Stokes drag between the moving particles and the liquid accelerates the diffusive layers which begin to move relative to the bulk. The movement of the diffusive layer relative to the charged channel surface induced by the external electric field is known as electroosmosis. Viscous forces between the liquid in the diffusive layers and the liquid in the bulk accelerates the bulk into motion creating an additional contribution to the current through its advection called the electric advection current I_{adv}. Therefore, the total conductance is the sum of the migration conductance S_{mig} and the advection conductance S_{adv}

$$S_{\text{tot}} = S_{\text{mig}} + S_{\text{adv}} = \frac{I_{\text{mig}}}{\Delta V} + \frac{I_{\text{adv}}}{\Delta V}. \tag{4.4}$$

In the following sections we derive the migration and advection conductance contributions.

4.1.1 Electromigration Conductance

The electromigration current is found by integrating the electromigration current density $\mathbf{J}_{\text{mig}}$ given by Eq. (2.3d) over the cross-sectional area of the channel $\partial\Omega$,

$$I_{\text{mig}} = \int_{\partial\Omega} \mathbf{J}_{\text{mig}} \cdot \mathrm{d}\mathbf{A} = \int_{-\frac{w}{2}}^{\frac{w}{2}} \int_0^h \sigma_{\text{el}}(z) E_{\text{ext}} \, \mathrm{d}z\mathrm{d}y = 2\Delta V \frac{w}{L} \int_0^{\frac{h}{2}} \sigma_{\text{el}}(z) \, \mathrm{d}z, \tag{4.5}$$

where the last equality follows from the electric conductivity $\sigma_{\text{el}}(z)$ being symmetric around the center of the channel at $z = h/2$ due to the symmetry in the internal electric potential $\phi_{\text{int}}(z)$, see Fig. 4.1(b). The electromigration conductance contribution is then

$$S_{\text{mig}} = \frac{I_{\text{mig}}}{\Delta V} = 2\frac{w}{L} \int_0^{\frac{h}{2}} \sigma_{\text{el}}(z) \, \mathrm{d}z. \tag{4.6}$$

The conductivity $\sigma_{\text{el}}(z)$ of a single ion of concentration $c(z)$, valence Z, and mobility μ is $\sigma_{\text{el}}(z) = |Z|e\mu c(z)$. For $\mathcal{N}$ ions the conductivity inside the channel is

$$\sigma_{\text{el}}(z) = e \sum_{i=1}^{\mathcal{N}} |Z_i| \mu_i c_i(z) = e \sum_{i=1}^{\mathcal{N}} |Z_i| \mu_i c_i^{\text{b}} \exp\left(-\frac{Z_i e}{k_{\text{B}} T} \phi_{\text{int}}(z) \right), \tag{4.7}$$

where we have assumed the ions Boltzmann distributed.

4.1.2 Advection Conductance

The resulting velocity throughout the channel due to electroosmotic effects is called the electroosmotic velocity. The Navier–Stokes equation Eq. (2.6) can be solved in steady state $\partial_t \mathbf{v}(z) = \mathbf{0}$ in a rectangular channel with an externally applied electric field in the x direction and no-slip condition at the walls $v_x(z = 0) = 0$ and $v_x(z = h) = 0$. Due to the high aspect ratio $h \ll w$ we can approximate the system as a parallel plate channel and the electroosmotic velocity becomes

$$\mathbf{v}(z) = v_x(z)\mathbf{e}_x = \left[\phi_{\text{int}}(z) - \zeta \right] \frac{\epsilon}{\eta} \mathbf{E}_{\text{ext}}, \tag{4.8}$$

where we have used the charge density Eq. (4.1) in the electric force density and the boundary conditions $\phi_{\text{int}}(0) = \phi_{\text{int}}(h) = \zeta$. The electric advection current is

$$I_{\text{adv}} = \int_{\partial\Omega} \mathbf{J}_{\text{adv}} \cdot \mathrm{d}\mathbf{A} = \int_{\partial\Omega} \rho_{\text{el}}(\mathbf{r}) \mathbf{v}(\mathbf{r}) \cdot \mathrm{d}\mathbf{A}. \tag{4.9}$$

For $\lambda_{\text{D}} \ll w$ the electroosmotic velocity for the rectangular channel is to good approximation given by Eq. (4.8). Together with the general charge density for $\mathcal{N}$ ions Eq. (2.21) we get

$$I_{\text{adv}} = 2\Delta V \frac{w}{L} \frac{e\epsilon}{\eta} \int_0^{\frac{h}{2}} \left[\phi_{\text{int}}(z) - \zeta \right] \sum_{i=1}^{\mathcal{N}} Z_i c_i(z) \, \mathrm{d}z, \quad \lambda_{\text{D}} \ll w. \tag{4.10}$$

The advection conductance of the rectangular channel immediately follows

$$\begin{aligned} S_{\text{adv}} &= \frac{I_{\text{adv}}}{\Delta V} \\ &= 2\frac{w}{L}\frac{e\epsilon}{\eta}\int_0^{\frac{h}{2}} \left[\phi_{\text{int}}(z)-\zeta\right] \sum_{i=1}^{\mathcal{N}} Z_i c_i^{\text{b}} \exp\left(-\frac{Z_i e}{k_{\text{B}}T}\phi_{\text{int}}(z)\right) \mathrm{d}z, \quad \lambda_{\text{D}} \ll w. \end{aligned} \tag{4.11}$$

The total conductance S_{tot} Eq. (4.4) for the high aspect ratio rectangular channel is the sum of the electromigration conductance Eq. (4.6) and the advection conductance Eq. (4.11).

A script that calculates the total conductance of the rectangular channel given the ζ potential, internal potential profile $\phi_{\text{int}}(z)$, bulk ionic concentrations, and ionic valences can be found in Appendix C.6.

4.1.3 Conductance in the Bulk Regime

For a high concentration solution with $c \gtrsim 10$ mM the Debye length is much smaller than the height $\lambda_{\text{D}} \ll h$ so the diffusive layers are very thin[2] and the bulk dominates the channel. Therefore, a nanochannel containing an electrolyte of large concentration is referred to as being in the bulk regime. In such a nanochannel the internal potential $\phi_{\text{int}}(z)$ is approximately zero everywhere and the electromigration conductance Eq. (4.6) can be approximated by

$$S_{\text{mig}} \approx \frac{wh}{L} e \sum_{i=1}^{\mathcal{N}} |Z_i| \mu_i c_i^{\text{b}}. \tag{4.12}$$

In the bulk ρ_{el} is zero due to charge neutrality confer Eq. (2.29). Therefore, from Eq. (4.9) it follows that the advection conductance for a nanochannel with a high concentration electrolyte is approximately zero,

$$S_{\text{adv}} \approx 0. \tag{4.13}$$

The total conductance in the bulk regime is therefore given by

$$S_{\text{tot}} = S_{\text{mig}} + S_{\text{adv}} = \frac{wh}{L} e \sum_{i=1}^{\mathcal{N}} |Z_i| \mu_i c_i^{\text{b}} \equiv S_{\text{bulk}} \quad \text{(bulk regime)}. \tag{4.14}$$

The conductance in the bulk regime for a solution with KCl of high concentration is dominated by potassium and chloride ions and is given by

$$S_{\text{bulk}}^{\text{KCl}} = \frac{wh}{L} e \left(\mu_{\text{K}^+}\ c_{\text{K}^+}^{\text{b}} + \mu_{\text{Cl}^-}\ c_{\text{Cl}^-}^{\text{b}}\right), \tag{4.15}$$

A MatLab script calculating the bulk conductance is provided in Appendix C.7. The mobilities of all modeled ions are found in Table B.2 in Appendix B and we assume them

[2] The Debye length of a 10 mM monovalent electrolyte is ≈ 3 nm, see Fig. A.8 in Appendix A.7.

to be independent of the ionic strength which is justified for low salt concentrations. For high salt concentrations the ionic mobilities decrease. As an example consider a KCl solution. The assumption leads to errors in the conductivity[3] of 5.4 % for 10 mM and 17 % for 100 mM confer Appendix A.8.

4.2 Conductance Characteristics of a Nanochannel

In this section we numerically calculate the nanochannel conductance versus KCl bulk concentration. The bulk concentraton of KCl used in the calculations range from 1 M down to 0.1 µM. The channel is in a bulk regime from 1 M to ≈10 mM so here the surface conditions of the channel do not influence the conductance. However, for lower concentrations the channel surface begins to influence the conductance and since the salt concentration is very low here, we can neglect the adsorption of metal cations and therefore use the simpler 2pK-model in the conductance calculation. Furthermore, we will characterize the behavior of the conductance curve and discuss the reasons for its shape in the entire concentration range. The nanochannel conductance for a given KCl bulk concentration is calculated by following the steps

1 Use our modified Santiago script in Appendix C.1 to determine the bulk pH and the actual concentrations of all charge states of the species in the electrolyte, see Section 3.1.

2 Solve the 2pK-model self-consistently for the ζ potential using a start guess taking into account diffuse layer overlap as discussed in Appendix A.9 from which the internal potential profile $\phi_{\text{int}}(z)$ is calculated in the channel confer Appendix A.6.

3 The channel conductance is calculated from the potential profile in step 2 using Eqs. (4.6) and (4.11) in the total channel conductance Eq. (4.4).

The conductance versus KCl bulk concentration together with the bulk conductance of KCl $S_{\text{bulk}}^{\text{KCl}}$ is shown in Fig. 4.2. The inset shows how the ζ potential varies over the same concentration range. Consistent with literature the conductance of the nanochannel plateaus for low salt concentrations. In the figure we have labeled four characteristic regimes on the conductance curve: the bulk regime, the departure, the valley, and the plateau. We have, for the first time in literature, defined these regimes in Fig. 4.3(f). The bulk regime is the part of the conductance curve which follows the bulk salt conductance curve. The departure regime begins where the channel conductance deviates more from the bulk conductance than a specified tolerance. It ends where the conductance curve intersects the conductance level for an infinite dilute salt solution i.e. intersects the plateau level. The valley begins in the point where the departure ends and ends where the relative difference between the conductance curve and plateau level is less than a specified tolerance. Previous models in literature only show three regimes: the bulk regime, the departure, and the plateau [21, 22].

[3]The conductivity of a high concentration KCl solution is $\sigma_{\text{el,KCl}} = e\big(\mu_{\text{K+}}\ c_{\text{K+}} + \mu_{\text{Cl-}}\ c_{\text{Cl-}}\big)$. The error in conductivity originates from the changed mobilities.

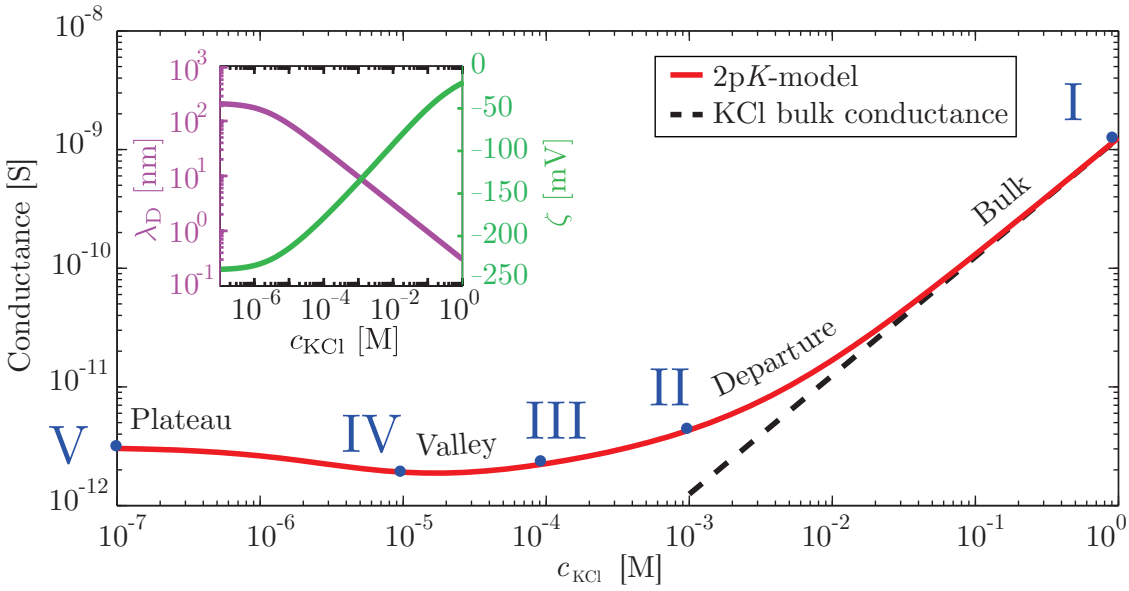

Figure 4.2: A log-log plot of nanochannel conductance versus KCl bulk concentration (red) together with the KCl bulk conductance $S_{\mathrm{bulk}}^{\mathrm{KCl}}$ (black dashed) calculated by the 2pK-model in Section 3.3 for KCl and absorbed CO_2 in deionized water. Four conductance regimes are marked: bulk regime, departure, valley, and plateau. These regimes are defined in Fig. 4.3(f). The blue roman numerals match with those in Fig. 4.3. The inset shows how the ζ potential and the Debye length λ_{D} varies with concentration. The mobilities and model parameters can be seen in Table B.2 and Table B.3, respectively, in Appendix B. The channel dimensions are $h \times w \times L = 200$ nm $\times$ 5 µm $\times$ 1.2 cm.

4.2.1 Concentration Profiles

We can explain the conductance valley and subsequent plateau region from the transverse concentration profiles of ions in the nanochannel for different KCl bulk concentrations. These profiles have been plotted in Fig. 4.3(a)–(e) with roman numerals matching those in Fig. 4.2 for different concentrations. Some of the curves stated in the legend are not visible on the graph due to too low concentrations.

Ions contribute to the conductance through their concentration, valence, and mobility. Therefore, an ion of low concentration does not necessarily has a low influence on the conductance if it has a large mobility. Furthermore, since the ζ potential becomes increasingly negative for lower salt concentrations, confer the inset in Fig. 4.2, only the positive hydrons and potassium ions are dominating the conductance through their elevated concentrations. Based on this, in order to determine which ion dominates the conductance, we have added curves in Fig. 4.3(a)–(e) showing the concentration of hydrons scaled with the ratio of hydron mobility to potassium mobility $c_{\mathrm{H}}\ \mu_{\mathrm{H^+}}/\mu_{\mathrm{K^+}}$.

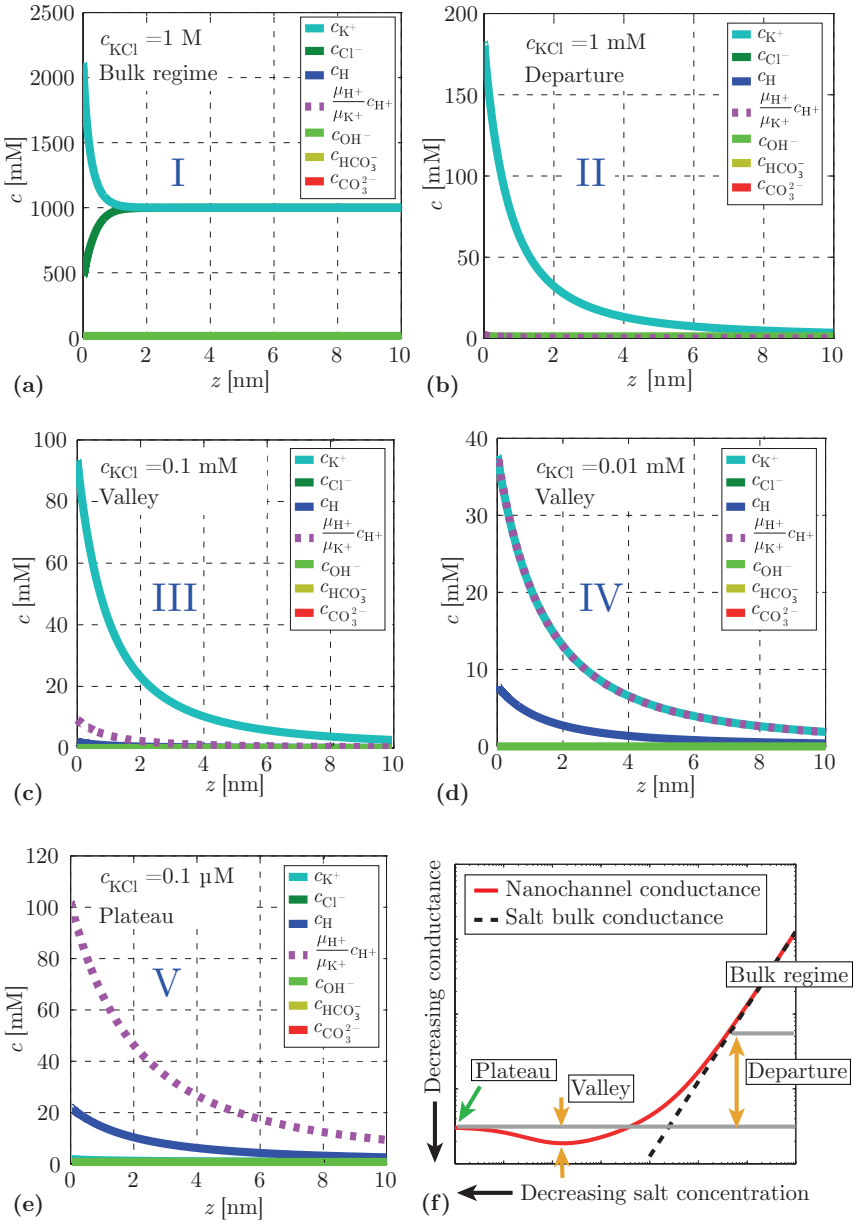

Figure 4.3: Nanochannel ionic concentration profiles for KCl bulk concentrations of, **(a)** 1 M, **(b)** 1 mM, **(c)** 0.1 mM, **(d)** 0.01 mM, and **(e)** 0.1 µM. Some of the curves stated in the legend are not visible on the graph due to too low concentrations. The dashed curve shows the concentration of hydrons scaled with the ratio of hydron mobility to potassium mobility. The blue roman numerals match with those in Fig. 4.2. The bulk regime, departure, valley, and plateau match those conductance regimes defined in Fig. 4.2. The mobilities and model parameters can be seen in Table B.2 and Table B.3, respectively, in Appendix B. The channel has height $h = 200$ nm. **(f)** shows our definitions of the four characteristic regimes on the conductance curve: bulk regime, departure, valley, and plateau.

The departure from the bulk conductance can be explained from the concentration profiles governed by the ζ potential and the Debye length λ_D. The ζ potential lifts up the counterion concentration mainly within a Debye length distance from the wall and the Debye length is the distance from the wall over which the counterion concentration is elevated. Both the ζ potential and Debye length λ_D increase in size with decreasing KCl bulk concentration as shown in the inset in Fig. 4.2. The ζ potential becomes more negative because a decrease in ionic bulk concentrations c_i^b decreases the size of the surface charge density δ_o confer Eq. (3.26a). Physically this is because the same surface charge density cannot be sustained with a lower number of screening ions. When the size of δ_o decreases the capacitor relation Eq. (3.21) states that ϕ_d and ϕ_o approach each other. Since the size of ϕ_o is larger than ϕ_d the equation can be satisfied by increasing the size of ϕ_d i.e. the ζ potential. So, physically when the bulk concentration is reduced screening of the wall becomes harder but the wall can counteract this by becoming less negative. This, together with an increasingly negative ζ potential attracting more counterions makes the screening easier.

In the bulk regime the conductance is dominated by the chloride and potassium ions as shown in Fig. 4.3(a). The conductance will here follow the KCl bulk conductance confer Section 4.1.3 which decreases with the KCl bulk concentration. The conductance departure from bulk occurs when the size of the ζ potential has lifted up the potassium ion concentration close to the wall to counteract the decrease in potassium ion bulk concentration. When the bulk concentration decreases the diffusive layer increases expelling chloride coions leaving potasssium counterions to dominate the conductance as is seen in Fig. 4.3(b).

A further decrease in KCl bulk concentration increases the size of the ζ potential sufficiently to elevate the hydron concentration as shown in Fig. 4.3(c). Now the hydrons begin to contribute to the conductance as shown by the appearance of the graph $c_H\ \mu_{H^+}/\mu_{K^+}$ (dashed line). The bulk concentration of hydrons is fixed in the solution so as the size of the ζ potential increases the concentration of hydrons is elevated and at some point begins to take over the dominating role in conductance increasing this from the valley to the plateau see Fig. 4.2. As shown in Fig. 4.3(d) the hydrons and potassium ions contribute equally to conductance at a KCl bulk concentration of ≈ 0.01 mM. For low enough KCl bulk concentrations the decreasing potassium ion concentration becomes negligible compared to the constant bulk hydron concentration and both the ζ potential and λ_D plateaus see Eq. (3.26) and Eq. (2.33), respectively. At this point the conductance dominating ions are only the hydrons as shown in Fig. 4.3(e).

We now estimate whether it is the ζ potential or Debye length λ_D which has the greatest effect on the deviation from the bulk conductance. We will approximate the concentration profiles in Fig. 4.3(a) (1 M KCl) and Fig. 4.3(b) (1 mM KCl) as rectangles shown as the blue areas in Fig. 4.4(a) and Fig. 4.4(b), respectively. The roman numerals in the top of the figure match those in Fig. 4.2. The bottom rectangle (dark blue) represents the bulk concentration and the top rectangle (light blue) delineated with a red dashed line is the elevated concentration of counterions above the bulk. In Fig. 4.4(a) the bulk area is multiplied by a factor of 2 because it is the concentration of both potassium and chloride

ions. Note that we are only interested in orders of magnitude so we have approximated the chloride concentration to equal its bulk value throughout the channel. The area of each rectangle area can be related to its contribution to the conductance. The top level of the light blue rectangle

$$c_{\mathrm{KCl}} \exp\left(-\frac{e}{k_{\mathrm{B}}T}\zeta\right), \tag{4.16}$$

representing the elevated counterion concentration is governed by the KCl bulk concentration[4] and ζ potential, and its width by the Debye length $\lambda_{\mathrm{D}} \propto (c_{\mathrm{KCl}})^{-1/2}$ illustrated by the green arrows in Fig. 4.4(b). When decreasing the KCl bulk concentration 3 orders of magnitude from 1 M Fig. 4.4(a) to 1 mM Fig. 4.4(b) the Debye length increases with a factor of 30 from 0.3 nm to 10 nm. It is seen that the elevated concentration level is reduced with one order of magnitude from 2000 to 200. All things being equal, a downscaling of the KCl bulk concentration by 3 orders of magnitude would reduce the level from 2000 to 2 so the ζ potential has opposed the concentration reduction with a factor of 100. The area of the elevated concentration rectangle is related to the deviation of the conductance from the bulk so we have thereby demonstrated that the increasingly negative ζ potential has a greater effect (a factor of 100 here) on the conductance curve deviation from the bulk than the increased Debye length (a factor of 30 here).

Finally, we compare the ratio of the conductance contribution from the elevated concentration to that of the bulk concentration at 1 M to the same ratio at 1 mM by calculating the areas of the rectangles. At 1 M Fig. 4.4(a) the ratio is

$$\frac{1000\ \mathrm{mM} \times 0.3\ \mathrm{nm}}{2 \times 1000\ \mathrm{mM} \times 100\ \mathrm{nm}} = 1.5 \times 10^{-3}, \tag{4.17}$$

and at 1 mM Fig. 4.4(b) it is

$$\frac{200\ \mathrm{mM} \times 10\ \mathrm{nm}}{1\ \mathrm{mM} \times 100\ \mathrm{nm}} = 20. \tag{4.18}$$

The conductance contribution from the elevated concentration is 3 orders of magnitude lower than the bulk contribution at 1 M and at 1 mM it is one order of magnitude higher than the bulk contribution. This verifies that at high KCl bulk concentrations the conductance is dominated by the bulk concentration and at low KCl bulk concentrations it is dominated by the elevated counterion concentrations.

[4]We have $c_{\mathrm{KCl}} = c_{\mathrm{K}^+}$ under the assumption that KCl dissociates completely.

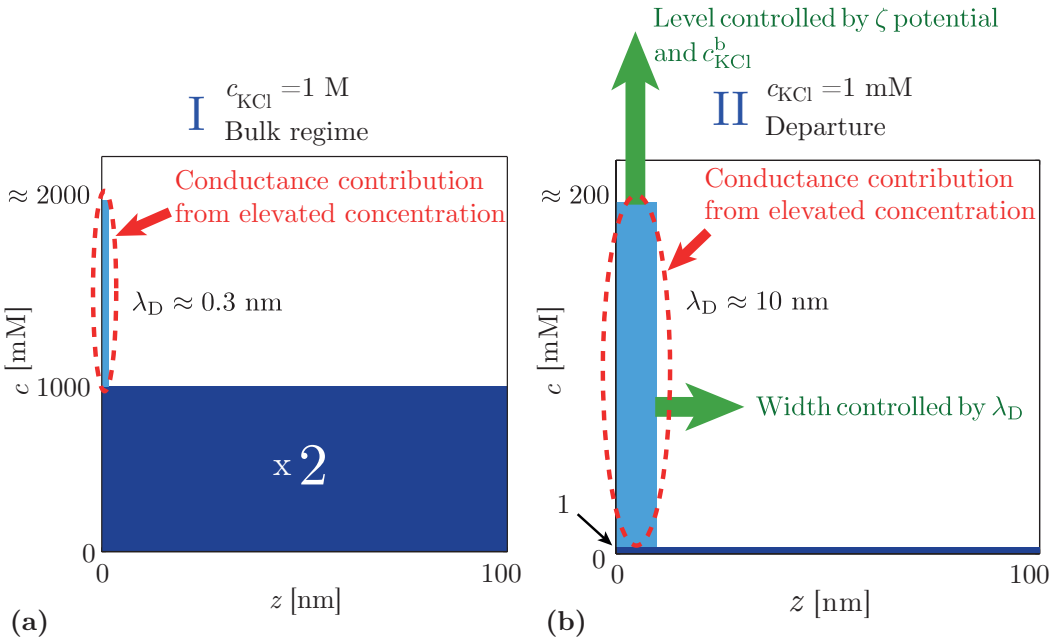

Figure 4.4: Nanochannel concentration profiles for **(a)** 1 M KCl bulk concentration and **(b)** 1 mM KCl bulk concentration approximated by rectangles. The actual concentration profiles for **(a)** and **(b)** are seen in Fig. 4.3(a) and Fig. 4.3(b), respectively. The roman numerals in the top of the figure match those in Fig. 4.2. The bottom rectangle (dark blue) represents the bulk concentration and the top rectangle (light blue) delineated with a red dashed line is the elevated concentration of counterions above the bulk. The top level of the light blue rectangle is governed by the KCl bulk concentration and ζ potential, and its width by the Debye length λ_D (green arrows in **(b)**). The figure is not drawn to scale.

4.2.2 Measuring the Conductance Valley

To experimentally measure the conductance valley seen in Fig. 4.2 data must be obtained requiring the ability to measure the conductance for very low concentrations. When the salt concentrations become sufficiently low the Debye length becomes so large that the concentration of counterions throughout the channel becomes very high. Outside the channel, in the bulk, the metal electrode is positioned and here the concentration of counterions is low equal to their bulk value. Therefore, a boundary is created at each end of the channel where one side of each boundary contains counterions of high concentration (counterions inside the channel) and the other side contains ions of low concentration (counterions in the reservoir). This gives rise to a Gibbs–Donnan effect creating an electric potential between the two concentration regions, i.e. from the reservoir to the channel. This interferes with the externally applied electric field through the nanochannel and impedes experimental measurements of the current. One way of avoiding this limitation would be by incorporating the metal electrodes inside the nanochannels which is the topic of current research in the UCSB Nanolab.

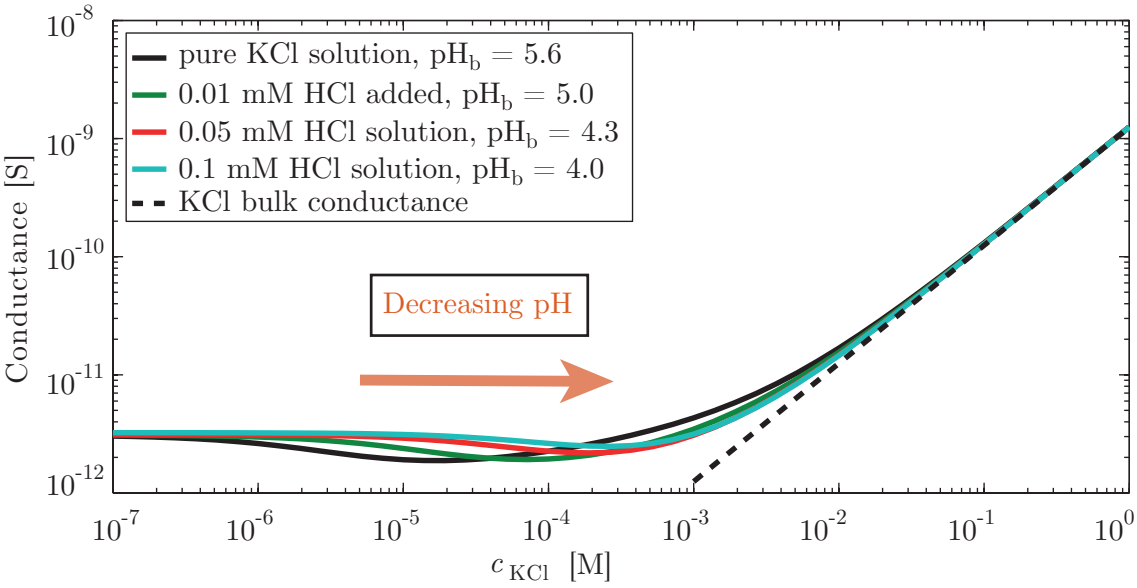

Figure 4.5: A log-log plot of the channel conductance versus KCl bulk concentration for different added concentrations of HCl together with the bulk conductance of KCl. The orange arrow with text box shows the displacement of the conductance curve when increasing the formal concentration of HCl and hence decreasing the bulk pH. The mobilities and model parameters can be seen in Table B.2 and Table B.3, respectively, in Appendix B. The channel has height $h = 200$ nm.

We will propose and carry out an experiment which moves the valley toward higher KCl bulk concentrations. The valley occurs because the dominating contribution to the conductance is shifted from the potassium ions with decreasing concentration to the elevated hydrons having a fixed bulk concentration. By increasing the bulk concentration of hydrons they will dominate the conductance earlier shifting the valley and plateau toward higher concentrations. Increasing the bulk hydron concentration is done by adding an acid. We choose HCl since it best resemblances the existing electrolyte composition. The effect on the conductance curve by adding HCl is shown in Fig. 4.5. Incidentally, the graph has been generated with a pK_- value of 2.8 due to early fitting results of our model to experimental data from the UCSB Nanolab. We later show that a more correct pK_- value for a bare silica nanochannel is near the literature value of 6.64 and in Section 5.4 we discuss possible reasons for the low pK_- value initially determined. Nevertheless, as expected the conductance valley shifts toward higher KCl concentrations when increasing the solution acidity but we see that the conductance valley becomes more shallow which is primarily due to the generally increased conductance from the additional hydrons. Finally, the plateau level increases slightly with acidity due to the extra added hydrons. In Section 5.2.2 we present data from a conductance measurement on a 165 nm high channel[5]

[5]The experiment was carried out in the UCSB Nanolab by Andrew Crumrine (May 2010).

with a KCl solution containing 0.1 mM HCl. The experimental data is found in Tables B.8 and B.9 in Appendix B.5.

4.3 Conductance Dependence on Parameters

For high salt bulk concentrations the Debye length is negligible compared to the channel height and the wall does not have any effect on the ions in the channel, see Section 4.1.3. Therefore, the model must as a first thing predict the right conductance in the bulk regime. The channel parameters affecting the conductance curve in the bulk regime are purely geometrical which can be seen directly from Eq. (4.14). However, discrepancies in the bulk regime between the calculated and the experimentally measured conductance can arise due to channel fabrication errors. We later have to fit the channel width to match the bulk conductance in the data set found in Table B.7, Table B.8, and Table B.9 in Appendix B.5.

In Appendix A.10 we study how the conductance curve behaves when separately neglecting CO_2 absorption, diffusive layer overlap, the advection conductance contribution, and removing the immobile layer all in the 2pK-model. From this study we find that the absorbed CO_2 and the Stern capacitance C_s are the most important model features when calculating the conductance.

4.3.1 Identifying the Relevant Fitting Parameters

We have been supplied with experimental data for the conductance of different silica nanochannels containing KCl solutions which can be found in Appendix B.5. In order to fit our conductance curve to these data we carry out a preliminary investigation of how the different parameters in the 2pK-model affect the shape and position of the curve. Assuming the channel dimensions together with the actual concentrations of particles in the bulk to be known quantities we are left with the following surface related input parameters to fit in our model confer Table 3.2: the Stern capacitance C_s, the total number of chargeable sites Γ_{tot}, pK_+, and pK_-.

Stern Capacitance C_s

First, the Stern capacitance C_s is varied. The conductance versus KCl bulk concentration for different values of the Stern capacitance is shown in Fig. 4.6. Recall that the literature value of the Stern capacitance is $C_s = 0.2\ \mathrm{F\,m^{-2}}$, and it is seen that increasing the Stern capacitance generally elevates the conductance for concentrations below the beginning of the departure regime. For increasing Stern capacitances the beginning of the departure regime itself shifts toward higher concentrations. We can explain this general increase from the capacitor relation Eq. (3.21). When C_s increases the difference between ϕ_o and ϕ_d decreases if δ_o is assumed constant. The elevated conductance can be explained by an increase in the size of ϕ_d towards ϕ_o. The largest possible value of ϕ_d is obtained with $C_s = \infty$ where $\phi_d = \phi_o$ corresponding to removing the immobile layer. This marks

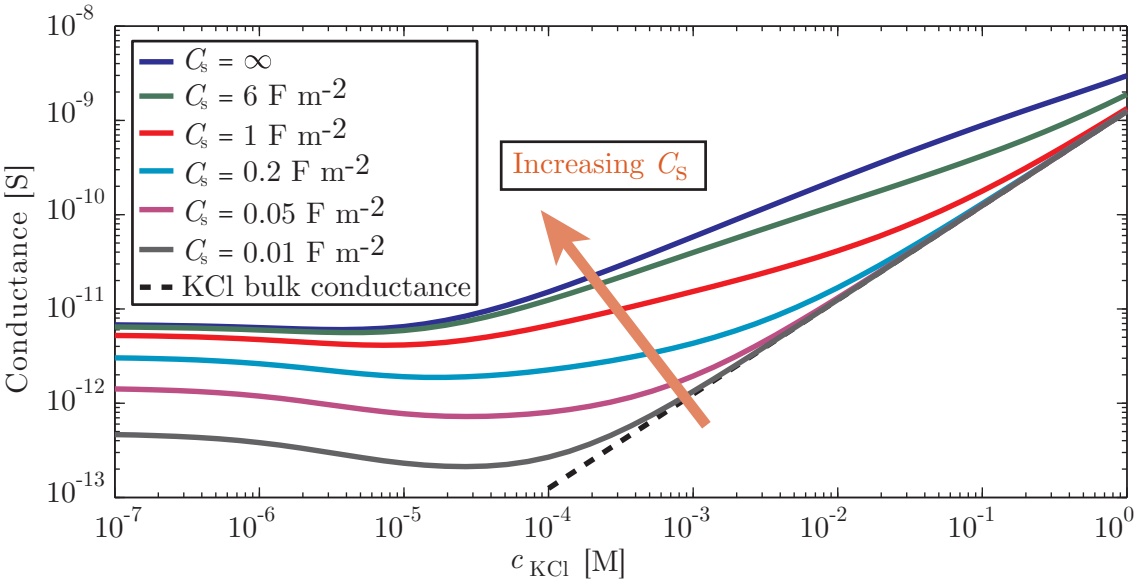

Figure 4.6: A log-log plot of the channel conductance versus KCl bulk concentration for different Stern capacitances C_s together with the bulk conductance of KCl. The orange arrow with text box indicates the displacement of the conductance curve when increasing the Stern capacitance. The mobilities and model parameters can be seen in Table B.2 and Table B.3, respectively, in Appendix B. The channel has height $h = 200$ nm

an upper bound for how much the ϕ_d potential can elevate the conductance. The Stern capacitance has a large effect on the conductance so we will use it as a best fit parameter.

Total Number of Chargeable Sites Γ_{tot}

We now vary the total number of chargeable sites Γ_{tot} around the literature value of 5 sites nm^{-2} [16]. The conductance versus KCl bulk concentration for different values of Γ_{tot} is shown in Fig. 4.7. By increasing Γ_{tot} the conductance curve is generally elevated from the beginning of the departure regime. This is because a general upscaling of the total number of chargeable sites increases the number of all site states SiOH, SiO^-, and $SiOH_2^+$ which increases the size of the surface charge density, see Eq. (3.19). This attracts more screening counterions to the surface including hydrons. Therefore, the hydron concentration at the o-plane $c_H^b \exp\left(-\frac{e}{k_B T}\phi_o\right)$ increases in the equilibrium relations for the surface reactions Eq. (3.18). This induces shifts in the equilibria resulting in a reduction of the ratios $\theta_{SiO^-}/\theta_{SiOH}$ and $\theta_{SiOH}/\theta_{SiOH_2^+}$. In other words, more neutral SiOH sites are created relative to negative SiO^- sites and more positive $SiOH_2^+$ sites are created relative to neutral SiOH sites. Therefore, the increase in size of δ_o is opposed on the negative silica surface which opposes the increase in conductance. This opposing effect explains why the distance between successive conductance curves on the log scale in Fig. 4.7 decreases for increasing Γ_{tot}. As a numerical example consider the conductances at a concentration

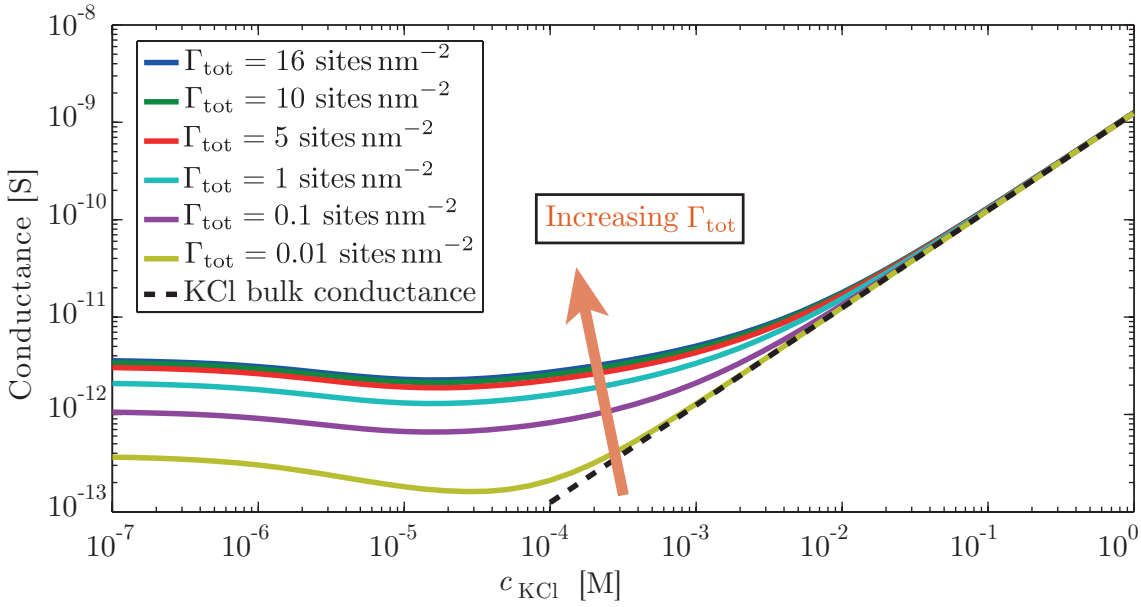

Figure 4.7: A log-log plot of the channel conductance versus KCl bulk concentration for different values of the total number of chargeable sites Γ_{tot} together with the bulk conductance of KCl. The orange arrow with text box indicates the displacement of the conductance curve when the total number of chargeable sites increases. The mobilities and model parameters can be seen in Table B.2 and Table B.3, respectively, in Appendix B. The channel has height $h = 200$ nm.

of 10^{-7} M. The distance between the conductance curves for $\Gamma_{tot} = 0.01$ sites nm^{-2} and $\Gamma_{tot} = 0.1$ sites nm^{-2} is 2.89 whereas the distance between the conductance curves for $\Gamma_{tot} = 1$ sites nm^{-2} and $\Gamma_{tot} = 10$ sites nm^{-2} is 1.62. Γ_{tot} is typically used in the literature as either 5 sites nm^{-2} or 8 sites nm^{-2} [23] and since we see from Fig. 4.7 that the conductance curve largely remains constant when varying Γ_{tot} around these values we will not use it as a fitting parameter for the conductance curve.

pK_+: The Number of $SiOH_2^+$ Sites

A plot of the conductance versus KCl bulk concentration for different values of pK_+ is shown in Fig. 4.8. The point of zero charge is the average of pK_+ and pK_-, Eq. (3.47). When decreasing pK_+ more neutral SiOH sites are created relative to positively charged $SiOH_2^+$ sites confer Eq. (3.54) which increases the size of the surface charge density δ_o on the negative silica surface. When the size of δ_o increases more counterions are needed for screening increasing the elevated concentrations and thereby increasing the conductance. Qualitatively, as seen in the figure, the valley and plateau level increases slightly when reducing the pK_+ with the rest of the curve remaining unchanged. The small effect on the conductance is explained by $\theta_{SiOH_2^+}$ being orders of magnitude lower than θ_{SiO^-} and θ_{SiOH} at pH = 5.68 similar to our analysis using the metal adsorption model in Fig. 3.5. We will

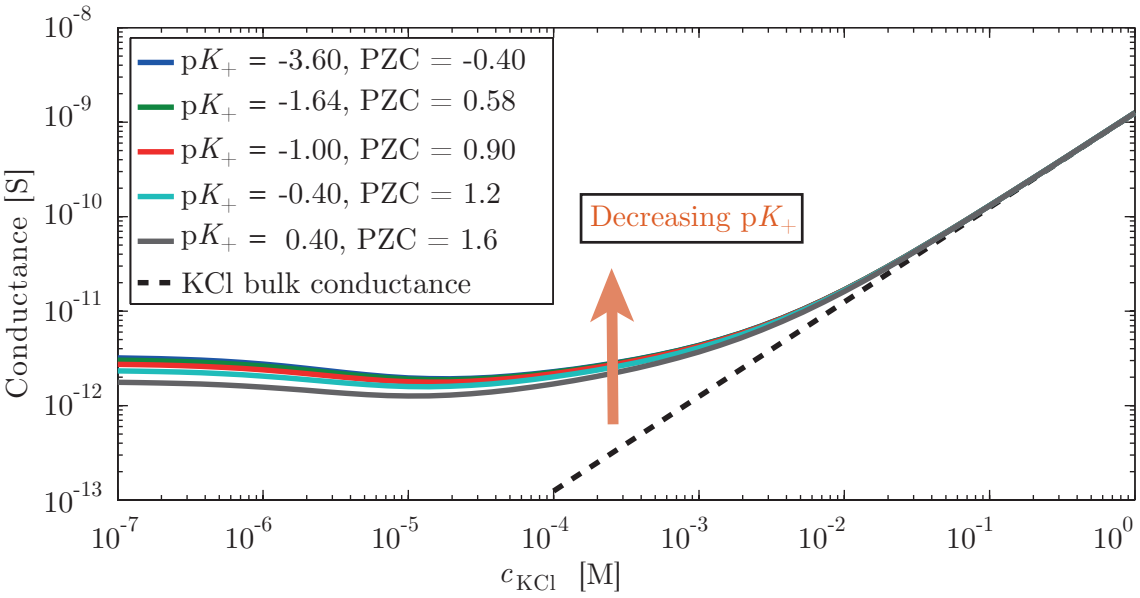

Figure 4.8: A log-log plot of the channel conductance versus KCl bulk concentration for different values of pK_+ together with the bulk conductance of KCl. The point of zero charge is calculated from Eq. (3.47). The orange arrow with text box indicates the displacement of the conductance curve when decreasing pK_+. The mobilities and model parameters can be seen in Table B.2 and Table B.3, respectively, in Appendix B. The channel has height $h = 200$ nm.

therefore not use pK_+ as a relevant fitting parameter for the conductance measurements.

pK_-: The Number of SiO^- Sites

The conductance is plotted versus KCl bulk concentration for different values of pK_- in Fig. 4.9. The conductance below the bulk regime is seen to increase for a decreasing pK_-. Lowering pK_- increases the ratio $\theta_{\mathrm{SiO^-}}/\theta_{\mathrm{SiOH}}$ according to Eq. (3.53). Therefore, more SiO^- sites are created relative to SiOH sites and the size of the surface charge density δ_{o} increases on the negative silica surface. The conductance increases below the bulk regime because more counterions are needed for screening increasing the elevated concentrations. We will use pK_- as a best fit parameter.

In summary, the most relevant fitting parameters are the Stern capacitance C_{s} and the logarithmic dissociation constant governing the deprotonization of the silica surface pK_-.

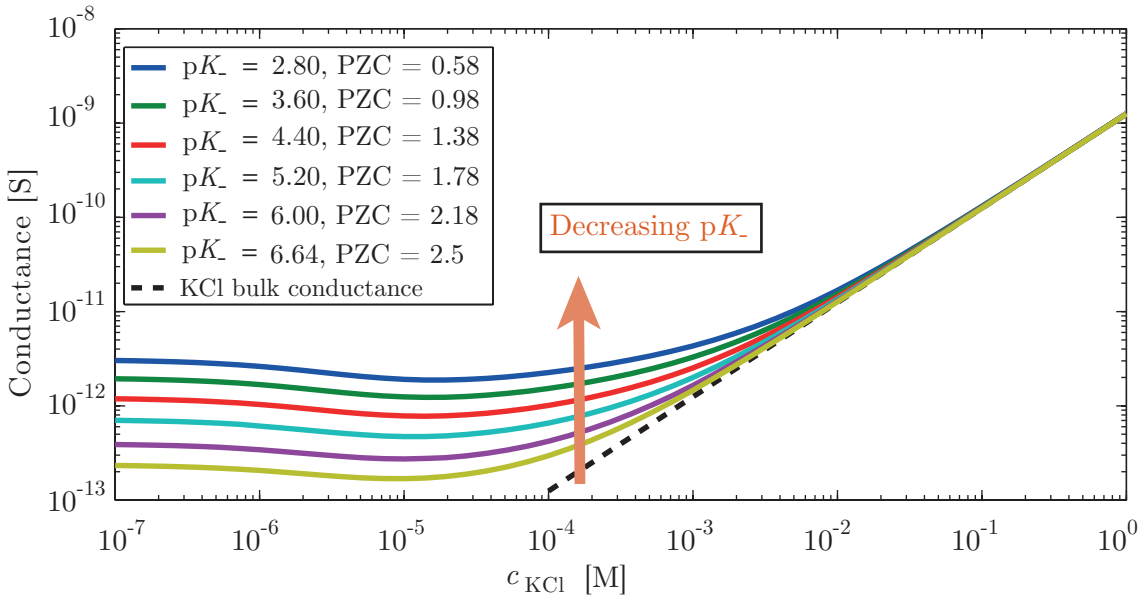

Figure 4.9: A log-log plot of the channel conductance versus KCl bulk concentration for different values of pK_- together with the bulk conductance of KCl. The point of zero charge is calculated from Eq. (3.47). The orange arrow with text box indicates the displacement of the conductance curve when decreasing pK_-. The mobilities and model parameters can be seen in Table B.2 and Table B.3, respectively, in Appendix B. The channel has height $h = 200$ nm.

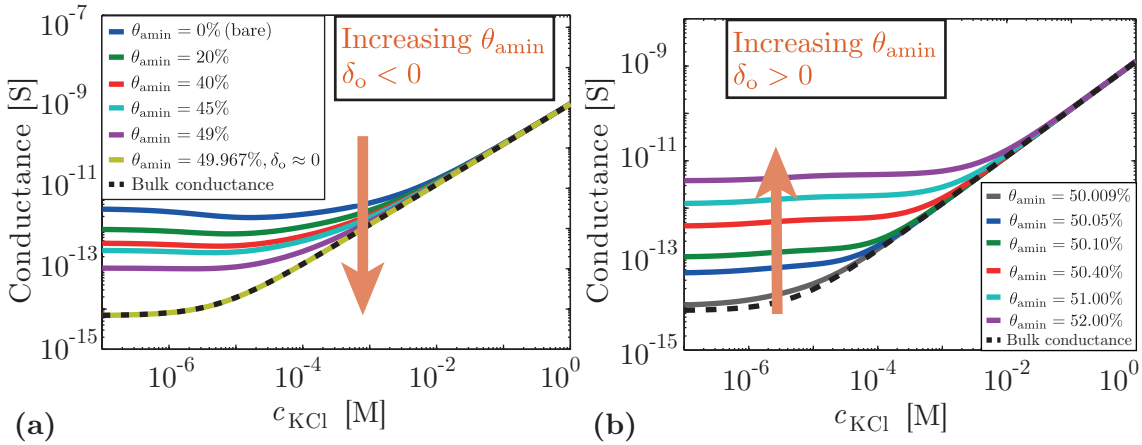

Figure 4.10: A log-log plot of the channel conductance versus KCl bulk concentration for different aminosilane coverages θ_{amin} together with the bulk conductance (dashed black curve) Eq. (4.14). In **(a)** the silica surface is net negative $\delta_o < 0$ and in **(b)** it is net positive $\delta_o > 0$. The orange arrows with text boxes indicate the conductance curve displacement when the coverage is increased. The mobilities and model parameters can be seen in Table B.2 and Table B.3, respectively, in Appendix B. The channel height is 200 nm.

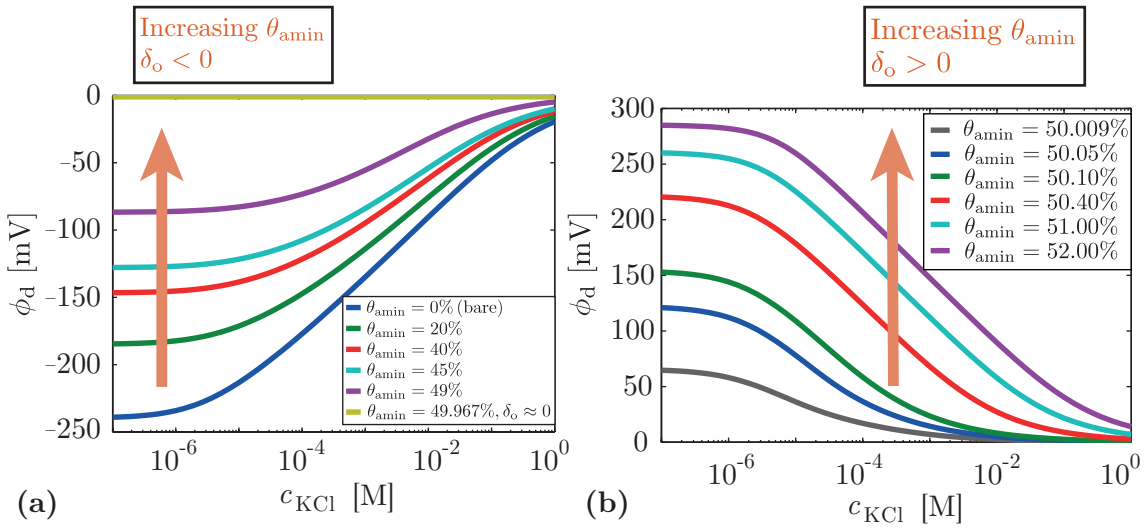

Figure 4.11: A lin-log plot of the ϕ_d potential versus KCl bulk concentration for different aminosilane coverages. In **(a)** the silica surface is net negative $\delta_o < 0$ and in **(b)** it is net positive $\delta_o > 0$. The orange arrows with text boxes indicate the conductance curve displacement when the coverage is increased. The mobilities and model parameters can be seen in Table B.2 and Table B.3, respectively, in Appendix B. The channel height is 200 nm.

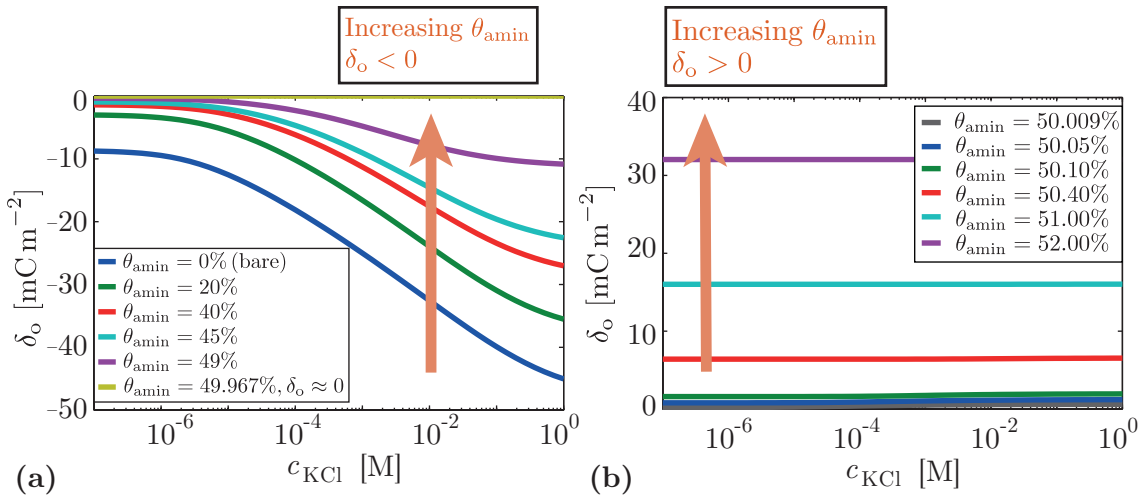

Figure 4.12: A lin-log plot of the surface charge density δ_o versus KCl bulk concentration for different aminosilane coverages. The mobilities and model parameters can be seen in Table B.2 and Table B.3, respectively, in Appendix B. The channel height is 200 nm.

4.3.2 Conductance Dependence on Aminosilane Coating

In Section 3.5 we derived the modified equations for the 2pK-model taking into account coating on the silica surface. We now study how the conductance curve depends on different coating coverages of aminosilane θ_{amin}. The conductance is plotted versus KCl bulk concentration for different values of θ_{amin} in Fig. 4.10. In Fig. 4.11 and Fig. 4.12 corresponding ϕ_{d} potentials and surface charge densities δ_{o} are plotted, respectively. In Fig. 4.10(a) it is seen that the conductance decreases below the bulk regime for increasing coating coverages until the surface becomes neutral i.e. $\delta_{\text{o}} = 0$ at $\theta_{\text{amin}} \approx 49.967\%$. For neutral walls the concentration of each ion equal its bulk value throughout the channel so the conductance follows the bulk conductance curve Eq. (4.14). Furthermore, the ϕ_{d} potential is expected to be zero which is confirmed by the yellow curve in Fig. 4.11(a). Fig. 4.11(a) shows that the size of ϕ_{d} increases with decreasing KCl bulk concentration, and Fig. 4.12(a) that the size of δ_{o} decreases with decreasing KCl bulk concentration. This is in agreement with our discussion in Section 4.2.1 where we argued that ζ became more negative when the size of δ_{o} decreased. We note that an increased positive coverage increases both the ϕ_{d} potential Fig. 4.11 and the surface charge density δ_{o} Fig. 4.12.

When the surface is neutral

$$\theta_{\text{SiO}^-} = \theta_{\text{SiOH}_2^+} + \theta_{\text{amin}} \quad \text{(neutral surface)}, \tag{4.19}$$

and since $\theta_{\text{SiOH}_2^+}$ is many orders of magnitude lower than θ_{amin} we have that $\theta_{\text{SiO}^-} \approx 49.967\%$ confer Fig. A.12 in Appendix A.11. Furthermore, since θ_{SiOH} is also many orders of magnitude lower than θ_{SiO^-} the neutral surface is dominated by the coating coverage and negatively charged SiO^- sites. When θ_{amin} is increased above 49.967% the silica surface becomes positively charged verified by Fig. 4.12(b). In the following discussion we will refer to $\theta_{\text{amin}} < 49.967\%$ as the low coverage regime (negative silica surface) and $\theta_{\text{amin}} > 49.967\%$ as the high coverage regime (positive silica surface).

In Section 4.2.1 we argued that when the bulk salt concentration is reduced screening of the wall becomes harder. The charged surface counteracted this by becoming less charged resulting in easier screening. However, in the high coverage regime the surface only has a fixed amount of coated sites and SiO^- sites and is unable to create more negative sites to reduce its charge. Therefore, δ_{o} becomes independent of the KCl bulk concentration, see Fig. 4.12(b). It follows that the ϕ_{d} potential must increase even more to attract counterions to sustain screening of the wall. δ_{o} increases rapidly with coating coverage in the high coverage regime see Fig. 4.12(b). Moreover, since it is constant throughout the concentration range more counterions are present in the diffusive layers even for the lowest concentrations as compared to Fig. 4.12(a). This results in the conductance increasing rapidly with the aminosilane coating coverage below the bulk regime, see Fig. 4.10. Finally, we note that when the wall becomes positive the counterions change from potassium (K^+) and hydrons (H^+) to chloride (Cl^-), hydroxide (OH^-), carbonate (CO_3^{2-}), and bicarbonate (HCO_3^-).

4.4 Chapter Summary

In this chapter we derived the conductance for a rectangular nanochannel, see Eqs. (4.4), (4.6), and (4.11), and calculated it numerically using the 2pK-model, see Fig. 4.2. We characterized the conductance curve by four regimes: the bulk regime, departure, valley, and plateau defined in Fig. 4.3(f). We then explained the conductance curve by using the concentration profiles in Fig. 4.3(a)–(e). We introduced a box model of the concentration profiles Fig. 4.4 and found that the increasing ζ potential is the main reason for the conductance curve deviation from the bulk conductance as compared to the effect of the increasing Debye length λ_{D}. We further estimated the contribution to the conductance from the elevated counterion concentration and the bulk concentration in the end of Section 4.2.1. We found that at high KCl bulk concentrations the elevated counterion concentrations had negligible effect on the conductance as compared to the bulk concentrations whereas for low KCl bulk concentrations the elevated counterion concentrations dominated the conductance over the bulk concentrations. We carried out an investigation of which surface related parameters in the 2pK-model had a main influence on the shape of the conductance curve with respect to being used as fitting parameters and found that the Stern capacitance C_{s} and logarithmic dissociation constant governing the negative sites pK_{-} are most suited, see Section 4.3. Finally, we studied how aminosilane coating of the silica surface changed the conductance curve.

Chapter 5

Characterization of the Silica Nanochannel Surface by Conductance Measurements

In this chapter we start out by describing how the conductance of a nanochannel is measured experimentally. We present conductance data of nanochannels measured in the UCSB Nanolab and fit our 2pK-model to the data using the fitting parameters found in Section 4.3.1. Our goal is to characterize the nanochannel surface in terms of these parameters. Finally, we discuss our results.

5.1 Nanochannel Conductance Experiments at the UCSB Nanolab

To experimentally measure the conductance Eq. (4.4)

$$S \equiv \frac{I}{\Delta V} \tag{5.1}$$

of nanochannels a voltage ΔV can be applied over two electrodes in each end of the channel and the current I can be recorded. The system setup accomplishing this is shown in Fig. 5.1. When fabricating the nanochannels used in experiments the length and width are first defined by a photolithographic process [21]. Then, a directional plasma etches the height of the channel through the amorphous silica. The final height is controlled by the etching time and the experiments are carried out for nanochannels with heights of 165 nm and 200 nm. The electrolyte is potassium chloride (KCl) dissolved in deionized water at different concentrations. Besides measuring the conductance in the regimes where it deviates from its bulk value we are also interested in measuring the bulk regime conductance so concentrations up to 100 mM are used. In this way we can verify the channel dimensions used as input parameters in the 2pK-model.

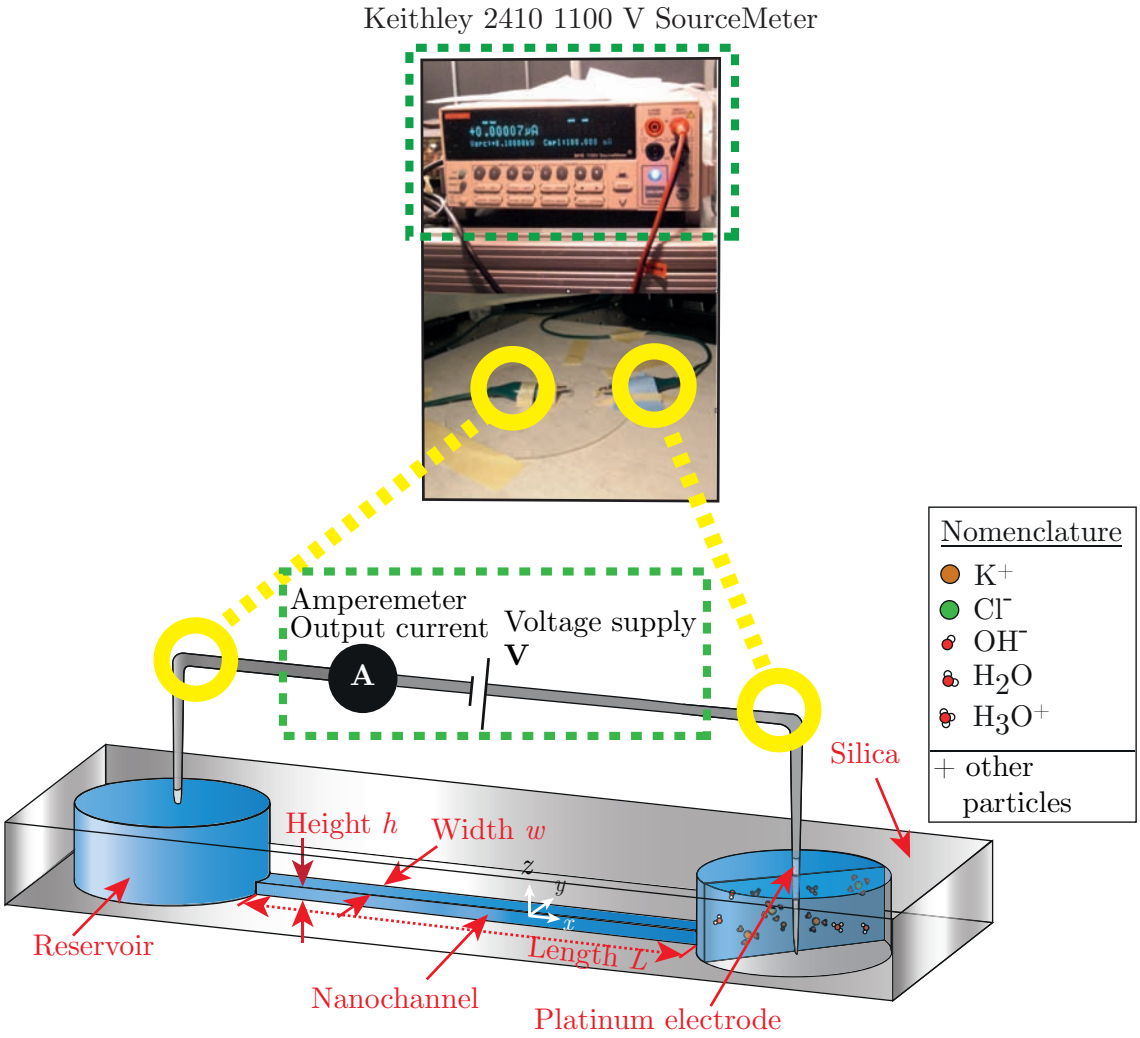

Figure 5.1: Experimental setup for measuring the conductance of a silica nanochannel. Top: a real photo of the setup. Bottom: a sketch of the same system defining the geometry of the nanochannel and elements in the setup. A nomenclature is provided in the right of the figure. The yellow circles show the electrodes just before entering the electrolyte. The green dashed box indicates the voltage supply and amperemeter both part of a Keithley 2410 1100 V SourceMeter used in the experiments. The reservoirs are shown connected through the nanochannel which serves as a channel for electric current when a voltage is applied over the two electrodes. The right reservoir is shown in a cross-section with enlarged electrolyte particles. Data from the current meter (black full circle) and the voltage source allows the calculation of conductance S through the channel. The channel has dimensions $h \times w \times L = 200$ nm $\times$ 5 µm $\times$ 1.2 cm.

5.1.1 Procedure

Before each current measurement the channel is rinsed with deionized water for 30 minutes. The channel is then rinsed with the KCl solution until reaching a stabile current readout. The voltage is sourced 100 to 500 V in steps of 100 V. The stabilized current is recorded averaged over 300 samples for each voltage. The result is thus an average conductance calculated over 5 voltage steps. This procedure is repeated for all concentrations.

5.1.2 Data

We will fit our model to two sets of data from each of two experimentalists: David A. Herrick and Andrew Crumrine both having followed the procedure stated above. The completion of one such procedure will be dubbed one trial. David A. Herrick has one trial for each concentration whereas Andrew Crumrine has multiple trials per concentration.

Dataset 1 and 2 from David A. Herrick can be seen in Table B.5 and Table B.6, respectively, in Appendix B.5. Dataset 1 and 2 from Andrew Crumrine can be seen in Table B.7 and Table B.8-B.9, respectively, in Appendix B.5.

5.2 Fitting the Conductance Data for Bare Silica Nanochannels

When fitting the 2pK-model to the experimental conductance data we use the same procedure to calculate the conductance as in Section 4.2. We use the built-in MatLab function `lsqcurvefit` around our model to fit the data in two different fitting approaches. In fitting approach 1 (fit 1) we only fit pK_- and set $C_\mathrm{s} = 0.2$. In fitting approach 2 (fit 2) we fit both pK_- and C_s. All other model parameters are found in Table B.2 and Table B.3 in Appendix B. The script used for fitting the conductance data can be found in Appendix C.8

For each data set the fitting statistics are provided in corresponding tables containing the coefficient of determination R^2 and the 2-norm of the residual given by

$$\sum_{i=1}^{\mathcal{P}} \left(S_{\mathrm{data},i} - S_{\mathrm{fit},i}\right)^2, \tag{5.2}$$

where $\mathcal{P}$, $S_{\mathrm{data},i}$, and $S_{\mathrm{fit},i}$ are the number of experimental data points, the experimentally measured conductance at point i, and the calculated conductance from the fitted model at point i, respectively. The last column in each table contains the absolute relative difference between the fitted pK_- value and the literature value p$K_- = 6.64$ [16], which we will refer to as the deviation.

5.2.1 Data Sets from David A. Herrick

For the data sets of David A. Herrick the channel dimensions are $h \times w \times L = 200$ nm $\times$ 5 µm $\times$ 1.2 cm.

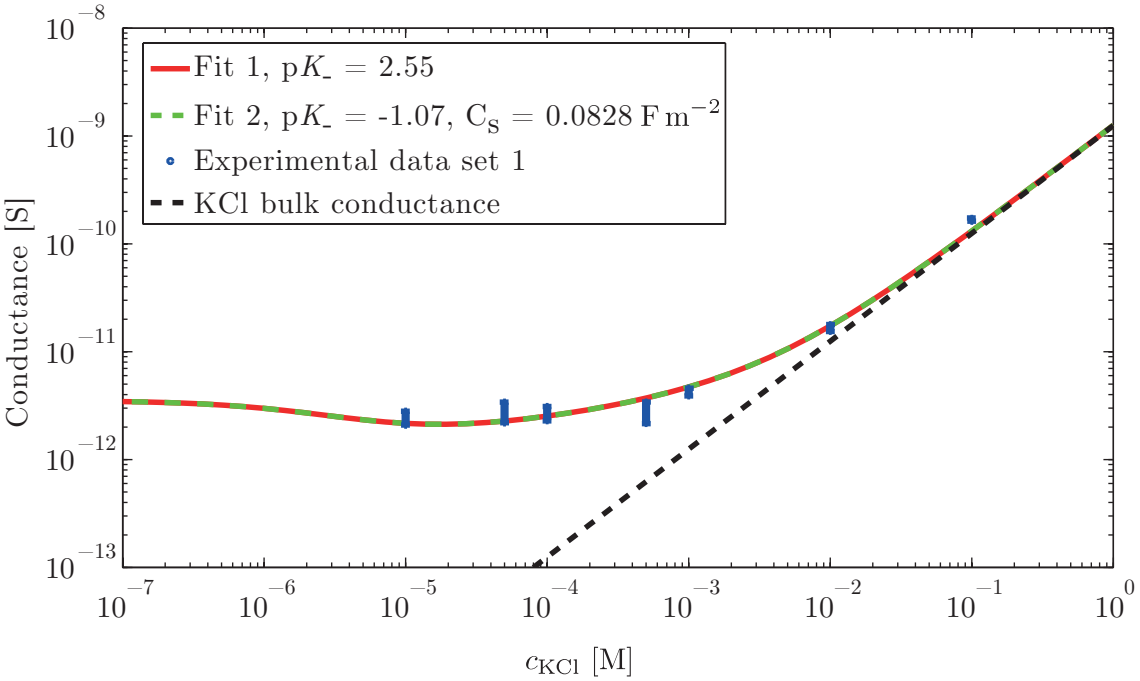

Figure 5.2: Fit to conductance data set 1 from David A. Herrick. A log-log plot of conductance versus KCl bulk concentration. Fitting approach 1 (Fit 1, red) and fitting approach 2 (Fit 2, dashed green) are plotted with experimental data (blue) and bulk KCl conductance (dashed black).

Data Set 1

The experimental data are found in Table B.5 in Appendix B.5. Our best fit to the model is seen for both fitting approaches in Fig. 5.2. The fitting statistics are found in Table 5.1.

David A. Herrick - data set 1 - UCSB Nanolab				
Fitting Approach	Fitting Parameter	R^2	2-Norm of Residual	Deviation
Fit 1	$pK_- = 2.55$	0.941	0.320	62%
Fit 2	$pK_- = -1.07$	0.801	0.246	116%
	$C_s = 0.0828$ F m^{-2}			

Table 5.1: Fitting results from experimental data set 1 from David A. Herrick. Coefficient of determination R^2 is in the third column. Absolute relative difference between the found pK_- value and the literature value of 6.64 in the rightmost column.

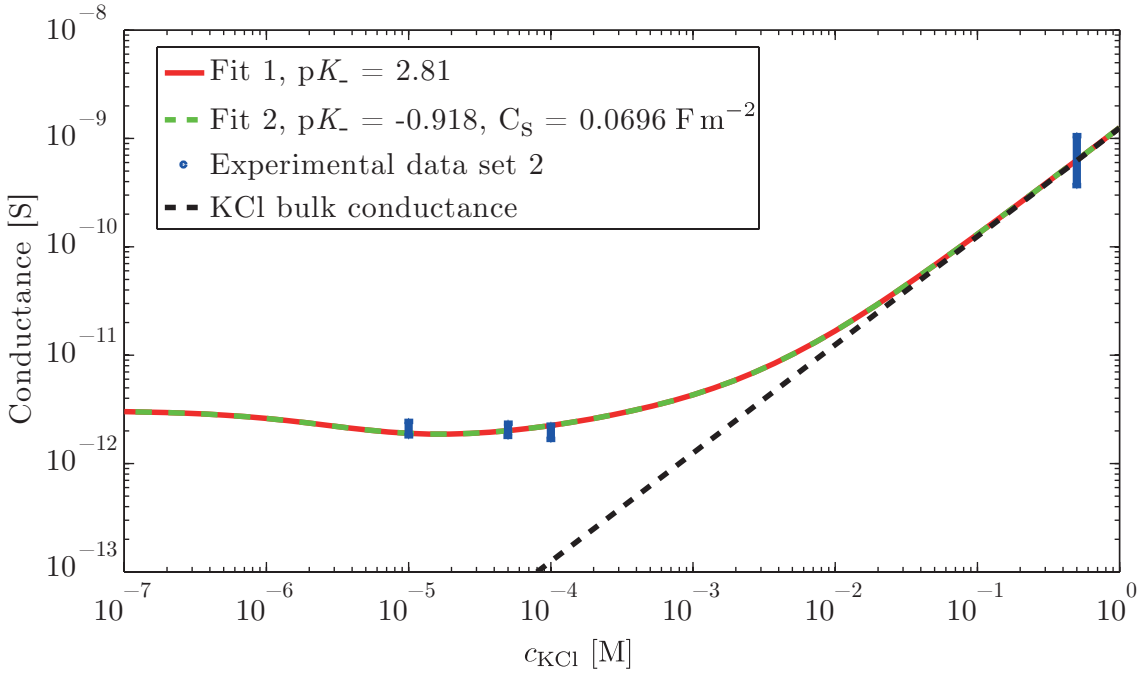

Figure 5.3: Fit to conductance data set 2 from David A. Herrick. A log-log plot of conductance versus KCl bulk concentration. Fitting approach 1 (Fit 1, red) and fitting approach 2 (Fit 2, dashed green) are plotted with experimental data (blue) and bulk KCl conductance (dashed black).

Data Set 2

The experimental data are found in Table B.6 in Appendix B.5. Our best fit to the model is seen for both fitting approaches in Fig. 5.3. The fitting statistics are found in Table 5.2.

David A. Herrick - data set 2 - UCSB Nanolab				
Fitting Approach	Fitting Parameter	R^2	2-Norm of Residual	Deviation
Fit 1	$pK_- = 2.81$	0.802	0.218	58%
Fit 2	$pK_- = -0.918$	0.801	0.198	114%
	$C_s = 0.0696$ F m^{-2}			

Table 5.2: Fitting results from experimental data set 2 from David A. Herrick. Coefficient of determination R^2 is in the third column. Absolute relative difference between the found pK_- value and the literature value of 6.64 in the rightmost column.

5.2.2 Data Sets from Andrew Crumrine

Preliminary investigation of the data sets from Andrew Crumrine showed measured conductances around a factor of 1.5 higher than predicted from theory in the bulk regime. The Kohlrausch law cannot explain this since it predicts lower conductances for high concentrations, see Appendix A.8. Therefore, we suggested that the channel dimensions stated in the first place could be off due to fabrication errors or wear. The channel dimensions were measured[1] using CVD imaging and the width was found to be 8 µm up to 2 µm less because a 4×4 binning was used. This confirmed that at least the width of the channel did not fit the initially given value of 5 µm and that it could explain the discrepancy factor of 1.5. Therefore, we chose two bulk conductance measurements from data set 2 from Andrew Crumrine and fitted the channel width to it. By hindsight we choose 50 mM and 100 mM to be the bulk points. Using the width as fitting parameter we get that the channel should be 7.09 µm wide for the bulk data points to best fit experiments in the bulk regime. The fitting results are summarized in Table 5.3.

Fitting Channel Width		
Fitting Parameter	R^2	2-Norm of Residual
$w = 7.09 \times 10^{-6}$ m	0.990	0.00312

Table 5.3: Fitting channel width to the bulk data points from data set 2 from Andrew Crumrine. Coefficient of determination R^2 is in the second column.

[1] The measurements were carried out by Mariateresa Napoli at the UCSB Nanolab (May 2010).

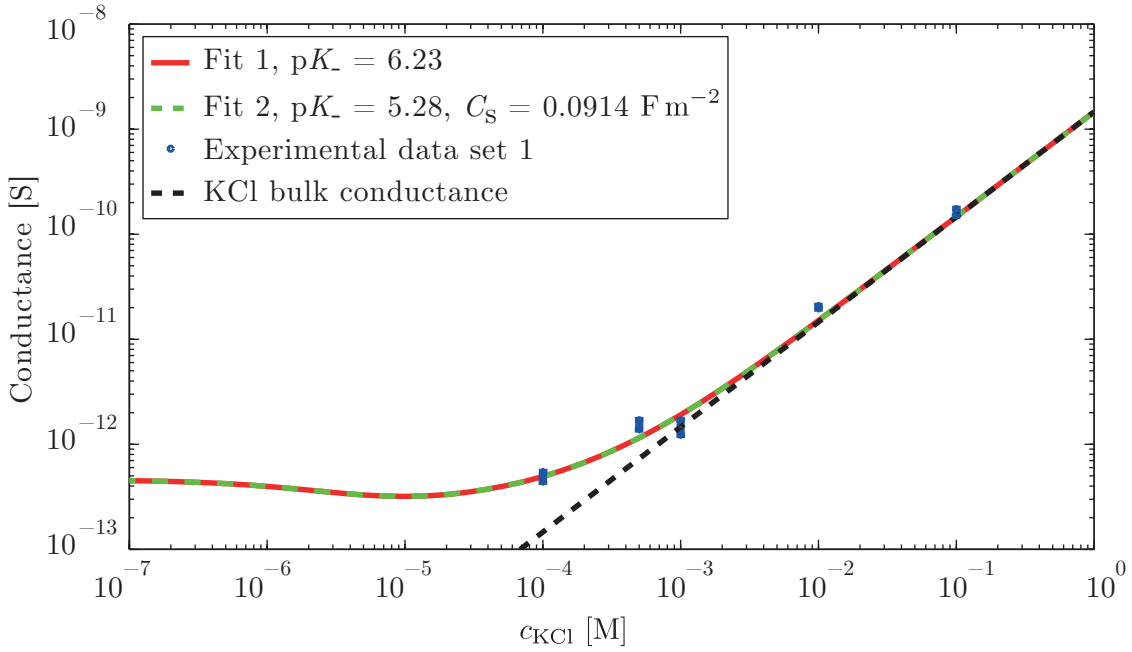

Figure 5.4: Fit to conductance data set 1 from Andrew Crumrine. A log-log plot of conductance versus KCl bulk concentration. Fitting approach 1 (Fit 1, red) and fitting approach 2 (Fit 2, dashed green) are plotted with experimental data (blue) and bulk KCl conductance (dashed black).

Data Set 1

The experimental data are found in Table B.7 in Appendix B.5. Our best fit to the model is seen for both fitting approaches in Fig. 5.4. The fitting statistics are found in Table 5.4.

Andrew Crumrine - data set 1 - UCSB Nanolab				
Fitting Approach	Fitting Parameter	R^2	2-Norm of Residual	Deviation
Fit 1	pK_- = 6.23	0.985	0.195	6%
Fit 2	pK_- = 5.82	0.984	0.194	20%
	C_s = 0.0914 F m^{-2}			

Table 5.4: Fitting results from experimental data set 1 from Andrew Crumrine. Coefficient of determination R^2 is in the third column. Absolute relative difference between the found pK_- value and the literature value of 6.64 in the rightmost column.

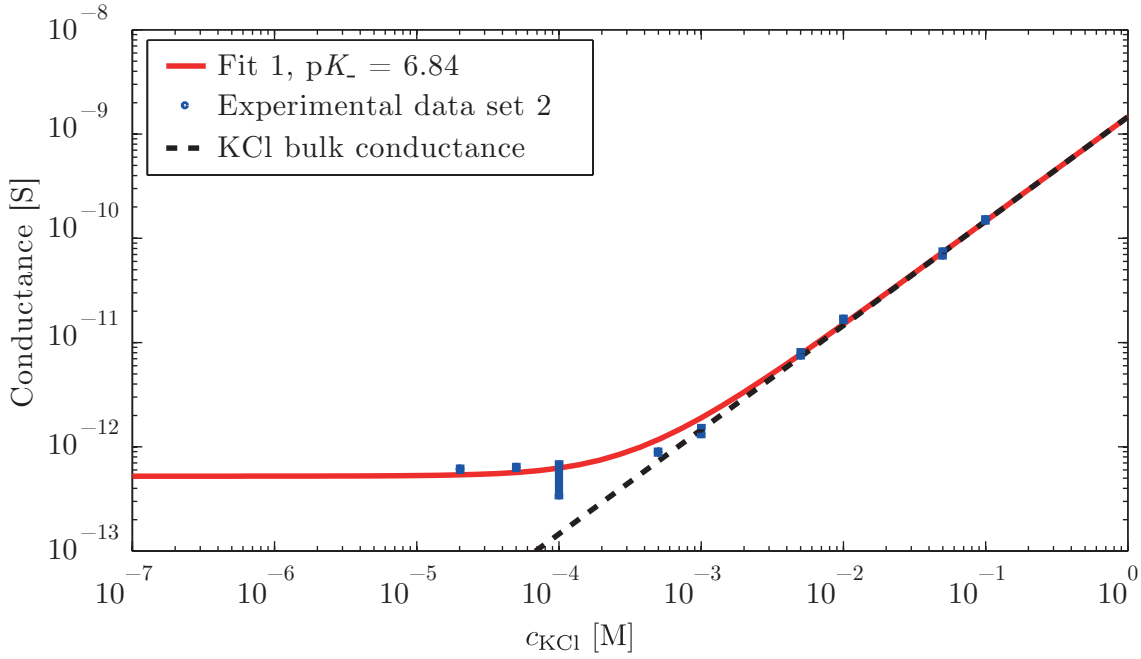

Figure 5.5: Fit to conductance data set 2 from Andrew Crumrine. A log-log plot of conductance versus KCl bulk concentration. Fitting approach 1 (Fit 1, red) is plotted with experimental data (blue) and bulk KCl conductance (dashed black).

Data Set 2

When fitting to data set 2 we add 0.1 mM HCl in the model. For this data set we were unable to use the second fitting approach due to numerical problems and the timeframe of the project. The experimental data are found in Table B.8 in Appendix B.5. Our best fit to the model is seen for both fitting approaches in Fig. 5.5. The fitting statistics are found in Table 5.5.

Andrew Crumrine - data set 2 - UCSB Nanolab				
Fitting Approach	Fitting Parameter	R^2	2-Norm of Residual	Deviation
Fit 1	pK_- = 6.84	0.998	0.256	3%

Table 5.5: Fitting results from experimental data set 2 from Andrew Crumrine. Coefficient of determination R^2 is in the third column. Absolute relative difference between the found pK_- value and the literature value of 6.64 in the rightmost column.

5.3 Fitting the Conductance Data for Coated Silica Nanochannels

One application of our models is to determine the percentage coverage of silica nanochannels flushed with a coating solution. This can be done by finding the pK_- value for a bare channel from conductance measurements. Then, we can assume that pK_- stays independent of the surface coating and fit the coverage of coated molecules θ_{coat} to get the percentage coverage. To our best knowledge this has not been done in the literature before and in collaboration with UCSB Nanolab we are planning to publish a paper presenting our models and results from characterizing bare and coated silica nanochannel surfaces by conductance measurements.

5.4 Discussion of Results

When fitting our model to the experimental data we generally saw that fitting pK_- together with a concentration independent Stern capacitance (fit 2) generally led to a worse fit than when fitting pK_- alone (fit 1) with respect to the coefficient of determination and correlation with the literature value. Taking into account all fitting approaches we get that the fitted pK_- for the data sets from David A. Herrick deviates between 58 and 116 % from literature and that the data sets from Andrew Crumrine deviates between 3 and 20% from literature. Considering only fit 1 the data sets from David A. Herrick deviates between 58 and 62% from literature and the data sets from Andrew Crumrine deviates between 3 and 6 % from literature. Therefore, between the two fitting approaches considered here fit 1 is the most optimal. The higher R^2 values and lower deviations for Andrew Crumrine's data are also partly explained by the fact that we fitted the channel width to conductances in the bulk regime.

Both experimental data sets from David A. Herrick is generally one order of magnitude higher than what is calculated from the 2pK-model when using the literature value for pK_-. Before receiving the data sets from Andrew Crumrine, only fitting the data from David A. Herrick, we believed that the pK_- value valid for the metal adsorption model at high KCl concentrations was lower due to the very low KCl concentrations. However, this did not seem like a satisfactory explanation for the large discrepancy between the fitted value of pK_- and the literature value. Then, we fitted the model to the data sets from Andrew Crumrine which should be the same surface as the one in David A. Herrick's experiments and the model calculated a value of pK_- within 6% of the literature value for both data sets. Andrew Crumrine used a more precise amperemeter than David A. Herrick so the discrepancy can be due to the experimental measuring apparatus.

Assume now that the channel surface in David A. Herrick's experiments had a pK_- value near the literature value as expected. The discrepancy in the data sets from David A. Herrick can then be explained by asserting that his channel was coated with a positive coating molecule and was in the high coverage regime $\delta_o > 0$. We know from Section 4.3.2

that the conductance of a silica nanochannel which has been coated to become positively charged increases with increasing coating coverage see Fig. 4.10(b) on the order of magnitude needed to explain the discrepancy.

Turning now to data set 2 from Andrew Crumrine a conductance valley in Fig. 5.5 should be visible in the experimentally measured regime because 0.1 mM HCl has been added to the solution as discussed in Section 4.2.2. However, our preliminary investigation of how to move the valley shown in Fig. 4.5 was based on a pK_- value of 2.8 and a channel height of 200 nm which we had obtained from fitting our model to the data sets from David A. Herrick. Meanwhile, we have shown that a pK_- value near the literature value 6.64 fits the data sets from Andrew Crumrine and moreover his channel height is 165 nm. This does not mean that our proposal of moving the valley is wrong it was just not applicable for the channel used by Andrew Crumrine.

If the conductance calculated from the 2pK model fits in the bulk regime for a given channel we can primarily adjust the plateau level through pK_- but the detailed shape of the conductance curve between the bulk regime and the plateau level is model predictions. In Figs. (5.2)–(5.5) we see that the conductance curve correlates with data points over the entire concentration range. Our theoretical models are therefore able to predict conductance behavior due to the solid/liquid interface of different nanochannels and we can characterize the nanochannel surfaces through pK_-.

Chapter 6

Conclusion and Outlook

In the first part of the thesis we discussed how to calculate the actual concentrations of all solutes in an aqueous bulk solution which was needed before the electrolyte in the reservoirs enters the nanochannel. Using this method the absorption of CO_2 from the atmosphere was a straightforward task to include in the calculations.

When deriving the governing equations for the solid/liquid interface reactions we stated them in a general compact form increasing the stability in MatLab. We derived two models each valid in a particular concentration regime. The 2pK-model was only valid for low salt concentrations in the channel whereas the metal adsorption model was also valid for high salt concentrations. We expanded our models to account for coated silica surfaces which has not been done before.

We then moved on to calculate the conductance for low KCl bulk concentrations using the 2pK-model and we characterized its behavior. Our model predicted novel regimes not encountered in literature before. We defined the theoretically predicted regimes and dubbed them: the bulk regime, departure, valley, and plateau. We explained the origin of each regime from the transverse concentration profiles in the nanochannel elevated by the ζ potential. We found that for low KCl bulk concentrations in a bare silica nanochannel the elevation of the fixed bulk concentration of inherent hydrons dominated the conductance. Therefore, we stress that the hydrons cannot be neglected when modeling the conductance of a bare silica nanohannel for low salt concentrations. Since absorbed CO_2 changes the inherent hydron concentration it must be included in the model as well. This has not been considered in any surface/liquid interface model before to our best knowledge.

We studied how the conductance of a nanochannel depended on the aminosilane coating of the surface and found that if the charge density of the coated silica surface was negative an increased coating coverage lowered the conductance. Conversely, if the charge density of the coated silica surface was positive an increased coating coverages led to an increase in conductance.

Finally, we fitted our model to experimental data for a bare silica nanochannel and calculated a value of pK_- within 3% of the literature value. We found that fitting a concentration independent Stern capacitance together with the pK_- value did not lead to better correlation with experiments compared to fitting pK_- alone.

Our models provide a fundament for future work in characterizing silica/liquid interfaces. The next step is to provide experimental data for very low salt concentrations which could verify the theoretical prediction of the conductance valley and be a very important step in verifying this first theoretical proposal with respect to conductance measurements. Furthermore, current studies indicate that the Stern capacitance depends on the salt concentration. By experimentally determining the ζ potential for each measured concentration it could be made a given input parameter. Then it could be possible to determine if our models agree with a concentration dependent Stern capacitance. With the fitted pK_- value for a bare silica nanochannel we are now able to calculate conductances of a coated channel. This allows us to carry out a systematic study of the surface coverage obtained for a given coating solution concentration. From this, the model could predict whether the surface is net negative or positive for a given coating solution. It is possible to verify this theoretical prediction by an independent experiment where the direction of the electro-osmotic flow can determine the sign of the surface.

Finally, our theoretical work is an important step towards predicting the electrokinetic properties of silica nanochannels and thereby optimizing its use for example in biological engineering applications and in energy harvesting devices.

Appendix A

A.1 The Diffusive Layer for Multiple valences

In micro- and nanochannel experiments the sample electrolyte coexists with a buffer solution e.g. tris, borate, acetate or potassium phosphate, a flourescent, and/or a titrate solution. We therefore turn to the case where the electrolyte contacting the wall contains many different ions with multiple valences. A general expression for the Debye length where the fluid consists of $\mathcal{N}$ electrolyte pairs will be derived. Let the valence of the cation and anion of the ith electrolyte pair be $N_{+,i}$ and $N_{-,i}$, respectively, with both valences being positive integers treating the anion with an explicit sign as in Eq. (2.8).

A.1.1 Ionic Concentrations and Ion Pairs

A sketch of the system parameters discussed in this section can be seen in Fig. A.1. Turning to the ith electrolyte it consists of a certain concentration of cations and anions given by $c_{+,i}(\mathbf{r})$ and $c_{-,i}(\mathbf{r})$, respectively. If the wall is assumed neutral before any electrolyte contacts it far away from the wall the ζ potential cannot be felt by any ion, and the system has arranged itself in such a way that charge neutrality preserves here. The ith ion pair is overall neutral in the bulk and by denoting the bulk concentrations of the ith cation and anion $c^{\mathrm{b}}_{+,i}$ and $c^{\mathrm{b}}_{-,i}$, respectively, we have

$$c^{\mathrm{b}}_{+,i}N_{+,i} = c^{\mathrm{b}}_{-,i}N_{-,i}, \quad i \in \{1, ..., \mathcal{N}\}, \tag{A.1}$$

so the total charge density ρ_{el} satisfies

$$\rho_{\mathrm{el}}(\infty) = e\sum_{i=1}^{\mathcal{N}}\left[c^{\mathrm{b}}_{+,i}N_{+,i} - c^{\mathrm{b}}_{-,i}N_{-,i}\right] = 0. \tag{A.2}$$

Along with the charge neutrality it is useful to define a charge molarity c^{b}_{*} which is the number of charges of the same sign in a given volume in the bulk. Note that this definition is independent of how the charges are distributed. The charge molarity of the ions c^{b}_{*} is defined as

$$c^{\mathrm{b}}_{*} \equiv \sum_{i=1}^{\mathcal{N}} c^{\mathrm{b}}_{+,i}N_{+,i} = \sum_{i=1}^{\mathcal{N}} c^{\mathrm{b}}_{-,i}N_{-,i}. \tag{A.3}$$

The ionic strength $\mathcal{I}$ will be used later and is here given as

$$\mathcal{I} \equiv \frac{1}{2}\sum_{i=1}^{\mathcal{N}}\left[c^{\mathrm{b}}_{+,i}N^2_{+,i} + c^{\mathrm{b}}_{-,i}N^2_{-,i}\right]. \tag{A.4}$$

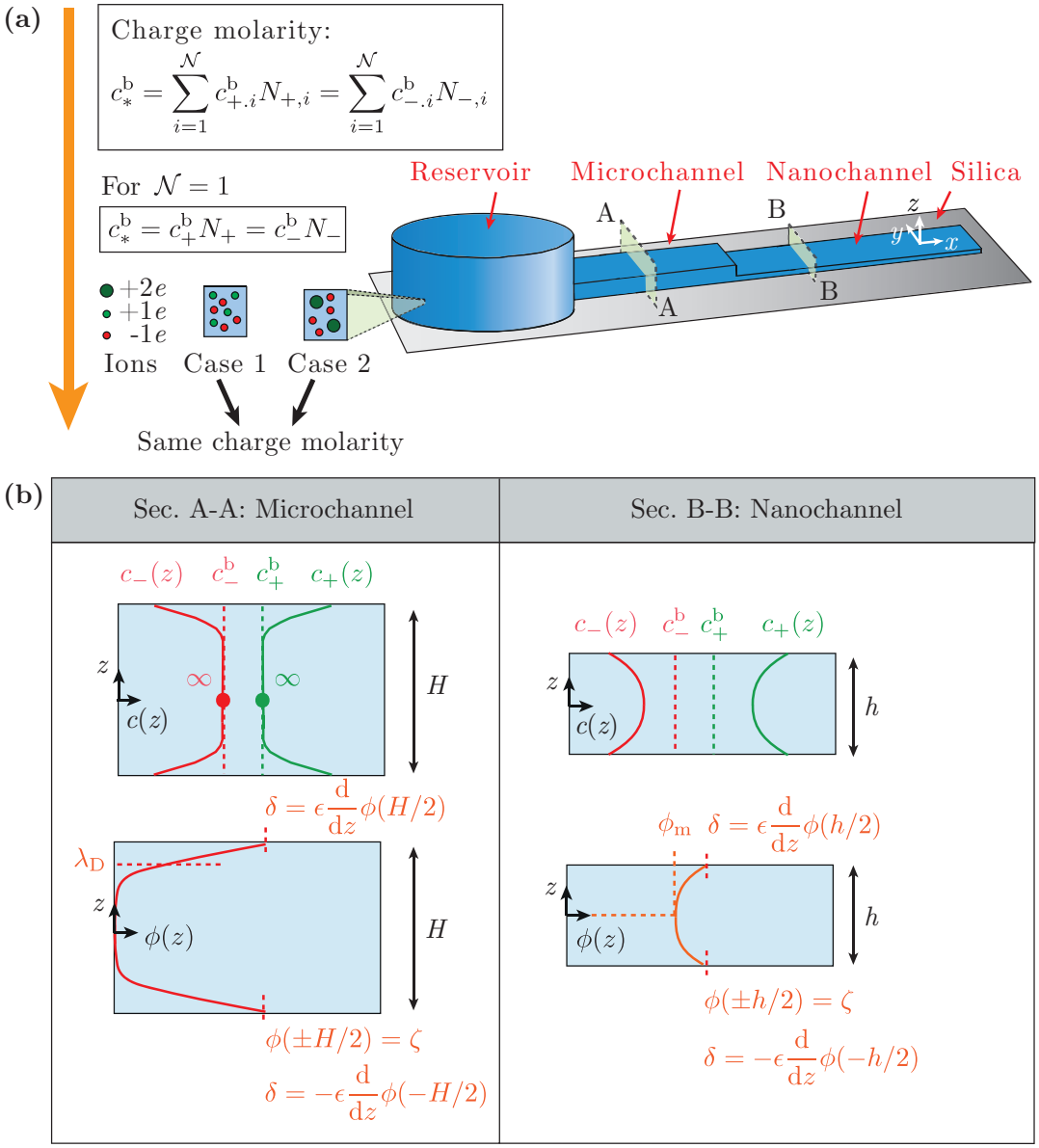

Figure A.1: **(a)** a sketch of a system showing a reservoir, microchannel, and nanochannel all placed on a silica substrate. In the left side of the figure the definition of charge molarity, discussed in Section A.1.1, has been exemplified. The xy-plane is defined in the far right of the figure and for each channel the origin of the third co-ordinate z, transverse to the flow direction, is taken to be symmetrically placed midways between the lower and upper bounding channel walls. Two cross-sections: sec. A-A and sec. B-B of the microchannel and nanochannel, respectively, have been highlighted. **(b)** shows the cross-section for the microchannel (left, sec. A-A) and the nanochannel (right, sec. B-B). For each channel a cross-section of typical concentration profiles (top) for co-ions (red) and counterions (green) have been shown together with the electric potential profile (bottom). The figure shows the parameters: $c_{\pm}(z), c_{\pm}^{\mathrm{b}}, \lambda_{\mathrm{D}}, \delta, \zeta$, and ϕ_{m}.

A.1.2 Debye Length for Constant Charge Molarity

We now derive an expression for the Debye length of a system containing only one type of cation and anion with valences N_+ and N_-, respectively. The ith ion concentration in the bulk, which will be useful later, can be expressed from Eq. (A.3) as

$$c^{\mathrm{b}}_{\pm,i} = \frac{1}{N_{\pm,i}} \left(c^{\mathrm{b}}_{*} - \sum_{j \neq i}^{\mathcal{N}} N_{\pm,j} c^{\mathrm{b}}_{\pm,j} \right). \tag{A.5}$$

An expression for the ith ion concentration as a function of the electric potential was derived in Eq. (2.11) for one electrolyte and is here stated on the form

$$c_{\pm,i}(\mathbf{r}) = c^{\mathrm{b}}_{\pm,i} \exp\left(\mp \frac{N_{\pm,i} e}{k_{\mathrm{B}} T} \phi(\mathbf{r}) \right). \tag{A.6}$$

The charge density $\rho_{\mathrm{el}}(\mathbf{r})$ can then be expressed as

$$\rho_{\mathrm{el}}(\mathbf{r}) = e \sum_{i=1}^{\mathcal{N}} \left[N_{+,i} c_{+,i}(\mathbf{r}) - N_{-,i} c_{-,i}(\mathbf{r}) \right]. \tag{A.7}$$

Inserting Eq. (A.7) into the Poisson equation Eq. (2.5) and using Eq. (A.6) leads to

$$\nabla^2 \phi(\mathbf{r}) = -\frac{e}{\epsilon} \sum_{i=1}^{\mathcal{N}} \left[N_{+,i} c^{\mathrm{b}}_{+,i} \exp\left(-\frac{N_{+,i} e}{k_{\mathrm{B}} T} \phi(\mathbf{r}) \right) - N_{-,i} c^{\mathrm{b}}_{-,i} \exp\left(\frac{N_{-,i} e}{k_{\mathrm{B}} T} \phi(\mathbf{r}) \right) \right], \tag{A.8}$$

which is the Poisson–Boltzmann equation for the multiple ion electrolyte. In the Debye–Hückel limit we have

$$\nabla^2 \phi(\mathbf{r}) = -\frac{e}{\epsilon} \sum_{i=1}^{\mathcal{N}} \left[N_{+,i} c^{\mathrm{b}}_{+,i} \left(1 - \frac{N_{+,i} e}{k_{\mathrm{B}} T} \phi(\mathbf{r}) \right) - N_{-,i} c^{\mathrm{b}}_{-,i} \left(1 + \frac{N_{-,i} e}{k_{\mathrm{B}} T} \phi(\mathbf{r}) \right) \right]. \tag{A.9}$$

Exploiting the charge neutrality in the bulk, Eq. (A.2), Eq. (A.9) simplifies to

$$\nabla^2 \phi(\mathbf{r}) = \frac{e^2}{\epsilon k_{\mathrm{B}} T} \sum_{i=1}^{\mathcal{N}} \left[c^{\mathrm{b}}_{+,i} N^2_{+,i} + c^{\mathrm{b}}_{-,i} N^2_{-,i} \right] \phi(\mathbf{r}) = \frac{1}{\{\lambda_{\mathrm{D}}(\mathcal{I})\}^2} \phi(\mathbf{r}), \tag{A.10}$$

where the Debye length in terms of the ionic strength Eq. (A.4) is

$$\lambda_{\mathrm{D}}(\mathcal{I}) = \sqrt{\frac{\epsilon k_{\mathrm{B}} T}{2e^2}} \sqrt{2} \left(\sum_{i=1}^{\mathcal{N}} \left[c^{\mathrm{b}}_{+,i} N^2_{+,i} + c^{\mathrm{b}}_{-,i} N^2_{-,i} \right] \right)^{-\frac{1}{2}} = \sqrt{\frac{\epsilon k_{\mathrm{B}} T}{2 \mathcal{I} e^2}}. \tag{A.11}$$

By using Eq. (A.5) the Debye length in Eq. (A.11) can be expressed in terms of the charge molarity as

$$\lambda_{\mathrm{D}} = \sqrt{2} \lambda^*_{\mathrm{D}} \left\{ \sum_{i=1}^{\mathcal{N}} \left[N_{+,i} \left(1 - \sum_{j \neq i} \frac{N_{+,j} c^{\mathrm{b}}_{+,j}}{c^{\mathrm{b}}_{*}} \right) + N_{-,i} \left(1 - \sum_{j \neq i} \frac{N_{-,j} c^{\mathrm{b}}_{-,j}}{c^{\mathrm{b}}_{*}} \right) \right] \right\}^{-\frac{1}{2}}, \tag{A.12}$$

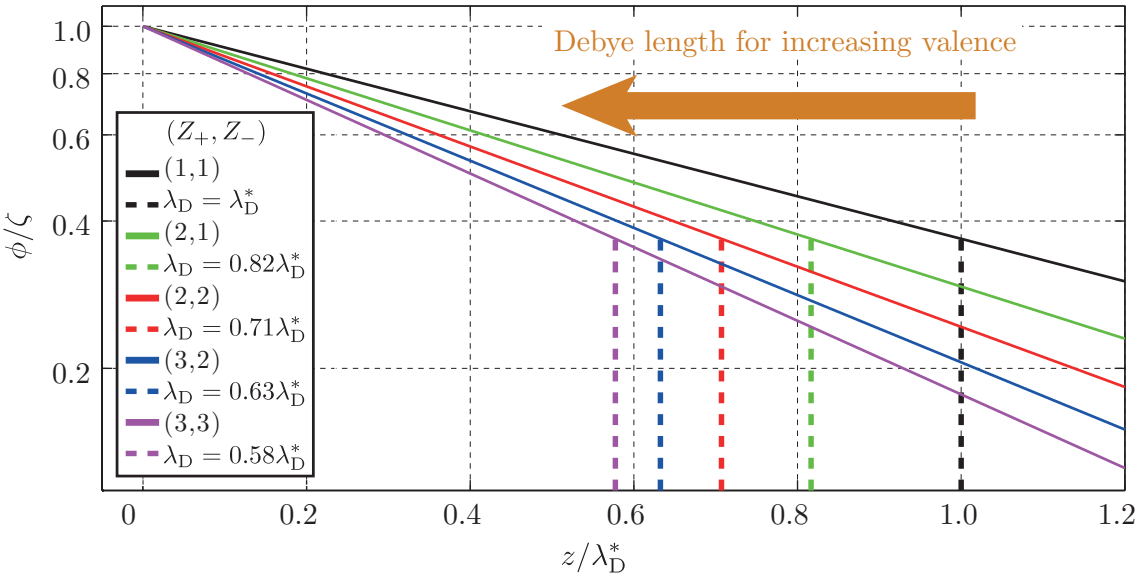

Figure A.2: A log-lin plot of the potential $\phi(z)$ (full lines) for $0 < z < 1.2\lambda_D^*$ near an infinite planar surface placed at $z = 0$ for different valences in an electrolyte at fixed charge molarity (and hence fixed λ_D^*) containing only one ion pair. The dashed lines represent the corresponding Debye lengths.

where

$$\lambda_D^* \equiv \sqrt{\frac{\epsilon k_B T}{2e^2 c_*^b}}, \tag{A.13}$$

is the standard Debye length introduced in Eq. (2.17) with $c_o = c_*^b$. The Debye length for a system containing only one type of cation and anion, corresponding to $\mathcal{N} = 1$ in Eq. (A.12), with valences N_+ and N_-, respectively, is

$$\lambda_D(\mathcal{I}) = \lambda_D^*(c_*^b)\sqrt{\frac{2}{N_+ + N_-}}. \tag{A.14}$$

Now let the two types of ions have the same valence N. The Debye length then reduces to Eq. (2.17) as expected.

The charge molarity is very advantegous since the form of the Debye length as given in Eq. (A.13) provides comparability of systems with ions of high valence to systems with ions of low valence by keeping the total charge molarity, that is, the total number of charges per unit volume in the bulk constant. This allows for the following analysis of the change in the screening ability of the ions when e.g. collecting more charge on fewer particles.

A.1.3 The Electric Potential for Constant Charge Molarity

The potential at a distance z away from the wall for arbitrary combinations of valences in a specie consisting of one ion pair can be found by inserting Eq. (A.14) into Eq. (A.10). Impose the boundary conditions that the potential must be ζ at the wall and decay to zero at infinity, and solve for the potential as a function of z. The result is

$$\phi(z) = \zeta \exp\left(-\frac{z}{\lambda_{\mathrm{D}}(N_+, N_-)}\right), \tag{A.15}$$

and is plotted for a constant charge molarity c_*^{b} in Fig. A.2 for different valence combinations. We have assumed that the ζ potential is independent of the ionic strength which we show in later chapters is not the case confer Fig. 4.11. Since the Debye length is independent of the ζ potential the assumption will not affect our results in this section. Note that Eq. (A.15) is symmetric in N_+ and N_- which is a result of Eq. (A.8) being invariant to interchanging the signs of the ions. Furthermore, all combinations with the same sum of N_+ and N_- yield the same result. The abscissa is the distance from the wall in units of the standard Debye length defined in Eq. (A.13), and the logarithmic ordinate is the potential in units of the ζ potential always present at the wall. The semilogarithmic plot turns Eq. (A.15) into straight lines each with slope $-\left\{\frac{1}{2}\left(N_{+,i} + N_{-,i}\right)\right\}^{\frac{1}{2}}$. Since the ζ potential is assumed independent of the species present in the fluid the potential should be unity for all graphs when $z/\lambda_{\mathrm{D}}^* = 0$, which is also seen to be the case. The vertical lines represent the Debye length of the graph with matching color.

The results suggest that distributing a certain fixed amount of charge on fewer ions, that is, increasing the valence number of each individual ion and at the same time reducing the molar concentration to keep c_*^{b} fixed, decreases the Debye length. On the contrary, distributing a certain fixed amount of charges such that each ion gets as few as possible (unity being the lower limit) increases the Debye length. These effects can be understood by going back to the expression for the chemical potential, Eq. (2.8), here given for the counterion with the third term having the same sign as the charge of the counterion

$$\mu(z) = \mu_{0,\pm} + \underbrace{k_{\mathrm{B}}T \ln\left(\frac{c(z)}{c_{\mathrm{o}}}\right)}_{\text{Entropy contribution}} \qquad \underbrace{\pm Ne\phi(z).}_{\text{Electric potential contribution}} \tag{A.16}$$

As indicated in Eq. (A.16) the diffusive layer can be thought of as the result of two opposing energies in equilibrium, namely the entropy energy and the electric potential energy. Assume now that an electrolyte of concentration c_{o} contacts a neutral wall. The counterions will distribute themselves homogeneously throughout space and the chemical potential is $\mu(z) = \mu_{0,+}$. Let now $\mu_{0,+} = 0$.[1] At time $t_0 = 0^+$ a negative wall potential is suddenly switched on and the chemical potential in this instant becomes

$$\mu(z) = -Ne|\phi_{\mathrm{a}}| \quad (z < \infty), \tag{A.17}$$

[1] or equivalently define a new chemical potential $\mu_{\mathrm{scaled}}(z)$ which is zero when the electric potential is zero.

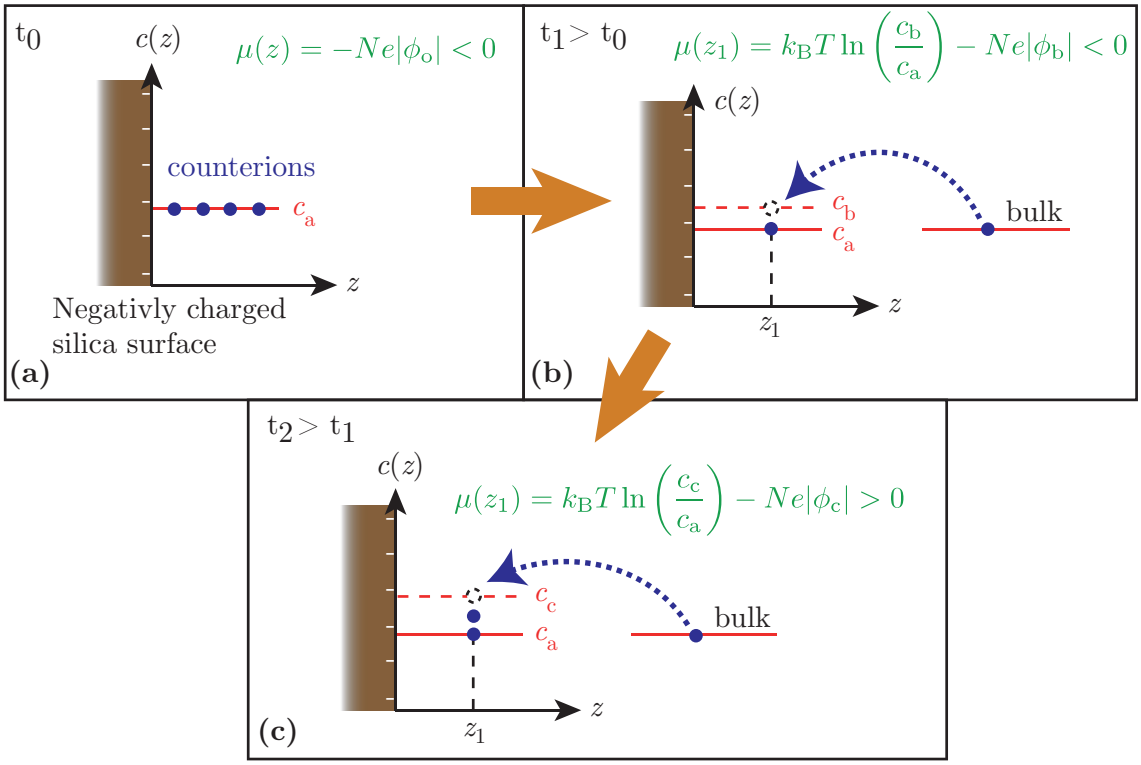

Figure A.3: Illustration supporting chemical potential arguments of why ions of higher valence lead to a lower Debye length. The brown area is the wall with white negative wall ions. The counterions are the blue circles. In each figure the chemical potential and its sign is stated (green equation). **(a)** is the system at time $t_0 = 0^+$, **(b)** the system at time $t_1 > t_0$, and **(c)** the system at time $t_2 > t_1$. The orange arrows indicate the temporal development of the system.

see Fig. A.3(a). Since $\mu(z) < 0$ the system will spontaneously begin adding particles from the bulk (infinite reservoir) to different points in space. Consider specifically one such point z_1. When adding an extra particle to z_1 the concentration becomes $c(z_1)$ and since this is greater than c_o a positive entropy term arises in the chemical potential and the potential energy changes

$$\mu(z_1) = k_B T \ln\left(\frac{c_b}{c_a}\right) - Ne|\phi_b|. \tag{A.18}$$

If $\mu(z_1) < 0$ after this particle addition the particle will be moved, see Fig. A.3(b). Adding another particle to z_1 increases the concentration to c_c and changes the potential so

$$\mu(z_1) = k_B T \ln\left(\frac{c_c}{c_a}\right) - Ne|\phi_c|. \tag{A.19}$$

This time though, the entropy term becomes larger than the negative potential term which makes the chemical potential positive $\mu(z_1) > 0$ if the particle is moved see Fig. A.3(c).

Since this is equivalent to a positive change in Gibbs free energy confer Eq. (2.7) it is not favorable for the system to move the particle and the concentration at z_1 has reached its equilibrium value $c(z_1)$. Finally, the potential term in $\mu(z)$ becomes increasingly negative with the counterion valence allowing the concentration of ions everywhere to increase for higher valence counterions. A higher concentration of counterions each with more charge screens the wall more effectively and the Debye length will decrease. When the co-ions have higher valence they are expelled more from the wall leaving the counterions in the diffusive layer only having to screen the wall which is more effective decreasing the Debye length.

A.2 Debye Length for a Double Pair Electrolyte

We move on to study an electrolyte containing two ion pairs in thermal equilibrium with a wall. The first electrolyte is assumed to dissociate into monovalent ions as is the case with e.g. the salt KCl splitting into K^+ and Cl^-. The second electrolyte dissociates into one divalent cation and two monovalent anions as could be the case for e.g. the salt CaI_2 splitting into one Ca^{2+} ion and two I^- ions. From Eq. (A.5) the bulk concentration of one electrolyte's cation can be expressed in terms of the other

$$c_{\mathrm{Ca}^{2+}} = \frac{1}{N_{\mathrm{Ca}^{2+}}}\left(c_*^{\mathrm{b}} - N_{\mathrm{K}^+}c_{\mathrm{K}^+}^{\mathrm{b}}\right), \quad \text{and} \quad c_{\mathrm{K}^+} = \frac{1}{N_{\mathrm{K}^+}}\left(c_*^{\mathrm{b}} - N_{\mathrm{Ca}^{2+}}c_{\mathrm{Ca}^{2+}}^{\mathrm{b}}\right). \tag{A.20}$$

The ratio of the Debye length λ_{D} to λ_{D}^* is found from Eq. (A.12) with $\mathcal{N} = 2$ and using Eq. (A.1)

$$\frac{\lambda_{\mathrm{D}}}{\lambda_{\mathrm{D}}^*} = \sqrt{2}\left[(N_{\mathrm{K}^+} + N_{\mathrm{Cl}^-})\left(1 - \frac{N_{\mathrm{Ca}^{2+}}c_{\mathrm{Ca}^{2+}}^{\mathrm{b}}}{c_*^{\mathrm{b}}}\right) + (N_{\mathrm{Ca}^{2+}} + N_{\mathrm{I}^-})\left(1 - \frac{N_{\mathrm{K}^+}c_{\mathrm{K}^+}^{\mathrm{b}}}{c_*^{\mathrm{b}}}\right)\right]^{-\frac{1}{2}}.$$

Inserting $N_{\mathrm{K}^+} = N_{\mathrm{Cl}^-} = N_{\mathrm{I}^-} = 1$, $N_{\mathrm{Ca}^{2+}} = 2$, and using Eq. (A.20) to eliminate $c_{\mathrm{Ca}^{2+}}$ the ratio becomes a function of $c_{\mathrm{K}^+}^{\mathrm{b}}$

$$\begin{aligned}\frac{\lambda_{\mathrm{D}}}{\lambda_{\mathrm{D}}^*}(c_{\mathrm{K}^+}^{\mathrm{b}}) &= \sqrt{2}\left[2\left(1 - \frac{2c_{\mathrm{Ca}^{2+}}^{\mathrm{b}}}{c_*^{\mathrm{b}}}\right) + 3\left(1 - \frac{c_{\mathrm{K}^+}^{\mathrm{b}}}{c_*^{\mathrm{b}}}\right)\right]^{-\frac{1}{2}} \\ &= \sqrt{2}\left(3 - \frac{c_{\mathrm{K}^+}^{\mathrm{b}}}{c_*^{\mathrm{b}}}\right)^{-\frac{1}{2}}, \quad c_{\mathrm{Ca}^{2+}}^{\mathrm{b}} = \frac{1}{2}\left(c_*^{\mathrm{b}} - c_{\mathrm{K}^+}^{\mathrm{b}}\right). \end{aligned} \tag{A.21}$$

Similarly

$$\frac{\lambda_{\mathrm{D}}}{\lambda_{\mathrm{D}}^*}(c_{\mathrm{Ca}^{2+}}^{\mathrm{b}}) = \left(1 + \frac{c_{\mathrm{Ca}^{2+}}^{\mathrm{b}}}{c_*^{\mathrm{b}}}\right)^{-\frac{1}{2}}, \quad c_{\mathrm{K}^+}^{\mathrm{b}} = c_*^{\mathrm{b}} - 2c_{\mathrm{Ca}^{2+}}^{\mathrm{b}}. \tag{A.22}$$

Eq. (A.21) should be understood as follows: given a concentration of K^+ the concentration of Ca^{2+} is immediately determined because the charge molarity is constant. If instead

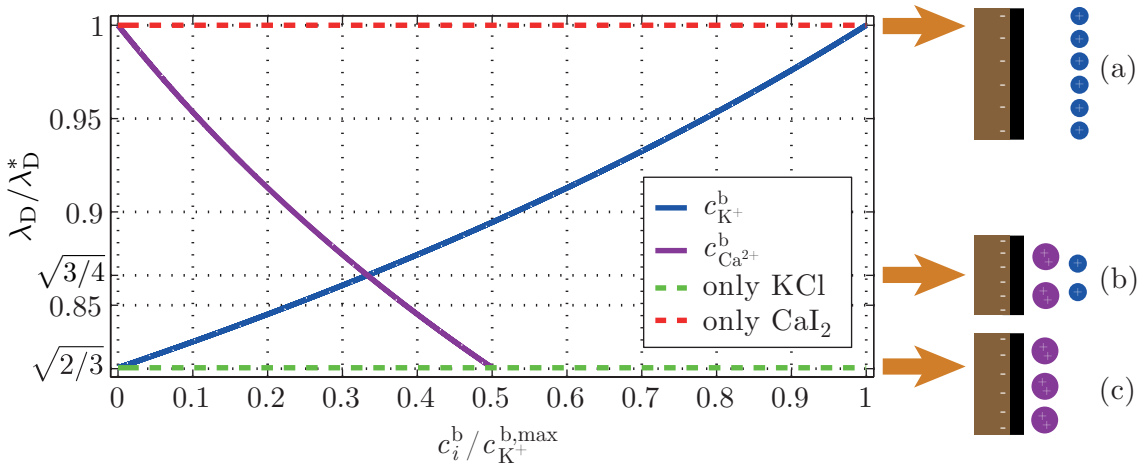

Figure A.4: The relative Debye length λ_D/λ_D^* plotted versus the bulk concentration for electrolytes consisting of different pairs. The charge molarity c_*^b is kept constant which couples the two graphs: when a cation concentration has been determined on the blue (black) graph, the intersection of a horizontal line from this point with the black (blue) graph, determines the concentration of the other cation. The dashed lines indicate the Debye length when only one of the electrolytes is present. The drawings in the far right shows a simplified picture of the general trend in the position of ions with different valences.

the concentration of Ca^{2+} is known Eq. (A.22) determines the concentration of K^+ in a similar way. A plot of Eqs. (A.21) and (A.22) is seen in Fig. A.4. For a given Debye length ratio λ_D/λ_D^* the concentration of each cation can be found by reading the graph horizontally. E.g. for $\lambda_D/\lambda_D^* = 0.9$ in the plot the concentration ratio for K^+: $c_{K^+}^b/c_{K^+}^{b,max} \simeq 0.53$, and for Ca^{2+}: $c_{Ca^{2+}}^b/c_{K^+}^{b,max} \simeq 0.24$. Note that in this specific example $c_{K^+}^{b,max} = c_*^b$. It is seen that when only KCl is present, that is, when $c_{Ca^{2+}}^b = 0$ the concentration ratio $c_{K^+}^b/c_{K^+}^{b,max}$ becomes unity because it is normalized to its own maximum. Since KCl is a monovalent electrolyte, a solution only containing KCl should give the standard Debye length per definition, and this is also seen to be the case. Likewise it is seen that when only CaI_2 is present, i.e. when $c_{K^+}^b = 0$, the Debye length becomes $\sqrt{2/3} \simeq 0.816$. This follows immediately from Eq. (A.21). It is also seen that in this case the concentration ratio $c_{Ca^{2+}}^b/c_{K^+}^{b,max}$ is only $1/2$. This is because Ca^{2+} has double the valence as K^+ and the charge molarity must be constant. A special case arises when the concentrations of the cations are equal. The Debye length ratio λ_D/λ_D^* here can be found from e.g. Eq. (A.22) to be $\sqrt{3/4} \simeq 0.866$. This is seen at the intersection of the two curves.

It is observed that the Debye length ratio for equal cation concentrations is closer to that obtained in a solution only consisting of the higher valence electrolyte. This is a result of the requirement of constant molarity. To see why, one must refer to the cartoon drawings of the screening counterions near the negatively charged wall in Fig. A.4 to the far right. The top drawing represents a system (a) where the solution contains only KCl, the middle

drawing a system (b) where the cation concentrations of KCl and CaI_2 are equal and the bottom drawing a system (c) where the solution contains only CaI_2. The distribution of the ions is of course continuous, assuming point particles, but the Debye length can be thought of as the distance at which the wall is effectively screened by the counterions as in the early Helmholtz model. Systems (a) and (c) show a Helmholtz model of the system by placing all the screening charge in a one Debye length distance from the wall. System (b) shows the general trend that ions with higher positive valence will statistically be closer to the wall confer Eq. (2.8). In system (b) the cation concentrations are equal and shows that the charge distribution resembles system (c) more than system (a). The drawings suggest that system (b) can loosely be thought of as a mix between 2/3 of system (c) and 1/3 of system (a). Therefore it should be expected that the Debye length in system (b) will be closer to that in system (c) than that in system (a) which is also seen in the graph.

A.3 Actual Concentrations in the Bulk

In this section we discuss how to calculate the actual concentrations of all ions in an electrolyte in the bulk. When the electrolyte is created by the experimentalist in macroscopic containers and when it enters the reservoirs both are on a length scale where the ions are not affected by the potential from the walls. Therefore, everywhere in the reservoir the concentrations are considered bulk concentrations. The concentrations in the middle of the nanochannel are also bulk concentrations when there is no diffusive layer overlap, $\lambda_D \ll h$.

The Santiago group provides a MatLab script in Ref. [14] referred to as the Santiago script which calculates the actual concentrations of acids and bases from the pK values of all dissociation reactions and formal concentrations of all added solutes. We have modified this script and use it to calculate the actual bulk concentrations of the ions in our solutions. The modified script can be seen in Appendix C.1.

The script is build upon the idea that the dissociation reactions of acids, bases, and salts can be formulated in equivalent acid dissociation reactions. A thorough description of the underlying theory behind the script is found in Ref. [6] and in the following section we will state the governing equations for the actual concentrations in the bulk solution.

Governing Equations

The general form of the dissociation reaction of an acid HA is

$$\mathrm{HA} \rightleftharpoons \mathrm{A^-} + \mathrm{H^+}, \tag{A.23}$$

where $\mathrm{A^-}$ is the conjugate base. Naturally, all acids and bases are on this acid dissociation form. As examples take the dissociation reactions of the strong acid HCl and the strong base KOH dissolved in water

$$\mathrm{HCl_{(s)}} \rightleftharpoons \mathrm{H^+_{(aq)}} + \mathrm{Cl^-_{(aq)}}, \tag{A.24}$$

$$\mathrm{KOH_{(s)}} \rightleftharpoons \mathrm{OH^-_{(aq)}} + \mathrm{K^+_{(aq)}}. \tag{A.25}$$

However, in order to model dissolved salts the dissociation reaction must be divided into equivalent acid dissociation forms. Consider as an example the dissociation of the salt KCl

$$\mathrm{KCl_{(s)}} \rightleftharpoons \mathrm{Cl^-_{(aq)}} + \mathrm{K^+_{(aq)}}. \tag{A.26}$$

1 mM KCl is mathematically equivalent to mixing 1 mM HCl with 1 mM KOH. Therefore, instead of writing salt dissociations on the form Eq. (A.26) they can be written on acid dissociaton forms as Eqs. (A.24) and (A.25).

Now let X denote a general acid. We omit the H in front of X for notational reasons. The dissociation reactions of X into charge states X^z with valence z can be generalized as

$$\mathrm{X}^{p_\mathrm{X}} \rightleftharpoons \mathrm{X}^{p_\mathrm{X}-1} + \mathrm{H}^+, \quad K_{\mathrm{X},p_\mathrm{X}-1}, \tag{A.27}$$
$$\mathrm{X}^{p_\mathrm{X}-1} \rightleftharpoons \mathrm{X}^{p_\mathrm{X}-2} + \mathrm{H}^+, \quad K_{\mathrm{X},p_\mathrm{X}-2}, \tag{A.28}$$
$$\ldots$$
$$\mathrm{X}^{n_\mathrm{X}+1} \rightleftharpoons \mathrm{X}^{n_\mathrm{X}} + \mathrm{H}^+, \quad K_{\mathrm{X},n_\mathrm{X}}, \tag{A.29}$$

where n_X and p_X are the minimum and maximum possible valence of the zth state, respectively. The general dissociation constant for each acid reaction in Eqs. (A.27)–(A.29) is on the form

$$K_{\mathrm{X},z} = \frac{c_{\mathrm{X},z}\, c_\mathrm{H}}{c_{\mathrm{X},z+1}}, \tag{A.30}$$

where $c_{\mathrm{X},z}$ is the concentration of the charge state X^z . The total number of dissociation reactions each with a dissociation constant $K_{\mathrm{X},z}$ is $r_\mathrm{X} = p_\mathrm{X} - n_\mathrm{X}$. The set of charge states X^z with $z \in [n_\mathrm{X}, p_\mathrm{X}]$ is dubbed a family. The sum over the concentrations in the family is the formal concentration of the acid X,

$$c_\mathrm{X} = \sum_{z=n_\mathrm{X}}^{p_\mathrm{X}} c_{\mathrm{X},z} \quad \text{(mass-conservation)}. \tag{A.31}$$

This is a conservation-of-mass relation for each family. The concentrations of dissociated states including the hydrons and the hydroxide ions must satisfy charge neutrality in the bulk,

$$\sum_\mathrm{X} \sum_{z=n_\mathrm{X}}^{p_\mathrm{X}} z c_{\mathrm{X},z} + c_\mathrm{H} - c_\mathrm{OH} = 0 \quad \text{(bulk charge neutrality)}. \tag{A.32}$$

The last equation needed is the autoprotolysis of water

$$\mathrm{H_2O} \rightleftharpoons \mathrm{H^+} + \mathrm{OH^-}, \tag{A.33}$$

with the hydron and hydroxide ion concentrations satisfying

$$K_\mathrm{w} = c_\mathrm{H}\, c_\mathrm{OH}, \tag{A.34}$$

where K_w is the self-ionization constant of water.

The concentrations $c_{\mathrm{X},z}$ from each family X together with c_{H} and c_{OH} are unknowns. The formal concentration of each family c_{X}, information on which charge states are created for each family, and the dissociation constant for each of these dissociation reactions must be known. Counting the unknowns in the above equations we get

$$\underbrace{2}_{c_{\mathrm{H}},\,c_{\mathrm{OH}}} + \sum_{\mathrm{X}} \underbrace{(1 + r_{\mathrm{X}})}_{c_{\mathrm{X},z}}. \tag{A.35}$$

The number of available equations are

$$\underbrace{2}_{\text{Eqs. (A.32),(A.34)}} + \sum_{\mathrm{X}} \underbrace{(1}_{\text{Eq. (A.31)}} + \underbrace{r_{\mathrm{X}})}_{\text{Eq. (A.30)}}, \tag{A.36}$$

and is seen to be sufficient to determine the actual bulk concentrations of the system.

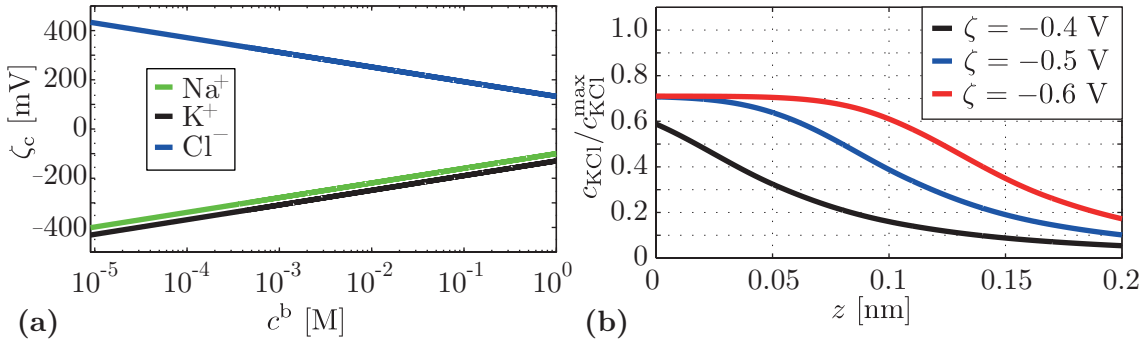

Figure A.5: **(a)** a lin-log plot of the critical ζ potential ζ_c for bulk concentrations c^b between 10 µM and 1 M of the ions modeled in this thesis. The critical concentrations have been determined from Ref. [25]. **(b)** solutions of the modified Poisson–Boltzmann equation using the concentrations in Eq. (A.37) plotted at room temperature for different ζ potentials for KCl with $c^b = 0.1$ mM and hydrated radius 0.125 nm. For the black graph $c(0) = 5.30 \times 10^{28}$ m^{-3}, for the blue graph $c(0) = 6.37 \times 10^{28}$ m^{-3}, and for the red graph $c(0) = 6.40 \times 10^{28}$ m^{-3}.

A.4 Steric Effects

The Boltzmann distribution of ions Eq. (2.11) can predict infinitely large concentrations for sufficiently high voltages. For example, consider 1 mM NaCl at room temperature $k_B T$=25.9 mV and let the wall be negatively charged by an external potential source with $\zeta = -1$ V.[2] The concentration of Na^+ ions at the wall predicted by the Boltzmann distribution is 5.86×10^{13} M $= 3.5 \times 10^{40}$ m^{-3}. This correspond to an ionic center-to-center distance of $\left(3.5 \times 10^{40}\ \text{m}^{-3}\right)^{-1/3} \simeq 3 \times 10^{-14}$ m. The radius of the sodium atom is approximately 0.17 nm, so the distribution clearly predicts unphysical results, and since the Poisson–Boltzmann equation Eq. (2.23) is based on the Boltzmann distribution it means that for sufficiently high voltages neither equation is valid. The modified Poisson–Boltzmann equation takes into account the finite size of the ions and uses the concentration expression Eq. (A.37) instead of Eq. (2.11). It puts an upper bound on the number of ions able to fit into a given volume when assuming a certain way they pack together. For a binary symmetric electrolyte the concentrations c_i are [24]

$$c_i(\mathbf{r}) = \frac{c_i^b \exp\left(-\frac{Z_i e}{k_B T}\phi(\mathbf{r})\right)}{1 + 2\nu \sinh^2\left(\frac{Z_i e}{2k_B T}\phi(\mathbf{r})\right)}, \tag{A.37}$$

where $\nu = 2\alpha_{ion}^3 c^b$ is the packing parameter, α_{ion} the effective ion size considered here as the diameter of the hydrated ion but need not be, $c^b = c_+^b = c_-^b$ in the case of a binary electrolyte, c_i^b, Z_i the concentration in the bulk and sign-carrying valence of the ith ion respectively, e the elementary charge, and $\phi(\mathbf{r})$ is the potential at the spatial point $\mathbf{r}$. The

[2] Normally $|\zeta| \lesssim 100$ mV without external sources.

atoms are assumed to pack in a face centered cubic model each atom occupying a volume of α_{ion}^3. The authors of Ref. [25] provide a table with values for the hydrated ion radius for some of the most modeled ions. The maximum allowed potential at the wall before the ith counterion concentration becomes too large can be found by isolating $\phi(\mathbf{r})$ in Eq. (2.11) and evaluating it at the wall where it equals ζ per definition

$$\zeta_{\text{c}} = \frac{k_{\text{B}}T}{Z_i e}\left[\ln\left(c_i^{\text{b}}\right) - \ln\left(c_i^{\max}\right)\right], \tag{A.38}$$

where $c_i^{\max}$ is the largest physically possible concentration assuming the face centered cubic packing and that the ions have the hydrated radii as given in Ref. [25].

In Fig. A.5(a) ζ_{c} is plotted versus the bulk ionic concentration for different ions modeled in this thesis. A plot of solutions to the modified Poisson–Boltzmann equation using the concentrations Eq. (A.37) for KCl of bulk concentration 0.1 mM at room temperature with a negatively charged wall at three different potentials -0.4, -0.5, and -0.6 V can be seen in Fig. A.5(b). The concentration at the most critical place closest to the wall is seen to be less than its maximum allowed value. This is a consequence of the minimization of the Helmholtz free energy. The higher the voltage the more nonlinear the problem becomes, and this creates difficulties when simulating the concentrations. For high enough voltages the concentration will attain its maximum value. It is also seen how the concentrations increase in a distance further away from the wall when the potential increases.

A.5 Derivation of Surface Coverages for the Metal Adsorption Model

In this section the expression

$$\theta_i = \frac{\mathcal{K}_i f_i}{1 + \sum_j \mathcal{K}_j f_j}, \quad i,j = \{\mathrm{SiOH_2^+}, \mathrm{SiOH}, \mathrm{SiOM}\}, \tag{A.39}$$

for the ith surface coverage will be derived. The starting point is Eqs. (3.18), (3.28), and (3.29) also stated below

$$\begin{aligned}
K_- &= \frac{\theta_{\mathrm{SiO^-}}}{\theta_{\mathrm{SiOH}}} c_{\mathrm{H}}^{\mathrm{b}} \exp\left(-\frac{e}{k_{\mathrm{B}}T}\phi_{\mathrm{o}}\right), && \text{(A.40)}\\
K_+ &= \frac{\theta_{\mathrm{SiOH}}}{\theta_{\mathrm{SiOH_2^+}}} c_{\mathrm{H}}^{\mathrm{b}} \exp\left(-\frac{e}{k_{\mathrm{B}}T}\phi_{\mathrm{o}}\right), && \text{(A.41)}\\
K_{\mathrm{M}} &= \frac{\theta_{\mathrm{SiOM}}}{\theta_{\mathrm{SiO^-}}} \left(c_{\mathrm{M}}^{\mathrm{b}}\right)^{-1} \exp\left(\frac{e}{k_{\mathrm{B}}T}\phi_{\beta}\right), && \text{(A.42)}\\
1 &= \theta_{\mathrm{SiOH}} + \theta_{\mathrm{SiOH_2^+}} + \theta_{\mathrm{SiO^-}} + \theta_{\mathrm{SiOM}}. && \text{(A.43)}
\end{aligned}$$

First, an expression for the surface coverage $\theta_{\mathrm{SiOH_2^+}}$ will be derived. Rewriting Eqs. (A.40)–(A.43) gives

$$\begin{aligned}
\theta_{\mathrm{SiOH_2^+}} &= \theta_{\mathrm{SiOH}} (K_+)^{-1} c_{\mathrm{H}}^{\mathrm{b}} \exp\left(-\frac{e}{k_{\mathrm{B}}T}\phi_{\mathrm{o}}\right), && \text{(A.44)}\\
\theta_{\mathrm{SiOH}} &= \theta_{\mathrm{SiO^-}} (K_-)^{-1} c_{\mathrm{H}}^{\mathrm{b}} \exp\left(-\frac{e}{k_{\mathrm{B}}T}\phi_{\mathrm{o}}\right), && \text{(A.45)}\\
\theta_{\mathrm{SiOM}} &= \theta_{\mathrm{SiO^-}} K_{\mathrm{M}}\ c_{\mathrm{M}}^{\mathrm{b}} \exp\left(-\frac{e}{k_{\mathrm{B}}T}\phi_{\beta}\right), && \text{(A.46)}\\
\theta_{\mathrm{SiO^-}} &= 1 - \theta_{\mathrm{SiOH}} - \theta_{\mathrm{SiOH_2^+}} - \theta_{\mathrm{SiOM}}. && \text{(A.47)}
\end{aligned}$$

Insert Eq. (A.45) into Eq. (A.44) to get

$$\theta_{\mathrm{SiOH_2^+}} = \theta_{\mathrm{SiO^-}} \left(K_- K_+\right)^{-1} \left(c_{\mathrm{H}}^{\mathrm{b}}\right)^2 \exp\left(-\frac{2e}{k_{\mathrm{B}}T}\phi_{\mathrm{o}}\right). \tag{A.48}$$

Insert Eqs. (A.45) and (A.46) in Eq. (A.47) and isolate $\theta_{\mathrm{SiO^-}}$

$$\theta_{\mathrm{SiO^-}} = \frac{1 - \theta_{\mathrm{SiOH_2^+}}}{1 + K_{\mathrm{M}} c_{\mathrm{M}}^{\mathrm{b}} \exp\left(-\frac{e}{k_{\mathrm{B}}T}\phi_{\beta}\right) + \left(K_-\right)^{-1} c_{\mathrm{H}}^{\mathrm{b}} \exp\left(-\frac{e}{k_{\mathrm{B}}T}\phi_{\mathrm{o}}\right)}. \tag{A.49}$$

This is inserted in Eq. (A.48) and $\theta_{\mathrm{SiOH_2^+}}$ is isolated

$$\theta_{\mathrm{SiOH_2^+}} = \frac{\mathcal{K}_{\mathrm{SiOH_2^+}} f_{\mathrm{SiOH_2^+}}}{1 + \mathcal{K}_{\mathrm{SiOM}} f_{\mathrm{SiOM}} + \mathcal{K}_{\mathrm{SiOH}} f_{\mathrm{SiOH}} + \mathcal{K}_{\mathrm{SiOH_2^+}} f_{\mathrm{SiOH_2^+}}}, \tag{A.50}$$

where

$$\mathcal{K}_{\mathrm{SiOH}} \equiv \left(K_-\right)^{-1}, \quad f_{\mathrm{SiOH}} \equiv c_{\mathrm{H}}^{\mathrm{b}} \exp\left(-\frac{e}{k_{\mathrm{B}}T}\phi_{\mathrm{o}}\right), \tag{A.51}$$

$$\mathcal{K}_{\mathrm{SiOM}} \equiv K_{\mathrm{M}}, \quad f_{\mathrm{SiOM}} \equiv c_{\mathrm{M}}^{\mathrm{b}} \exp\left(-\frac{e}{k_{\mathrm{B}}T}\phi_{\beta}\right), \tag{A.52}$$

$$\mathcal{K}_{\mathrm{SiOH_2^+}} \equiv \left(K_- K_+\right)^{-1}, \quad f_{\mathrm{SiOH_2^+}} \equiv \left(c_{\mathrm{H}}^{\mathrm{b}}\right)^2 \exp\left(-\frac{2e}{k_{\mathrm{B}}T}\phi_{\mathrm{o}}\right) = \left(f_{\mathrm{SiOH}}\right)^2. \tag{A.53}$$

Next, the surface coverage θ_{SiOH} will be derived. Inserting Eqs. (A.44) and (A.46) in Eq. (A.47) and isolating $\theta_{\mathrm{SiO^-}}$ leads to

$$\theta_{\mathrm{SiO^-}} = \frac{1 - \theta_{\mathrm{SiOH}}\left[1 + \left(K_+\right)^{-1} c_{\mathrm{H}}^{\mathrm{b}} \exp\left(-\frac{e}{k_{\mathrm{B}}T}\phi_{\mathrm{o}}\right)\right]}{1 + K_{\mathrm{M}} c_{\mathrm{M}}^{\mathrm{b}} \exp\left(-\frac{e}{k_{\mathrm{B}}T}\phi_{\beta}\right)}. \tag{A.54}$$

Insert this in Eq. (A.45) and isolate θ_{SiOH} to get

$$\theta_{\mathrm{SiOH}} = \frac{\mathcal{K}_{\mathrm{SiOH}} f_{\mathrm{SiOH}}}{1 + \mathcal{K}_{\mathrm{SiOM}} f_{\mathrm{SiOM}} + \mathcal{K}_{\mathrm{SiOH}} f_{\mathrm{SiOH}} + \mathcal{K}_{\mathrm{SiOH_2^+}} f_{\mathrm{SiOH_2^+}}}, \tag{A.55}$$

where the definitions in Eqs. (A.51)–(A.53) have been used. Finally the surface coverage θ_{SiOM} will be derived. By inserting Eqs. (A.45) and (A.48) in Eq. (A.47) and isolating $\theta_{\mathrm{SiO^-}}$ gives

$$\theta_{\mathrm{SiO^-}} = \frac{1 - \theta_{\mathrm{SiOM}}}{1 + K_-^{-1} c_{\mathrm{H}}^{\mathrm{b}} \exp\left(-\frac{e}{k_{\mathrm{B}}T}\phi_{\mathrm{o}}\right) + \left(K_- K_+\right)^{-1} \left(c_{\mathrm{H}}^{\mathrm{b}}\right)^2 \exp\left(-\frac{e}{k_{\mathrm{B}}T} 2\phi_{\mathrm{o}}\right)}. \tag{A.56}$$

This is inserted in Eq. (A.46) and θ_{SiOM} is isolated leading to

$$\theta_{\mathrm{SiOM}} = \frac{\mathcal{K}_{\mathrm{SiOM}} f_{\mathrm{SiOM}}}{1 + \mathcal{K}_{\mathrm{SiOM}} f_{\mathrm{SiOM}} + \mathcal{K}_{\mathrm{SiOH}} f_{\mathrm{SiOH}} + \mathcal{K}_{\mathrm{SiOH_2^+}} f_{\mathrm{SiOH_2^+}}}. \tag{A.57}$$

By using Eq. (A.47) with the results for the three surface coverages Eqs. (A.50), (A.55), and (A.57) the surface coverage $\theta_{\mathrm{SiO^-}}$ is

$$\theta_{\mathrm{SiO^-}} = \left(1 + \mathcal{K}_{\mathrm{SiOM}} f_{\mathrm{SiOM}} + \mathcal{K}_{\mathrm{SiOH}} f_{\mathrm{SiOH}} + \mathcal{K}_{\mathrm{SiOH_2^+}} f_{\mathrm{SiOH_2^+}}\right)^{-1}. \tag{A.58}$$

A.6 Numerical Solution of the Poisson–Boltzmann Equation

The electric potential is an essential physical quantity when studying electrokinetics in nanofludic systems. The channels used in our work are rectangular and have a much larger width than height $w \gg h$. Therefore, we solve the Poisson–Boltzmann equation numerically in an infinite parallel plate channel. To increase accuracy in the numerical calculations avoiding truncation errors we make the equation dimensionless and thereby on the order of unity.

In an infinite parallel plate channel the Poisson–Boltzmann equation Eq. (2.23) becomes one-dimensional with z as the co-ordinate between the bounding plates

$$\partial_z^2 \phi(z) = -\frac{e}{\epsilon} \sum_{i=1}^{\mathcal{N}} Z_i c_i^{\mathrm{b}} \exp\left(-\frac{Z_i e}{k_{\mathrm{B}} T} \phi(z)\right). \tag{A.59}$$

There are two boundary conditions for this second order ordinary differential equation. First, the potential is ζ at the wall and second, the spatial derivative of the potential in the mid channel is zero since the electric potential must be spatially symmetric. Place the origin on a bounding plate parallel to its surface normal then the boundary conditions become

$$\phi(0) = \zeta, \quad \partial_z \phi\left(\frac{h}{2}\right) = 0. \tag{A.60}$$

Define a dimensionless potential

$$\hat{\phi}(z) \equiv \frac{e}{k_{\mathrm{B}} T} \phi(z), \tag{A.61}$$

in terms of the ratio of electric potential energy to thermal energy. Define also a dimensionless position co-ordinate

$$\hat{z} \equiv \frac{z}{\lambda_D}, \tag{A.62}$$

in terms of the characteristic length over which the potential changes namely the Debye length. Eq. (A.59) on dimensionless form becomes

$$\hat{\partial}_{\hat{z}}^2 \hat{\phi}(\hat{z}) = -\sum_{i=1}^{\mathcal{N}} \frac{Z_i c_i^{\mathrm{b}}}{2\mathcal{I}} \exp\left(-Z_i \hat{\phi}(\hat{z})\right), \tag{A.63}$$

where the definition of the ionic strength Eq. (2.30) has been used. On dimensionless form the boundary conditions in Eq. (A.60) become

$$\hat{\phi}(0) = \frac{e}{k_{\mathrm{B}} T} \zeta, \quad \hat{\partial}_{\hat{z}} \hat{\phi}\left(\frac{h}{2\lambda_D}\right) = 0. \tag{A.64}$$

To numerically solve Eq. (A.63) using the built-in MatLab function `bvp4c` the second order ordinary differential equation must be transformed to a system of first order ordinary

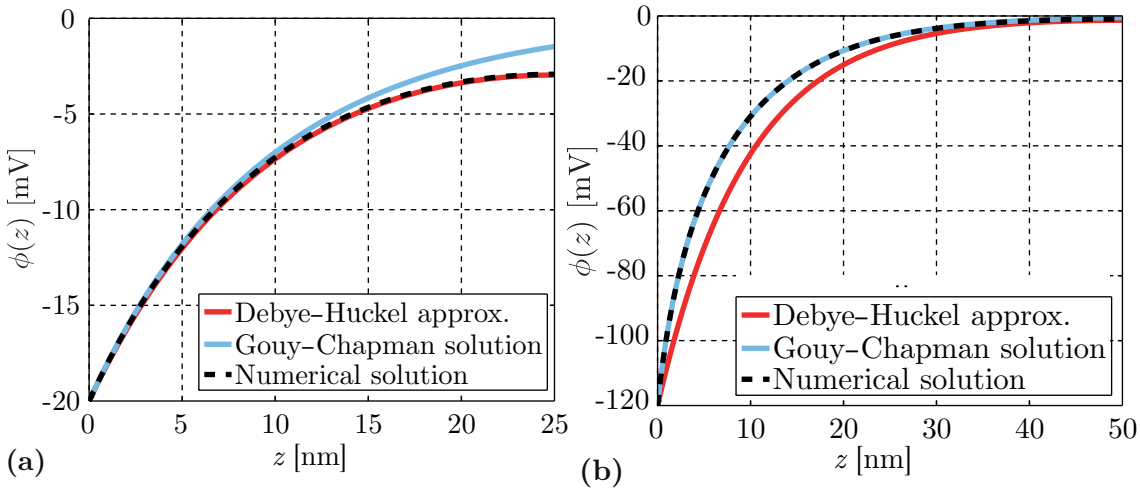

Figure A.6: **(a)** numerical solution of the electric potential in a parallel plate channel versus distance from the channel wall together with the Debye–Hückel and Gouy–Chapman solution. The number of equidistant logarithmic mesh points is 2000. The concentration of the monovalent salt is 1 mM. The channel height is 50 nm and the ζ potential is set to -20 mV. **(b)** numerical solution of the electric potential in a parallel plate channel versus distance from channel wall together with the Debye–Hückel and Gouy–Chapman solution. The number of equidistant logarithmic mesh points is 2000. The concentration of the monovalent salt is 1 mM. The channel height is 100 nm and the ζ potential is set to -120 mV. The Debye length λ_D is 10 nm.

differential equations. This can be done by defining

$$\begin{bmatrix} f_1(\hat{z}) \\ f_2(\hat{z}) \end{bmatrix} \equiv \begin{bmatrix} \hat{\phi}(\hat{z}) \\ \hat{\partial}_{\hat{z}}\hat{\phi}(\hat{z}) \end{bmatrix}. \tag{A.65}$$

The system of first order ordinary differential equations can then be written as

$$\begin{bmatrix} \hat{\partial}_{\hat{z}} f_1(\hat{z}) \\ \hat{\partial}_{\hat{z}} f_2(\hat{z}) \end{bmatrix} = \begin{bmatrix} f_2(\hat{z}) \\ -\sum_{i=1}^{\mathcal{N}} \frac{Z_i c_i^\mathrm{b}}{2\mathcal{I}} \exp\left(-Z_i \hat{\phi}(\hat{z})\right) \end{bmatrix}. \tag{A.66}$$

The size of the electric potential is expected to decrease with an exponential behavior away from the surface. Therefore, we set the distance between the mesh points to increase exponentially away from the surface. We use the built-in MatLab function `logspace` which distributes the points equidistant on a logarithmic scale. We lay points from 10^{-15} m to $h/2$ including zero.[3] The position of the mesh points are then scaled according to Eq. (A.62).

[3]The Debye length of a monovalent 1 M electrolyte is about 0.3 nm. Comparing this to the distance between the first mesh point at 0 m and the second mesh point at 10^{-15} m the potential decay should be well resolved.

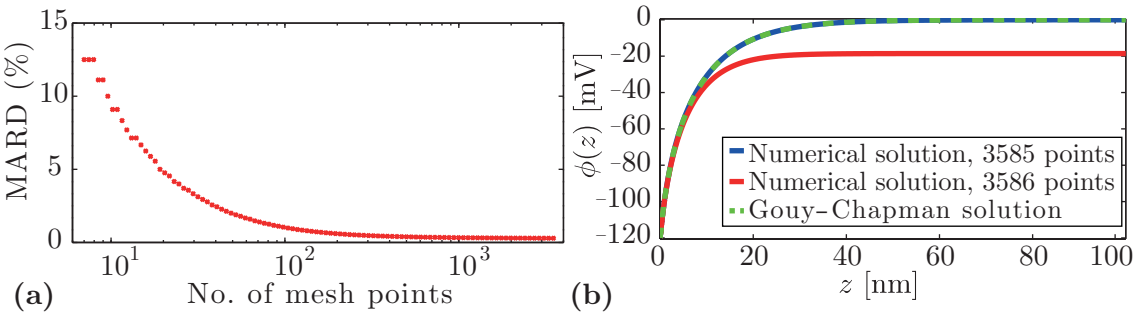

Figure A.7: **(a)** a lin-log plot of the mean absolute relative difference MARD between the numerical solution of the potential and the analytical Gouy–Chapman solution versus number of mesh points. We observe convergence and from the plot choose 1000 mesh points giving an accuracy of 0.32%. The channel height is 200 nm. The concentration of the monovalent salt is 1 mM and the ζ potential is set to -120 mV. **(b)** numerical solutions of the electric potential in parallel plate channel versus distance from the channel wall for 3585 (blue) and 3586 (red) equally logarithmic distributed mesh points. The analytical Gouy–Chapman solution (green dashed) is plotted together with the numerical solutions. The concentration of the monovalent salt is 1 mM. The channel height is 200 nm and the ζ potential is set to -120 mV.

A.6.1 Comparing Numerical and Analytical Solutions

We now numerically solve the potential in a parallel plate channel for different channel heights and ζ potentials using the MatLab script in Section C.2. In all calculations with the `bvp4c` solver we use a real tolerance and absolute tolerance of 10^{-7}. We compare our numerical solution to the Gouy–Chapman solution Eq. (2.15) valid in parallel plate channels for $\lambda_D \ll h$ and to the analytical solution in a parallel plate channel in the Debye–Hückel limit $|\zeta| \leq 26$ mV Eq. (2.18).

Numerical solutions are plotted in Fig. A.6 together with the analytical Gouy–Chapman solution Eq. (2.15) and the analytical solution valid in the Debye–Hückel limit Eq. (2.18) for channels of different heights containing a 1 mM monovalent electrolyte. In Fig. A.6(a) the ζ potential is set low at -20 mV and it is seen that the numerical solution follows the analytical Debye–Hückel solution as expected. We note that the Gouy–Chapman solution deviates from the other solutions due to the narrow channel height of 50 nm compared to the Debye length of 10 nm. The non-zero potential in the mid channel is caused by diffusive layer overlap. In Fig. A.6(b) the height is increased to 100 nm and the numerical solution coincides with the Gouy–Chapman solution. In the same figure we have set $\zeta = -120$ mV which is outside the Debye–Hückel limit so the Debye–Hückel approximated solution in this case deviates from the other solutions. Fig. A.6 verify that our numerical solution coincides with analytical solutions in their respective limits. At the same time we have shown the analytical solutions outside their valid limits.

A.6.2 Convergence Study

The number of mesh points needed to achieve a desired accuracy will be now be investigated. As a measure of having achieved convergence we use the mean absolute relative difference MARD between the numerical solution ϕ_{num} and the analytical solution ϕ_{analytic}

$$\text{MARD} = \frac{1}{\mathcal{P}} \sum_{p=1}^{\mathcal{P}} \left| \frac{\phi_{\text{num}}(z_p) - \phi_{\text{analytic}}(z_p)}{\phi_{\text{analytic}}(z_p)} \right|, \tag{A.67}$$

where $\mathcal{P}$ and z_p are the number of logarithmically equidistant mesh points and the pth mesh point, respectively. When plotting the mean absolute relative difference versus number of mesh points $\mathcal{P}$ the Gouy–Chapman solution is chosen as the analytical solution since the ζ potentials treated in this thesis are generally outside the Debye–Hückel range. We choose a 200 nm high channel containing a monovalent electrolyte of concentration 1 mM and the ζ potential is -120 mV. The mean absolute relative difference difference is plotted versus number of mesh points in Fig. A.7(a). The range of mesh points spans from 7 to 3500. The solver cannot solve the problem below 7 mesh points. For 1000 and 2000 mesh points the mean absolute relative difference is about 0.32% and 0.30%, respectively. We want as few mesh points as possible with the highest possible accuracy so we choose 1000 mesh points in our thesis.

We have plotted the numerical solution of the potential for two different number of mesh points together with the analytical Gouy–Chapman solution in Fig. A.7(b). We note that the solver returns a solution deviating significantly from the expected analytical solution when the number of mesh points exceeds 3585 in the case presented here. We observe a noticeable characteristic sharp break off in the incorrect solution. Therefore, when we solve the potential in the channel we plot it together with the Gouy–Chapman solution which will reveal any errors when solving the potential.

A.7 The Debye Length versus KCl Bulk Concentration

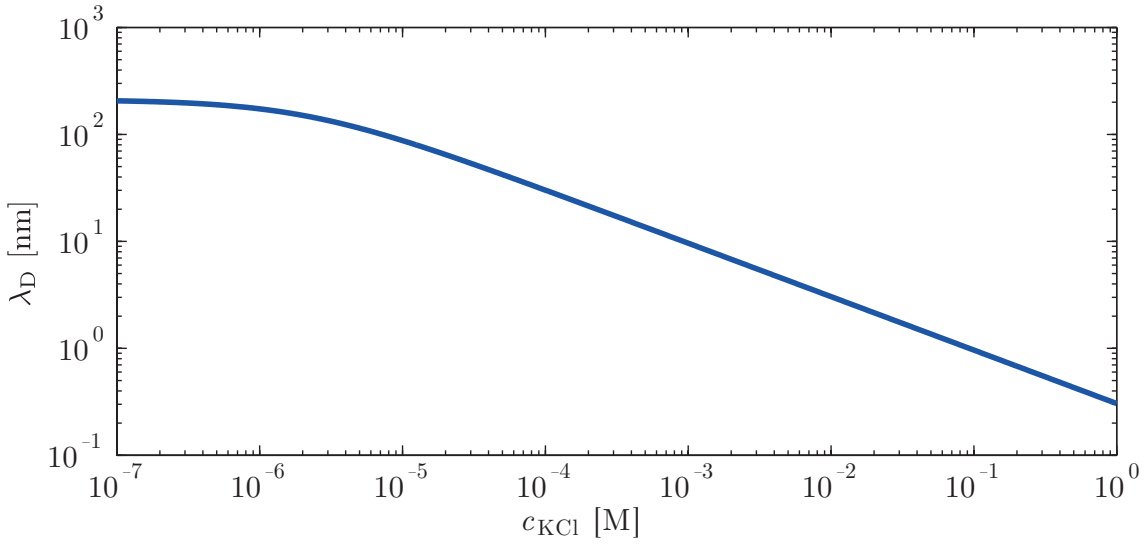

Figure A.8: A log-log plot of the Debye length versus KCl bulk concentration. 11.8×10^{-2} µM CO_2 is added to the KCl solution so pH = 5.68.

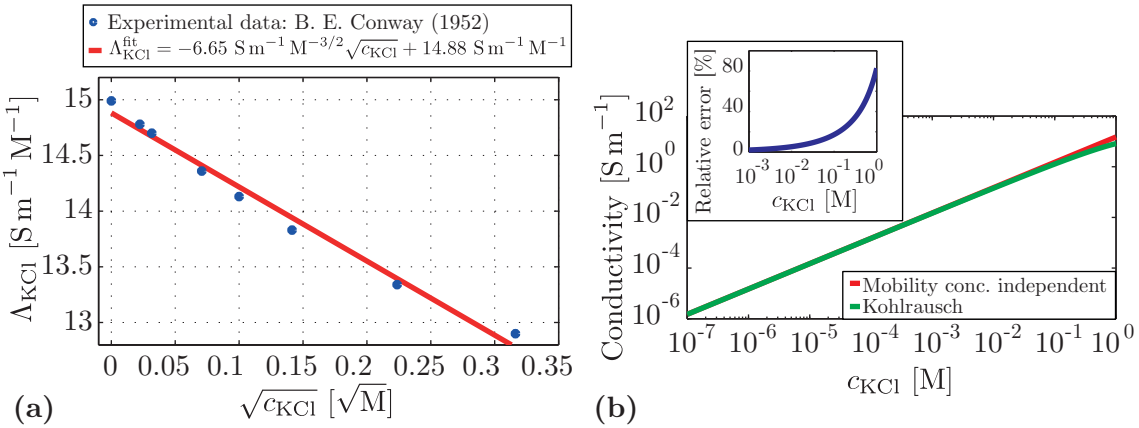

Figure A.9: **(a)** the equivalent conductivity of KCl Λ_{KCl} plotted versus $\sqrt{c_{\text{KCl}}}$ together with a linear fit of the Kohlrausch law Eq. (A.69). The correlation coefficient of the fit R^2 is 0.993. Experimental data is from Table A.1. **(b)** a log-log plot of the Kohlrausch conductivity Eq. (A.70) plotted versus KCl concentration together with the conductivity assuming the ionic mobilities to be independent of ionic strength. The relative error between the two conductivities versus KCl concentration is shown in the inset. The mobilities are found in Table B.2 in Appendix B, $\Lambda_{\text{o}} = 14.88\,\text{S m}^{-1}\,\text{M}^{-1}$, and $k_{\text{K}} = 6.65\,\text{S m}^{-1}\,\text{M}^{-3/2}$.

A.8 The Kohlrausch Law

The mobility of ions in a solution depends on the ionic strength of the solution. For high ionic strengths the ions will be surrounded by screening clouds of counterions of thickness λ_{D}. When the ions move these screening clouds exert drag forces on the ions. Furthermore, the screening cloud of counterions around each ion will be polarized due to the external electric field reducing the local electric field experienced by the ion [26]. Therefore, the mobility is reduced for high ionic strengths.

For an electrolyte define the equivalent conductivity as [27]

$$\Lambda \equiv \frac{\sigma}{c}, \tag{A.68}$$

where σ is its conductivity and c its concentration. The Kohlrausch law states

$$\Lambda = \Lambda_{\text{o}} - k_{\text{K}}\sqrt{c}, \tag{A.69}$$

where Λ_{o} is the equivalent conductivity at infinite dilution and k_{K} is the Kohlrausch coefficient. For low electrolyte concentrations $\Lambda \approx \Lambda_{\text{o}}$ and the conductivity scales as $\sigma = \Lambda_{\text{o}} c$. From the Kohlrausch law the conductivity of an electrolyte is

$$\sigma = \Lambda_{\text{o}} c - k_{\text{K}} c^{3/2}. \tag{A.70}$$

We will determine Λ_{o} and k_{K} for a KCl solution. Experimental data from Ref. [28] giving the equivalent conductivity of KCl for various KCl concentrations is given in Table A.1.

The Kohlrausch law has been fitted to the experimental data in Fig. A.9(a). For KCl we find that $\Lambda_o = 14.88\,\mathrm{S\,m^{-1}\,M^{-1}}$ and $k_K = 6.65\,\mathrm{S\,m^{-1}\,M^{-3/2}}$. Using these values the predicted Kohlrausch conductivity for KCl is plotted versus KCl concentration in Fig. A.9(b) together with the uncorrected conductivities calculated from the mobilities of K^+ and Cl^- in Table B.2 in Appendix B. The relative error between the two conductivities is seen in the inset of Fig. A.9(b). At KCl concentrations of 100 mM, 10 mM, and 1.0 mM the relative errors between uncorrected and corrected conductivities are 17%, 5.4%, and 2.1%, respectively.

c_{KCl} [M]	0	0.0005	0.001	0.005	0.01	0.02	0.05	0.1
Λ_{KCl} [S m^{-1} M^{-1}]	14.99	14.78	14.70	14.36	14.13	13.83	13.34	12.90

Table A.1: The equivalent conductivity of KCl for different KCl concentrations. The data is from Ref. [28].

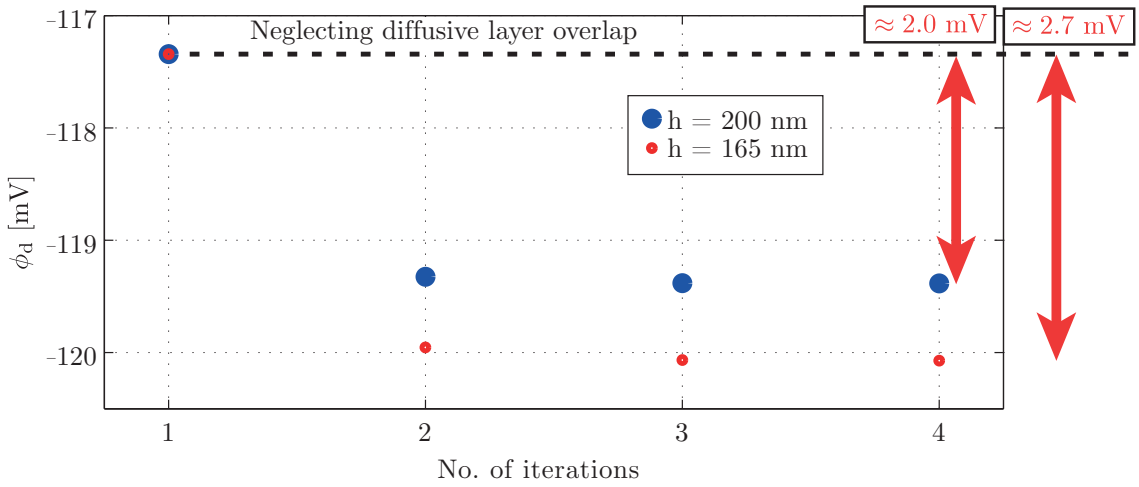

Figure A.10: ϕ_d plotted versus number of iterations for two different nanochannel heights h. The nanochannel contains deionized water with absorbed CO_2. Model parameters are found in Table B.3 in Appendix B except pK_- which is 6.64 confer Table 3.3.

A.9 Surface Charge Density Dependence on Diffusive Layer Overlap

When calculating the surface charge density in the diffusive layer δ_d for the 2pK-model in Section 3.3 and the metal adsorption model in Section 3.4 the electric potential in the center of the channel ϕ_m was assumed zero confer Eq. (2.28). In other words we assume no diffuse layer overlap equivalent to assuming $\lambda_D \ll h$ but this assumption will generally not hold for nanochannels containing a solution of very low bulk concentrations[4] ($\lesssim$ 0.1 mM).

In order to solve the models taking into account diffusive layer overlap the surface charge density in Eq. (2.28) of the silica surface must be replaced by the more general expression Eq. (2.27), i.e.

$$\delta_d = -\mathrm{sgn}\left(\phi_d\right)\left\{2\epsilon k_B T \sum_i^{\mathcal{N}} c_i^b \left[\exp\left(-\frac{Z_i e}{k_B T}\phi_d\right) - \exp\left(-\frac{Z_i e}{k_B T}\phi_m\right)\right]\right\}^{\frac{1}{2}}. \tag{A.71}$$

It is seen that the surface charge density in the diffusive layer δ_d changes with ϕ_m. The implementation of the diffusive layer overlap is identical for both models so we will here only describe how to implement it in the 2pK-model. We incorporate the calculation of ϕ_m self-consistently in our way of solving the ϕ_d potential. The implementation is inspired by Ref. [16] and described in the following procedure

1) Assume $\phi_m = 0$ and solve Eq. (3.26) for ϕ_d

[4] A 0.1 mM KCl solution has a Debye length of about 30 nm. For deionized water with absorbed CO_2 $\lambda_D \sim 211$ nm (pH = 5.68). Without absorbed CO_2 $\lambda_D \sim 963$ nm (pH = 7.00).

2) Solve the potential profile and determine ϕ_m, confer Appendix A.6

3) Eqs. (3.26b) and (3.26c) are solved for ϕ_d using Eq. (A.71) with ϕ_m from step 2

4) Steps 2 and 3 are repeated until ϕ_m converges[5]

ϕ_m depends on the channel height which leads to a channel height dependent δ_d potential. The electric potential ϕ_d is plotted in Fig. A.10 versus the number of iterations for two different channel heights h. The channel contains deionized water with absorbed CO_2. The dependence of ϕ_d on channel height is observed in the figure. In iteration step 1 the mid potential is assumed zero for both heights so the potentials are expected to coincide which is verified in the figure but for the following iterations the potentials deviate from each other since the mid potential ϕ_m depends on height. We observe that the changes in ϕ_d due to the non-zero mid potential ϕ_m are about -2.0 mV and -2.7 mV for the 200 nm and 165 nm high channel, respectively. As expected, the change in the ϕ_d potential is greatest for the channel of smallest height where the diffusive layer overlap is greatest.

[5] ϕ_m has converged when the absolute relative difference between the new value and the previous is below a specified threshold value. We use a threshold value of 10^{-4}.

A.10 Features of the Conductance Calculation

In this section we investigate how the conductance curve in Fig. 4.2 changes when we leave out a features of the system while keeping the rest. The features we choose to leave out of the model one by one are

1 CO_2 absorption

2 Diffusive layer overlap i.e. a non-zero ϕ_m

3 Advection conductance contribution

4 The immobile layer

1 Leaving out CO_2 Absorption

Leaving out the absorption of CO_2 brings the pH of the KCl solution to 7 instead of 5.68 and slightly modifies the ionic strength. The result is the blue curve in Fig. A.11. Without absorbed CO_2 the valley moves toward lower concentrations. The conductance curve is generally higher than when taking into account absorbed CO_2 which can be explained by the reduced ionic strength increasing the Debye length and hence the concentration elevation throughout the channel. Furthermore, fewer ions are present in the channel to screen the wall so size of the ζ potential increases elevating more counterions and thereby increases the conductance. The reason why the valley moves toward lower concentrations is that fewer hydrons are present so the KCl bulk concentration has to decrease even more before the hydrons begin to dominate as compared to a channel with a large hydron bulk concentration.

2 Neglecting Diffusive Layer Overlap

We neglect the diffusive layer overlap when calculating the surface charge density confer Appendix A.9 by assuming that the mid potential ϕ_m is zero. The result is the green dashed curve in Fig. A.11 on top of the full black curve. From Fig. A.10 we estimate that for a 200 nm high channel at infinite dilution (no KCl salt) the change in ϕ_d by accounting for diffusive layer overlap is less than 2%. We see that this is not enough to affect the conductance curve.

3 Leaving out the Advection Conductance Contribution

Since the advection conductance is a positive addition to the total conductance we expect a general decrease in conductance when leaving out this contribution. This is also seen to be the case in Fig. A.11 where the conductance without advection contribution (red curve) is below the full calculation (black curve).

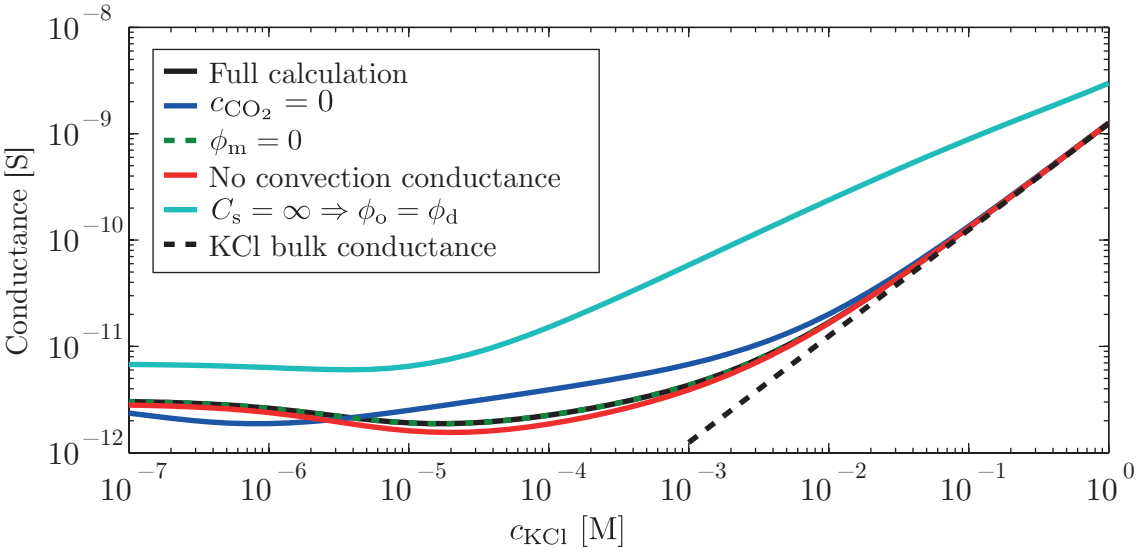

Figure A.11: A log-log plot of channel conductance versus KCl bulk concentration with the KCl bulk conductance (black dashed line) when taking out different model features: all features (black full curve), no absorbed CO_2 (blue curve), assuming zero mid potential (green dashed curve), no advection conductance (red curve), no immobile layer (light blue curve). The mobilities and model parameters can be seen in Table B.2 and Table B.3, respectively, in Appendix B. The channel has height 200 nm.

4 Removing the Immobile Layer

We remove the immobile layer by letting the Stern capacitance C_s become infinite. The effect on the conductance curve can be seen in Fig. A.11. Removing the immobile layer increases the size of ϕ_d to the size of ϕ_o and the 2pK-model changes from being based on the Gouy–Chapman–Stern picture to the Gouy–Chapman picture confer the models in Fig. 1.1. The conductance is increased considerably over the entire concentration range and it moves the bulk regime to higher KCl bulk concentrations. The reason is that the higher ϕ_d value increases the elevation of counterions which increases the conductance. We note that at high concentrations the Debye length is very small compared to the height but the large potential is still able to elevate the counterion concentrations in the thin diffusive layers enough for them to dominate the conductance over the bulk region in the channel. Recall that the Stern capacitance was originally introduced because the models predicted too large ζ potentials when compared to experiments [9].

Summary

The absorbed CO_2 and the Stern capacitance C_s are the most important features when calculating the conductance for various KCl bulk concentrations.

A.11 Surface Site Coverages with Aminosilane Coating

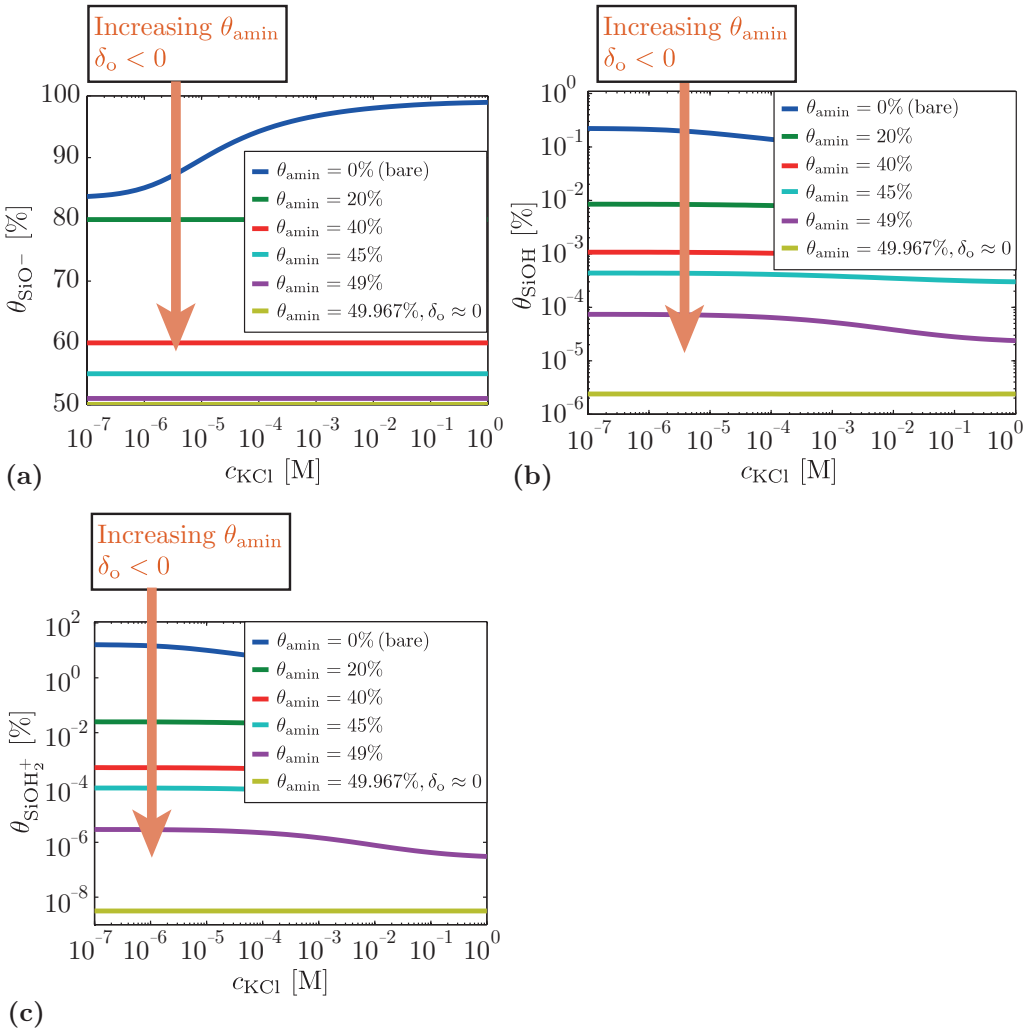

Figure A.12: Site coverages versus KCl bulk concentration for different values of aminosilane coverage. The mobilities and model parameters can be seen in Table B.2 and Table B.3, respectively, in Appendix B. The channel height is 200 nm. **(a)** a lin-log plot of SiO^- site coverage. **(b)** a log-log plot of SiOH site coverage. **(c)** a log-log plot of $SiOH_2^+$ site coverage.

Appendix B

Various Tables

B.1 Nature Constants

e [C]	ϵ_0 [F m^{-1}]	$\epsilon_\mathrm{r}^\mathrm{water}$ [29]	$k_\mathrm{B}T$ [J]	N_A [mol^{-1}]	F [C mol^{-1}]	K_w [M^2]	η [Pa s]
1.602×10^{-19}	8.85×10^{-12}	78	0.0259 e	6.022×10^{23}	9.65×10^4	10^{-14}	1.0×10^3

Table B.1: Nature constants. From left to right: elementary charge, permittivity of vacuum, relative permittivity of water ($T = 25$℃), thermal energy ($T = 25$℃), Avogadro's number, Faraday's constant, self-ionization constant of water, and viscosity of water ($T = 20$℃).

B.2 Ion Mobilities

	H^+ [30]	OH^- [30]	K^+ [30]	Cl^- [30]	HCO_3^- [6]	CO_3^{2-} [6]
Mobility [m^2 V^{-1} s^{-1}]	3.62×10^{-7}	2.05×10^{-7}	7.62×10^{-8}	7.91×10^{-8}	4.61×10^{-8}	7.18×10^{-8}

Table B.2: Ion mobilities at $T = 25$℃. From left to right: hydron, hydroxide ion, potassium ion, chloride ion, bicarbonate ion, and carbonate ion.

B.3 Parameters for Conductance Calculation Using the 2pK-model

w [m]	L [m]	Γ_{tot} [sites nm^{-2}]	pK_- [M]	pK_+ [M]	$c_{\mathrm{H_2CO_3}}$ [M]	C_{s} [F m^{-2}]
5×10^{-6}	1.2×10^{-2}	5	2.8	-1.64	1.18×10^{-5}	0.2

Table B.3: Channel parameters for the 2pK-model: channel width, channel length, total number of chargeable sites, logarithmic surface dissociation constants related to the negative SiO^- sites and positive $SiOH_2^+$ sites, respectively, formal concentration of H_2CO_3, and Stern capacitance.

B.4 Input/Output Parameters for the Metal Adsorption Model

Input		Output	
Lab input		Parameter	Symbol
Parameter	Symbol	Potentials	(ϕ_{o}, ϕ_{β}, ϕ_{d})
Channel geometry (height, width, length)	(h, w, L)	(o-plane, β-plane, d-plane)	
Temperature	T	Surface charge densities	(δ_{o}, δ_{β}, δ_{d})
Formal concentrations of all species	c_{formal}	(o-plane, β-plane, d-plane)	
Literature Input		Actual concentrations	c_{actual}
Parameter	Symbol	of all species	
pK_{a} for the silica channel wall reaction: $SiOH \rightleftharpoons SiO^- + H^+$	pK_-	Transverse concentration profile for the ith ion	$c_i(z)$
pK_{a} for the silica channel wall reaction: $SiOH_2^+ \rightleftharpoons SiOH + H^+$	pK_+	Silica surface point of zero charge	PZC
Stern capacitances (inner, outer)	(C_1, C_2)	Bulk solution acidity	pH_{b}
Total number of chargeable sites SiOH	Γ_{tot}	Debye length	λ_{D}
Charge states for all species in the bulk	-	Transverse potential profile	$\phi(z)$
Dissociation constant for all bulk reactions	pK_{a}		
pK_{a} for the silica channel wall reaction: $SiOM \rightleftharpoons SiO^- + M^+$	pK_{M}		

Table B.4: Input/output parameters for the metal adsorption model. The inputs are divided into values obtained from laboratory measurements (lab input) and values obtained from the literature (literature input).

B.5 Experimental Data

In this section we provide the experimental conductance data used in this thesis. The data is recorded in the Pennathur Laboratory at the University of California, Santa Barbara in the fall 2009 and the spring 2010. The data sets of experimentalist David A. Herrick can be seen in Tables B.5 and B.6. The data sets of experimentalist Andrew Crumrine are in Tables B.7–B.9

David A. Herrick - data set 1 - UCSB Nanolab				
Concentration [mM]	Voltage [V]	Current [A]	Conductance [S]	Mean [S]/Std. dev. [S]
100	100	1.72×10^{-8}	1.72×10^{-10}	$1.67 \times 10^{-10}/3.25 \times 10^{-12}$
	200	3.39×10^{-8}	1.70×10^{-10}	
	300	4.98×10^{-8}	1.66×10^{-10}	
	400	6.60×10^{-8}	1.65×10^{-10}	
	500	8.24×10^{-8}	1.65×10^{-10}	
10	100	1.49×10^{-9}	1.49×10^{-11}	$1.66 \times 10^{-11}/9.89 \times 10^{-13}$
	200	3.32×10^{-9}	1.66×10^{-11}	
	300	5.20×10^{-9}	1.73×10^{-11}	
	400	6.79×10^{-9}	1.70×10^{-11}	
	500	8.63×10^{-9}	1.73×10^{-11}	
1	100	3.72×10^{-10}	3.72×10^{-12}	$4.24 \times 10^{-12}/3.02 \times 10^{-13}$
	200	8.65×10^{-10}	4.33×10^{-12}	
	300	1.29×10^{-9}	4.29×10^{-12}	
	400	1.75×10^{-9}	4.37×10^{-12}	
	500	2.25×10^{-9}	4.50×10^{-12}	
0.5	100	1.80×10^{-10}	1.80×10^{-12}	$2.78 \times 10^{-12}/5.95 \times 10^{-13}$
	200	5.41×10^{-10}	2.71×10^{-12}	
	300	8.85×10^{-10}	2.95×10^{-12}	
	400	1.26×10^{-9}	3.16×10^{-12}	
	500	1.65×10^{-9}	3.31×10^{-12}	
0.1	100 (*)			$2.69 \times 10^{-12}/3.75 \times 10^{-13}$
	200	4.39×10^{-10}	2.20×10^{-12}	
	300	7.86×10^{-10}	2.62×10^{-12}	
	400	1.15×10^{-9}	2.88×10^{-12}	
	500	1.53×10^{-9}	3.06×10^{-12}	
0.05	100	1.85×10^{-10}	1.85×10^{-12}	$2.79 \times 10^{-12}/5.79 \times 10^{-13}$
	200	5.35×10^{-10}	2.68×10^{-12}	
	300	8.91×10^{-10}	2.97×10^{-12}	
	400	1.26×10^{-9}	3.16×10^{-12}	
	500	1.66×10^{-9}	3.32×10^{-12}	
0.01	100 (*)			$2.44 \times 10^{-12}/3.34 \times 10^{-13}$
	200	3.96×10^{-10}	1.98×10^{-12}	
	300	7.23×10^{-10}	2.41×10^{-12}	
	400	1.07×10^{-9}	2.68×10^{-12}	
	500	1.35×10^{-9}	2.70×10^{-12}	

Table B.5: Experimental data set 1 from David A. Herrick. First column shows the concentrations, second column the source voltage, third column the current for each voltage step, fourth column the conductance for each voltage, and the fifth column shows the mean conductance and standard deviation for the concentration. (*): data point excluded by experimentalist.

David A. Herrick - data set 2 - UCSB Nanolab				
Concentration [mM]	Voltage [V]	Current [A]	Conductance [S]	Mean [S]/Std. dev. [S]
500	100 (*)			$7.10 \times 10^{-10}/3.38 \times 10^{-10}$
	200	1.34×10^{-7}	3.21×10^{-10}	
	300	2.00×10^{-7}	5.73×10^{-10}	
	400	2.65×10^{-7}	8.44×10^{-10}	
	500	3.27×10^{-7}	1.10×10^{-9}	
0.1	100 (*)			$1.96 \times 10^{-12}/2.66 \times 10^{-13}$
	200	3.21×10^{-10}	1.61×10^{-12}	
	300	5.73×10^{-10}	1.91×10^{-12}	
	400	8.44×10^{-10}	2.11×10^{-12}	
	500	1.10×10^{-9}	2.21×10^{-12}	
0.05	100 (*)			$2.07 \times 10^{-12}/2.59 \times 10^{-13}$
	200	3.44×10^{-10}	1.72×10^{-12}	
	300	6.09×10^{-10}	2.03×10^{-12}	
	400	8.76×10^{-10}	2.19×10^{-12}	
	500	1.16×10^{-9}	2.32×10^{-12}	
0.01	100 (*)			$2.12 \times 10^{-12}/2.94 \times 10^{-13}$
	200	3.47×10^{-10}	1.74×10^{-12}	
	300	6.14×10^{-10}	2.05×10^{-12}	
	400	9.16×10^{-10}	2.29×10^{-12}	
	500	1.20×10^{-9}	2.40×10^{-12}	

Table B.6: Experimental data set 2 from David A. Herrick. First column shows the concentrations, second column the source voltage, third column the current for each voltage step, fourth column the conductance for each voltage, and the fifth column shows the mean conductance and standard deviation for the concentration. (*): data point excluded by experimentalist.

Andrew Crumrine - data set 1 - UCSB Nanolab				
Conc. [mM]	Trial	Avg. cond. [S]	Std. dev. [S]	Overall cond./Std. dev. [S]
100	1	1.70×10^{-10}	6.50×10^{-12}	$1.62 \times 10^{-10}/1.13 \times 10^{-11}$
	2	1.54×10^{-10}	9.86×10^{-12}	
10	1	1.96×10^{-11}	6.28×10^{-14}	$2.02 \times 10^{-11}/5.21 \times 10^{-13}$
	2	2.05×10^{-11}	1.25×10^{-13}	
	3	2.05×10^{-11}	1.31×10^{-12}	
1	1-7 (*)			$1.46 \times 10^{-12}/2.29 \times 10^{-13}$
	8	1.26×10^{-12}	2.45×10^{-13}	
	9	1.48×10^{-12}	2.50×10^{-13}	
	10	1.40×10^{-12}	3.77×10^{-13}	
	11	1.84×10^{-12}	2.56×10^{-13}	
	12	1.33×10^{-12}	2.78×10^{-13}	
0.5	1-4 (*)			$1.54 \times 10^{-12}/1.54 \times 10^{-13}$
	5	1.71×10^{-12}	3.20×10^{-13}	
	6	1.40×10^{-12}	1.69×10^{-13}	
	7	1.51×10^{-12}	1.11×10^{-13}	
0.1	1	4.38×10^{-13}	8.18×10^{-14}	$4.93 \times 10^{-13}/5.08 \times 10^{-14}$
	2	5.03×10^{-13}	8.04×10^{-15}	
	3	5.38×10^{-13}	7.69×10^{-15}	

Table B.7: Experimental data set 1 from Andrew Crumrine. First column shows the concentrations, second column the trial number, third column the average conductance for each trial, fourth column the standard deviation on each average conductance, and the fifth column shows the overall conductance and standard deviation for the concentration. (*): data point excluded by experimentalist.

Andrew Crumrine - data set 2 (0.1 mM HCl added) - UCSB Nanolab [Table 1/2]				
Conc. [mM]	Trial	Avg. cond. [S]	Std. dev. [S]	Overall cond./Std. dev. [S]
100	1 (*)			$1.50 \times 10^{-10}/2.65 \times 10^{-12}$
	2	1.51×10^{-10}	9.53×10^{-12}	
	3	1.54×10^{-10}	4.31×10^{-12}	
	4	1.49×10^{-10}	1.21×10^{-12}	
	5	1.51×10^{-10}	2.31×10^{-12}	
	6	1.47×10^{-10}	1.02×10^{-12}	
50	1 (*)			$7.15 \times 10^{-11}/3.23 \times 10^{-12}$
	2	6.69×10^{-11}	2.24×10^{-12}	
	3	7.09×10^{-11}	4.00×10^{-13}	
	4	7.53×10^{-11}	4.24×10^{-12}	
	5	7.39×10^{-11}	5.52×10^{-12}	
	6	7.07×10^{-11}	2.69×10^{-12}	
10	1 (*)			$1.67 \times 10^{-11}/2.19 \times 10^{-13}$
	2	1.64×10^{-11}	4.24×10^{-13}	
	3	1.65×10^{-11}	5.59×10^{-13}	
	4	1.69×10^{-11}	5.16×10^{-13}	
	5	1.67×10^{-11}	7.73×10^{-13}	
	6	1.69×10^{-11}	5.32×10^{-13}	
5	1 (*)			$7.81 \times 10^{-12}/3.02 \times 10^{-13}$
	2	8.16×10^{-12}	1.07×10^{-13}	
	3	7.52×10^{-12}	1.58×10^{-13}	
	4	8.03×10^{-12}	1.18×10^{-13}	
	5	7.49×10^{-12}	3.22×10^{-13}	
	6	7.88×10^{-12}	1.52×10^{-13}	
1	1	1.33×10^{-12}	2.45×10^{-14}	$1.42 \times 10^{-12}/9.45 \times 10^{-14}$
	2	1.35×10^{-12}	5.27×10^{-14}	
	3	1.34×10^{-12}	1.10×10^{-13}	
	4	1.48×10^{-12}	3.44×10^{-14}	
	5	1.50×10^{-12}	3.87×10^{-14}	
	6	1.54×10^{-12}	3.94×10^{-14}	

Table B.8: [Table 1/2] Experimental data set 2 from Andrew Crumrine. First column shows the concentrations, second column the trial number, third column the average conductance for each trial, fourth column the standard deviation on each average conductance, and the fifth column shows the overall conductance and standard deviation for the concentration. (*): data point excluded by experimentalist.

Andrew Crumrine - data set 2 (0.1 mM HCl added) - UCSB Nanolab [Table 2/2]				
Conc. [mM]	Trial	Avg. cond. [S]	Std. dev. [S]	Overall cond./Std. dev. [S]
0.5	1	9.06×10^{-13}	9.56×10^{-14}	$8.90 \times 10^{-13}/1.44 \times 10^{-14}$
	2	8.88×10^{-13}	1.28×10^{-14}	
	3	8.37×10^{-13}	4.25×10^{-14}	
	4	8.71×10^{-13}	2.55×10^{-14}	
	5	8.93×10^{-13}	3.06×10^{-14}	
	6	9.70×10^{-13}	5.40×10^{-14}	
0.1	1 (*)			$5.09 \times 10^{-13}/1.67 \times 10^{-13}$
	2	5.38×10^{-13}	1.04×10^{-14}	
	3	5.48×10^{-13}	8.65×10^{-15}	
	4	5.36×10^{-13}	1.01×10^{-14}	
	5	5.57×10^{-13}	8.50×10^{-15}	
	6	5.61×10^{-13}	6.42×10^{-15}	
	7	5.58×10^{-13}	7.16×10^{-15}	
	8	5.63×10^{-13}	6.07×10^{-15}	
	9	5.72×10^{-13}	1.04×10^{-14}	
	10	5.74×10^{-13}	9.90×10^{-15}	
	11	5.69×10^{-13}	8.17×10^{-15}	
	12	5.74×10^{-13}	8.67×10^{-15}	
0.05	1-2 (*)			$6.35 \times 10^{-13}/7.53 \times 10^{-15}$
	3	6.23×10^{-13}	5.66×10^{-15}	
	4 (*)			
	5	6.37×10^{-13}	6.00×10^{-15}	
	6	6.35×10^{-13}	1.46×10^{-15}	
	7	6.36×10^{-13}	4.34×10^{-15}	
	8	6.44×10^{-13}	5.25×10^{-15}	
0.02	1	6.07×10^{-13}	9.70×10^{-15}	$6.10 \times 10^{-13}/8.95 \times 10^{-15}$
	2	6.00×10^{-13}	2.74×10^{-14}	
	3	6.20×10^{-13}	1.20×10^{-14}	
	4	6.07×10^{-13}	2.49×10^{-14}	
	5-6 (*)			
	7	6.21×10^{-13}	2.92×10^{-14}	
	8	6.02×10^{-13}	2.28×10^{-14}	

Table B.9: [Table 2/2] Experimental data set 2 from Andrew Crumrine. (*): data point excluded by experimentalist.

Appendix C

MatLab Scripts

C.1 The Modified Santiago Script

```
function [pHb,zMat,cizMat] = Santiago(INP,cTot,Kw)
% The modified Santiago Script calculates the bulk pH and analytical
% concentration of each specie in the solution.
% Input: Matrix containing the pKa value and valence of each
%        possible valence state of the specie to be created in the solution,
%        vector containing the formal concentration of each added specie,
%        and the dissociation constant for water.
% Output: The bulk pH in the reservoir, a matrix containing all valence
%         states of the species, and a matrix containing all
%         analytical concentrations of the species.

Nspecies=size(INP,1); %Number of species added.
% PREPARE L Matrix
%--------------------
% Calculate the number of columns required for the matrix.
% this is determined by the maximum value of (p_i - n_i) for all species
% p_i - n_i = difference between most positive and most negative valence.
MaxCol=-Inf;
for j=1:size(INP,1)
    MaxCol=max([MaxCol,max(INP{j}(1:2:end))-min(INP{j}(1:2:end))+1]);
end

% Initialize matrices to zero
LMat=zeros(size(INP,1),MaxCol);
KaMat=LMat;

% Loop on species
for j=1:Nspecies
    zList=INP{j}(1:2:end);                  % Get list of valences
    pKaList=INP{j}(2:2:end);                % Get list of pKa
    KaList=10.^(-pKaList);                  % Create list of Ka
% Sort the valence in increasing order, and get indices
    [zList,Index]=sort(zList);
```

```
%Use indices to sort the other list in a consistent order
    KaList=KaList(Index);


% Find indices where the valence value is +1 and -1
% (at least one of these valences must always for any species used):
    Ip1=find(zList==1);     Im1=find(zList==-1);
% Add the neutral state to the list of valence, between negative
% and positive values
    zList  = [zList(1:Im1),0,zList(Ip1:end)];
% 1 added to the list of Ka values for math reasons
% (see formulation for 'L' matrix)
    KaList = [KaList(1:Im1),1,KaList(Ip1:end)];
% Put all lists into corresponding matrices.
    zMat(j,1:length(zList))=zList;
    KaMat(j,1:length(KaList))=zList;

    zListArranged{j}=zList;
    % Get minimum and maximum valences for this species
    % and construct the matrix L

    nj=min(zList);    pj=max(zList);
    for z=zList
        if z<0
            LMat(j,z-nj+1)=prod(KaList(z-nj+1:-nj));
        elseif z>0
            LMat(j,z-nj+1)=1/prod(KaList(-nj+2:z-nj+1));
        elseif z==0
            LMat(j,z-nj+1)=1;
        end %if
    end % for z

end %for ij

% CONSTRUCT POLYNOMIALS
%----------------------
% Construct the polynomial Q by multiplying all the polynomials in the
% matrix L (all rows). Multiplying polynomials is equivalent to convolving
% their vectors of coefficients
Q1=1;
for j=1:size(LMat,1)
    Q1=conv(Q1,LMat(j,:));
end %for j
Q2=[-Kw 0 1];
Q=conv(Q1,Q2);

% Construct the polynomials Pi
% Loop on all species
for i=1:Nspecies
    LMatMod=LMat;   % Defined Modified L Matrix, initially identical
                    % to L Matrix
    LMatMod(i,:)=LMat(i,:).*zMat(i,:);         % Modify just the row i

    % convolve all rows in the LMatMod to construct the polynomial
```

```
88      Pi=1;
89      for kl=1:size(LMatMod,1)
90          Pi=conv(Pi,LMatMod(kl,:));
91      end %for j
92      Pi=conv([0 1],Pi);
93      PMat(i,:)=Pi;   % Insert all polynomials Pi as rows in the matrix PMat
94  end %for i
95
96  % All the enries in each row are identical and equal to the total
97  % concentration of that specie:
98  cTotMat=repmat(cTot',1,size(PMat,2));
99  P=sum(cTotMat.*PMat,1);  % The polynomial P is the sum of c_i * P_i
100
101 % Construct the final polynomial as the sum of P and Q
102 Poly=PolSum(P,Q);
103 roo=roots(fliplr(Poly));        % Find all roots of the polynomial
104 roo=roo(imag(roo)==0);          % Eliminate complex solutions
105 cH=roo(roo>0);                  % Choose the positive solution.
106                                 % Note that cH is in mol/lit
107
108 pHb = -log10(cH);               %pH in bulk.
109
110 PolDeg=size(LMat,2);                                % Polynomial degree
111 % Create vector of cH Powers (cH^0, cH^1, ... , cH^(PolDeg-1)):
112 cHPolVec=[1;cumprod(ones(PolDeg-1,1)*cH,1)];
113 % Replicate powers vector to create matrix:
114 cHMatPower=repmat(cHPolVec',[Nspecies,1]);
115 % Temporarty matrix (see formulation for c_i_z):
116 M1Mat=repmat(cTot'./(LMat*cHPolVec),[1,PolDeg]);
117 % Calculate concentration of each ionic state (valence) of each species:
118 cizMat=LMat.*cHMatPower.*M1Mat;
119
120 % Sum arbitrary length polynomials:
121 function out=PolSum(P1,P2)
122 % This essentially pads the shorter vecotr with zeros, and then sums the
123 % two vectors
124 % get the length of the largest polynomial
125 Psize=max(length(P1),length(P2));
126 % Set temporary vectors of size Psize to zero.
127 P1out=zeros(1,Psize); P2out=P1out;
128 P1out(1:length(P1))=P1;             % Inject P1 values into temporar vector
129 P2out(1:length(P2))=P2;             % Inject P2 values into temporar vector
130 out=P1out+P2out;                    % sum both vectors
```

C.2 MatLab Script for Solving the Poisson–Boltzmann Equation

```
function [zpos,phi] = potential2ndOrderSolverBVP4C(zetap,pHb,zMat,cizMat,...
h,lD,IS,constant)
% Solves the Poison-Boltzman Eq. in a infinite parallel-plate channel
% in the region from the wall z = 0 to mid channel z = h/2.
% Input: The zeta potential, the bulk pH, ionic valence matrix, bulk conc.
%        matrix, channel height, Debye length, ionic strength
%        vector of constants
% Output: zpos - grid positions
%         phi - the electrical potential and it's derivative
el = constant(2); % Elementary charge (coulomb)
kT = constant(3); % Thermal energy (J)
BulkParam = [pHb , IS];

zpos = [0,logspace(-15,log10(h/2),2e3)]*1/lD;   % Exponential distributed
                                                % mesh grid
%zpos = linspace(0,h/2,1e3);                    % Evenly distributed
                                                % mesh grid

solinit = bvpinit(zpos,[zetap/(kT/el) 0]); % Initial mesh

options = bvpset('RelTol',1e-7,'AbsTol',1e-7); % Tolerance options

phi = bvp4c(@potential2ndOrder,@potential2ndOrderBC,solinit,options,...
            zetap,BulkParam,zMat,cizMat,constant);

function dphi = potential2ndOrder(z,phi,zetap,BulkParam,zMat,cizMat,...
                                  constant)
% The Poison-Boltzman Eq.
NA = constant(5);      % Avogadro's number (particles/mol)
pHb = BulkParam(1);    % Bulk pH
IS =  BulkParam(2);    % Ionic strength (m^-3)

cHb = 10^(-pHb)*1e3*NA;          % Hydron conc. (H+) (m^-3)
cOHb = 10^(-14+pHb)*1e3*NA;      % Hydroxide (OH-) conc. (m^-3)
cizMat = cizMat*1e3*NA;          % Bulk conc. of species (m^-3)

B = sum(sum(zMat.*cizMat.*exp(-zMat*phi(1)) ));
B = B + (1)*cHb*exp(-(1)*phi(1)) + (-1)*cOHb*exp(-(-1)*phi(1));
% 1st oder ODE system (normalized)
dphi = [phi(2),
         -B/(2*IS)];

function BV = potential2ndOrderBC(phia,phib,zetap,BulkParam,zMat,cizMat,...
                                  constant)
el = constant(2); % Elementary charge (coulomb)
kT = constant(3); % Thermal energy (J)
BV = [phia(1)-zetap/(kT/el),phib(2)]; % Boundary condition:
                                      % @ wall, phi = zeta
```

```
49                                                  % @ mid channel, dphi/dz = 0
```

C.3 MatLab Script for the 2pK-Model

```
1  function [sol2,delta0] = Find_zeta_2pKmodel(x01,phiMidChan,cizMat,zMat,...
2      pHb,constant)
3  % Calculates the zeta potential in the channel by using fsolve
4  % Input: Start guess on the zeta-potential, mid potential,
5  %             bulk conc. of species,ionic valence of species
6  %            bulk pH, constants.
7  options = optimset('Display','iter','TolFun',eps,'TolX',eps,...
8            'MaxFunEvals',1e25,'MaxIter',1e3,'Diagnostics','off',...
9            'LevenbergMarquardt','on','LargeScale','off');
10
11 sol2 = fzero(@(x01)Model2pK(x01,phiMidChan,zMat,cizMat,pHb,...
12     constant),x01,options);
13
14 %% Find surface charge:
15 phid = sol2;
16 epsl = constant(1);     % Permittivity for water. (F/m)
17 el = constant(2);       % Elementary charge (coulomb)
18 kT = constant(3);       % Thermal energy (J)
19 GamTot = constant(4);   % Total number of chargeable sites (m^-2)
20 NA = constant(5);       % Avogadro's number (particles/mol)
21 Kpl = constant(6);      % Equilibrium constant
22                         % for SiOH2+<-> SiOH + H+ (Molar)
23 Kmi = constant(7);      % Equilibrium constant for
24                         % SiOH <-> SiO- + H+ (Molar)
25 CTot = constant(11);    % Stern capacitance (F/m^2)
26 thetaAS = constant(16); % Amino silane coverage
27
28 cHb = 10^(-pHb)*1e3*NA;     % Bulk concentration of H+ (m^-3)
29 cOHb = 10^(-14+pHb)*1e3*NA; % Bulk concentration of OH- (m^-3)
30 cizMat = cizMat*1e3*NA;     % Concentration of electrolytes (m^-3)
31
32 C = exp(-zMat*el/kT*phiMidChan); % Constant for non zero mid potential.
33 % Contribution of electrolytes to the sum in delta0:
34 B = sum(sum( cizMat.*(exp(-zMat*el/kT*phid)-C) ));
35 % Add contribution of H+ and OH- to the sum in delta0:
36 B = B + cHb*(exp(-(1)*el/kT*phid)-exp(-(1)*el/kT*phiMidChan))...
37     +cOHb*(exp(-(-1)*el/kT*phid)-exp(-(-1)*el/kT*phiMidChan));
38 % Surface charge density in 0-plane:
39 delta0 = sign(phid)*sqrt(2*epsl*kT)*(B)^(1/2);
40 %%
41 phi0 = phid + delta0/CTot; % Stern capacitance relation
42 cHb = cHb/(1e3*NA); % -> (Molar)
43
44 KSiOH = Kmi^(-1);
45 fSiOH = cHb*exp(-el/kT*phi0);
46 KSiOH2 = (Kpl*Kmi)^(-1);
```

```
fSiOH2 = fSiOH^2;

% SiO coverage:
thetaSiO = (1-thetaAS)/(1 + KSiOH*fSiOH + KSiOH2*fSiOH2);
% SiOH2 coverage:
thetaSiOH2 = (1-thetaAS)*KSiOH2*fSiOH2/(1 + KSiOH*fSiOH + KSiOH2*fSiOH2);
% Surface charge density in 0-plane:
delta0 = el*GamTot*(thetaSiOH2 + thetaAS - thetaSiO);

function F = Model2pK(phid,phiMidChan,zMat,cizMat,pHb,constant)
% Calculates the zeta potential in the channel
% Input: Start guess on the zeta-potential, mid potential,
%        ionic valence of species, bulk conc. of species, bulk pH,
%        constants.
%% Constants:
epsl = constant(1);     % Permittivity for water. (F/m)
el = constant(2);       % Elementary charge (coulomb)
kT = constant(3);       % Thermal energy (J)
GamTot = constant(4);   % Total number of chargeable sites (m^-2)
NA = constant(5);       % Avogadro's number (particles/mol)
Kpl = constant(6);      % Equilibrium constant
                        % for SiOH2+<-> SiOH + H+ (Molar)
Kmi = constant(7);      % Equilibrium constant for
                        % SiOH <-> SiO- + H+ (Molar)
CTot = constant(11);    % Stern capacitance (F/m^2)
thetaAS = constant(16); % Amino silane coverage

%% Find surface charge:
cHb = 10^(-pHb)*1e3*NA;     % Bulk concentration of H+ (m^-3)
cOHb = 10^(-14+pHb)*1e3*NA; % Bulk concentration of OH- (m^-3)
cizMat = cizMat*1e3*NA;     % Concentration of electrolytes (m^-3)

C = exp(-zMat*el/kT*phiMidChan); % Constant for non zero mid potential.
% Contribution of electrolytes to the sum in delta0:
B = sum(sum( cizMat.*(exp(-zMat*el/kT*phid)-C) ));
% Add contribution of H+ and OH- to the sum in delta0:
B = B + cHb*(exp(-(1)*el/kT*phid)-exp(-(1)*el/kT*phiMidChan))...
    +cOHb*(exp(-(-1)*el/kT*phid)-exp(-(-1)*el/kT*phiMidChan));
% Surface charge density in 0-plane:
delta0 = sign(phid)*sqrt(2*epsl*kT)*(B)^(1/2);
%%
phi0 = phid + delta0/CTot; % Stern capacitance relation

cHb = cHb/(1e3*NA); % -> (Molar)

KSiOH = Kmi^(-1);
fSiOH = cHb*exp(-el/kT*phi0);
KSiOH2 = (Kpl*Kmi)^(-1);
fSiOH2 = fSiOH^2;

% SiO coverage:
thetaSiO = (1-thetaAS)/(1 + KSiOH*fSiOH + KSiOH2*fSiOH2);
% SiOH2 coverage:
thetaSiOH2 = (1-thetaAS)*KSiOH2*fSiOH2/(1 + KSiOH*fSiOH + KSiOH2*fSiOH2);
```

```
% SiOH coverage:
thetaSiOH = (1-thetaAS)*KSiOH*fSiOH/(1 + KSiOH*fSiOH + KSiOH2*fSiOH2);

% The surface charge density expressed by the coverages.
% On the form f(zeta) = 0 to be used in fzero:
F = delta0 - el*GamTot*(thetaSiOH2 + thetaAS - thetaSiO);
```

C.4 MatLab Script for the Metal Adsorption Model

```
function sol = FindZetaMetalModel(x0,zMat,cizMat,pHb,constant)
% Calculates the zeta potential in the channel by using fsolve
% Input: Start guess on the 2 potentials (phi0,phid),
%        ionic valence of species, bulk conc. of species,
%        the bulk pH, constants.
options = optimset('Display','iter','TolFun',1e-10,'TolX',1e-10,...
          'MaxFunEvals',1e25,'MaxIter',1e5,'Diagnostics','off',...
          'LevenbergMarquardt','on','LargeScale','off');
sol = fsolve(@(x0)MetalModel(x0,zMat,cizMat,pHb,constant),x0,options);

function F = MetalModel(x0,zMat,cizMat,pHb,constant)
% Calculates the zeta potential in the channel
% Input: Start guess on the 2 potentials (phi0,phid),
%        ionic valence of species, bulk conc. of species,
%        the bulk pH, constants.
%% Constants:
epsl = constant(1);   % Permittivity for water. (F/m)
el = constant(2);     % Elementary charge (coulomb)
kT = constant(3);     % Thermal energy (J)
GamTot = constant(4); % Total number of chargeable sites (m^-2)
NA = constant(5);     % Avogadro's number (particles/mol)
Kpl = constant(6);    % Equilibrium constant
                      % for SiOH2+<-> SiOH + H+ (Molar)
Kmi = constant(7);    % Equilibrium constant for
                      % SiOH <-> SiO- + H+ (Molar)
KM = constant(8);     % Equilibrium constant for
                      % SiO- + M+ <-> SiOM (Molar^-1)
C1 = constant(10);    % Inner Stern capacitance (F/m^2)
C2 = constant(11);    % Outer Stern capacitance (F/m^2)

%% Startguess
phi0 = x0(1); % phi_0
phid = x0(2); % phi_d

%% Find surface charge density of the diffusion layer:
cHb = 10^(-pHb)*1e3*NA;     % Bulk concentration of H+ (m^-3)
cOHb = 10^(-14+pHb)*1e3*NA; % Bulk concentration of OH- (m^-3)
cizMat2 = cizMat*1e3*NA;    % Concentration of electrolytes (m^-3)
% Contribution of electrolytes to the sum in deltad:
B = sum(sum( cizMat2.*(exp(-zMat*el/kT*phid)-1) ));
% Add contribution of H+ and OH- to the sum in deltad:
```

```
B = B + cHb*(exp(-(1)*el/kT*phid)-1)+cOHb*(exp(-(-1)*el/kT*phid)-1);
% Surface charge density in d-plane:
deltad = sqrt(2*epsl*kT)*(B)^(1/2);
%%
phib = phid - deltad/C2; % Capacitor relation

cHb = cHb/(1e3*NA);             % Bulk concentration of H+ (Molar)
cMb = cizMat2(1,2)/(1e3*NA);    % Bulk concentration of M+ (Molar)

KSiOH = Kmi^(-1);
fSiOH = cHb*exp(-el/kT*phi0);
KSiOM = KM;
fSiOM = cMb*exp(-el/kT*phib);
KSiOH2 = (Kpl*Kmi)^(-1);
fSiOH2 = fSiOH^2;

% The equations to be solved:
F = [ el*GamTot*(KSiOH2*fSiOH2 - 1 - KSiOM*fSiOM)/...              %(Eq. 1)
      (1 + KSiOM*fSiOM + KSiOH*fSiOH + KSiOH2*fSiOH2)-C1*(phi0-phib),...
      deltad + el*GamTot*(KSiOH2*fSiOH2 - 1)/...                   %(Eq. 2)
      (1 + KSiOM*fSiOM + KSiOH*fSiOH + KSiOH2*fSiOH2)];
```

C.5 MatLab Script for Calculating the Weighted pH

```
function [pHcWeight] = Find_pHweighted(zetap,pHb,zMat,cizMat,h,...
                                       lD,IS,constant)
% Calculates the weighted pH for the ionic species and plots the
% Input: The zeta potential, the bulk pH, ionic valence matrix, bulk conc.
%        matrix, channel height, Debye length,
%        ionic strength, vector of constants
% Output: Weighted pH in matrix corresponding to the structure of cizMat
el = constant(2);           % Elementary charge (coulomb)
kT = constant(3);           % Thermal energy (J)

%phiDH = zetap*cosh((z-h/2)/lD)/cosh(h/(2*lD)); % (V)

% Solve the electric potential in the channel:
[zpos,phi1_struct] = potential2ndOrderSolverBVP4C(zetap,pHb,zMat,cizMat,...
h,lD,IS,constant);

% Evaluate potential at positions zpos:
phi = deval(phi1_struct,zpos,1)*(kT/el);

zpos = lD*zpos;  % Rescale z position (m)
% Define potential as a function:
phiF = @(z) deval(phi1_struct,z/lD,1)*(kT/el);

Z = 1; % Ionic valence
% Gouy-Chapman solution of electric potential:
phiGC = 4*kT/(el*Z)*atanh(tanh(Z*el*zetap/(4*kT))*exp(-zpos/lD));
```

```
27
28 figure(1) % Check solved potential with Gouy–Chapman solution
29 plot(zpos,phi,'r.')
30 hold on
31 plot(zpos,phiGC,'g.')
32 hold off
33
34 pHcF = @(z) pHb + el*phiF(z)/(kT*log(10));
35
36 zMatv=zMat(:);
37 for k = 1:length(zMatv)
38     pHcWeight_vec(k) = pHb - ...
39     log10(quad(@(z) exp(-el/kT*(1+zMatv(k))*phiF(z)),0,h/2)./...
40     quad(@(z)exp(-el/kT*zMatv(k)*phiF(z)),0,h/2));
41 end
42 pHcWeight = reshape(pHcWeight_vec,size(zMat,1),size(zMat,2));
43 pHcWeight([cizMat==0]) = NaN;
44
45 plot(zpos,pHcF(zpos),'-r')
```

C.6 MatLab Script for Calculating the Conductance of a Rectangular Nanochannel

```
1  function [phiMidChan, S] = Find_channel_conductance(zetap,pHb,...
2                                      zMat,cizMat,muMat,h,lD,IS,constant)
3  % Solves the potential profile, determines mid channel potential, and
4  % calculates the channel conductance.
5  % Input: The zeta potential, the bulk pH, ionic valence matrix, bulk conc.
6  %        matrix, mobility matrix, channel height, Debye length,
7  %        ionic strength, vector of constants
8  % Output: phiMidChan - mid channel potential
9  %         S - channel conductance
10 epsl = constant(1);     % Permittivity of water (F/m)
11 el = constant(2);       % Elementary charge (coulomb)
12 kT = constant(3);       % Thermal energy (J)
13 NA = constant(5);       % Avogadro's number (particles/mol)
14 w = constant(14);       % Channel width in [m]
15 L = constant(15);       % Channel length in [m]
16 muH=362E-9;             % Mobility of H+  (m^2 V^-1 s^-1)
17 muOH=205E-9;            % Mobility of OH- (m^2 V^-1 s^-1)
18 eta = 1e-3;             % Dynamic viscosity (Pa s)
19
20 % Solve the electric potential in the channel:
21 [zpos,phi1_struct] = potential2ndOrderSolverBVP4C(zetap,pHb,zMat,cizMat,...
22 h,lD,IS,constant);
23
24 % Evaluate potential at positions zpos:
25 phi = deval(phi1_struct,zpos,1)*(kT/el);
26
27 zpos = lD*zpos;  % Rescale z position (m)
```

```
% Define potential as a function:
phiF = @(z) deval(phi1_struct,z/lD,1)*(kT/el);
phiMidChan = phi(end); % Get mid channel potential (V)

Z = 1; % Ionic valence
% Gouy-Chapman solution of electric potential:
phiGC = 4*kT/(el*Z)*atanh(tanh(Z*el*zetap/(4*kT))*exp(-zpos/lD));

figure(1) % Check solved potential with Gouy-Chapman solution
plot(zpos,phi,'r.')
hold on
plot(zpos,phiGC,'g.')
hold off

cHb = 10^(-pHb)*1e3*NA;          % Hydron conc. (H+) (m^3)
cOHb = 10^(-14+pHb)*1e3*NA;      % Hydroxide (OH-) (m^3)
cizMat = cizMat*1e3*NA;          % Bulk conc. of species (m^3)

muv = muMat(:);                  % Mobilities of species (m^2 V^-1 s^-1)
cizMatv = cizMat(:);             % Bulk conc. of species (m^3)
zMatv = zMat(:);                 % Valence of species

B =@(z) 0;
D =@(z) 0;
% Summation over all species:
for k = 1:length(muv)
   B = @(z) B(z) +...
       abs(zMatv(k)*el*muv(k))*cizMatv(k)*exp(-zMatv(k)*el*phiF(z)/kT);
   D = @(z) D(z) +...
       zMatv(k)*el*cizMatv(k)*exp(-zMatv(k)*el*phiF(z)/kT).*(phiF(z)-zetap);
end

% Contribution from H+ and OH-:
B = @(z) B(z) + abs((1)*el*muH)*cHb*exp(-(1)*el*phiF(z)/kT);
B = @(z) B(z) + abs((-1)*el*muOH)*cOHb*exp(-(-1)*el*phiF(z)/kT);
D = @(z) D(z) + (1)*el*cHb*exp(-(1)*el*phiF(z)/kT).*(phiF(z)-zetap);
D = @(z) D(z) + (-1)*el*cOHb*exp(-(-1)*el*phiF(z)/kT).*(phiF(z)-zetap);

sigmaCond = @(z) B(z);           % Conductivity (S/m)
sigmaAdv = @(z) epsl/eta*D(z);   % Advection contribution (S/m)

S = 2*w/L*quad(@(z) sigmaCond(z),0,h/2);
S = S + 2*w/L*quad(@(z) sigmaAdv(z),0,h/2); % Channel conductance (S)
```

C.7 MatLab Script for Calculating the Bulk Conductance

```
function [SBulk,SBulkKCl] = BulkConductance(h,pHb,mu,muH,zMat,cizMat,...
                            constant)
% Calculates the bulk conductance and the KCl bulk conductance
% Input: Channel height, bulk pH, mobilities, mobilities of H+ and OH-,
```

```
%        ionic valence matrix, bulk conc. matrix, vector of constants

el = constant(2); % Elementary charge (coulomb)
kT = constant(3); % Thermal energy (J)
NA = constant(5); % Avogadro's number (particles/mol)
w = constant(14); % Channel width (m).
L = constant(15); % Channel length (m).

cHb = 10^(-pHb)*1e3*NA;     % Hydronium conc. (H+) (m^-3)
cOHb = 10^(-14+pHb)*1e3*NA; % Hydroxide (OH-) conc. (m^-3)
cizMat = cizMat*1e3*NA;     % Bulk conc. of species (m^-3)

cizMatv = cizMat(:);
zMatv = zMat(:);
muv = mu(:);
B = 0;
for k = 1:length(muv)
    B = B + abs(zMatv(k)*el*muv(k))*cizMatv(k);
end
B = B + abs((1)*el*muH(1))*cHb;
B = B + abs((-1)*el*muH(2))*cOHb;
sigma = B;           % Bulk conductivity (S/m)
SBulk = h*w/L*sigma; % Bulk conductance (S)

F = 0;
F = F + abs((1)*el*muv(4))*cizMatv(4);  % Potassium
F = F + abs((-1)*el*muv(2))*cizMatv(2); % Chloride
% Bulk conductivity due to potassium chloride (S/m):
sigmaKCl = F;
% Bulk conductance due to potassium chloride (S):
SBulkKCl = h*w/L*sigmaKCl;
```

C.8 Script for Fitting the 2pK-Model to Conductance Data

```
clc
clear all
close all
format long e

global JJJ dt save_str experimentalist_str xfit_str C2
JJJ = 0; % Initilize iteration counter
dt = datestr(now, 'yyyy-mm-dd_HH-MM');

save_str = 'uncoat';    % String appended to saved data file
% save_str = 'coat';    % String appended to saved data file
% save_str4 = 'Dataset1_165nm';
save_str4 = 'Dataset2_165nm_HCl';
% save_str4 = 'Dataset2_200nm';
% save_str4 = 'Fitte_width_165nm';
% experimentalist_str = '_Dherrick';
```

```
17 experimentalist_str = '_Andrew';
18
19 [C, S] = NCS_fit_exp_inputuncoated; % Import experimental data
20 xdata = C; % Salt concentrations (Molar)
21 ydata = S; % Conductances (S)
22 %%
23 xfit_str = {'_pKminus' '_C2'};
24 %xfit_str = {'_pKminus'};
25 %xfit_str = {'_width'};
26 %xfit_str = {'_C2'};
27
28 %param0 = [6.64];    % Fitting pKminus
29 param0 = [6.64 0.2]; % Fitting pKminus and Cs
30
31 %lb = [-inf];   % Lower bounds on fit parameters (Fitting pKminus)
32 lb = [-inf 0];  % Lower bounds on fit parameters (Fitting pKminus and Cs)
33
34 %ub = [inf];    % Upper bounds on fit parameters (Fitting pKminus)
35 ub = [inf inf]; % Upper bounds on fit parameters (Fitting pKminus and Cs)
36 %%
37
38 % Definition of fitting function:
39 model2pKfit = @(param,xdata)Func2pKmodel(param,xdata,ydata);
40 % Func2pKmodel calculates the conductances from the 2pK-model
41 % The returned conductances are scaled down with log10.
42
43 % Options for fitting function:
44 options = optimset('MaxFunEvals', 2e4, 'MaxIter',1e3, 'display', 'iter',...
45     'TolFun', 1e-8, 'TolX', 1e-8,'Diagnostics','off');
46
47
48 tic;
49 % Fit parameters with lsqcurvefit (fitting in log-space) :
50 [paramfit,resnorm] = lsqcurvefit(model2pKfit,param0,log10(xdata),...
51                                  log10(ydata),lb,ub,options)
52 tiden = toc;
53 hold off
54
55 % Calculate the 2pK-model with the optimal values of the fitting parameters
56 [Snum,parammat,JJJ] = Func2pKmodel(paramfit,log10(xdata),ydata);
57 Snum = 10.^(Snum); % Rescale to conductance from log10(conductance)
58
59 %% Calculate "goodness" of fit
60 SStot_Cond = sum((ydata-mean(ydata)).^2);   % Total sum of squares
61 SSerr_Cond = sum((ydata-Snum).^2);          % Residual sum of squares
62 Rsqua_Cond = 1 - SSerr_Cond/SStot_Cond;     % Coefficient of determination
63 %%
64 save(['Matfiles/' datestr(now, 'yyyy-mm-dd_HH-MM') '_'...
65     save_str experimentalist_str xfit_str{:} '_' save_str4]);
66
67 figure(98)
68 loglog(xdata,Snum,'-b')
69 hold on
70 loglog(xdata,ydata,'.r')
```

```
hold off
saveas(gcf,['Figs/' datestr(now, 'yyyy-mm-dd_HH-MM') '_'...
    save_str experimentalist_str xfit_str{:} '_Figure.fig'])
```

C.9 Main Script for the 2pK-Model

```
% Main script for the 2pK-model:
% Calling the function ElecKinFunctions which returns the zeta potential,
% the mid channel potential, the surface charge density, the bulk pH,
% and the channel conductance.
clear all;
close all;
clc;
format long e

%% INPUT DATA
% (ionic valence, mobility, pKa, ionic valence, Mobility, pKa, ...)
INP={
    [       1   76.2E-9   13.7                          ]; % Potasium (KOH)
    %[       1   51.9E-9   13.7                          ]; % Sodium (NaOH)
    [      -1   79.1E-9   -7                            ]; % HCl
    [      -1   46.1E-9   6.352    -2   71.8E-9  10.33   ]; % CO2
    };

%% CONSTANTS
eps0 = 8.85e-12;            % Permittivity of vacuum (F/m)
epsr = 78;                  % Relative permittivity of water
epsl = epsr*eps0;           % Permittivity of water (F/m)
el = 1.602e-19;             % Elementary charge (coulomb)
kT = 0.0259*el;             % Thermal energy (J)
GamTot = 5/(1e-9)^2;        % Total number of chargeable sites (m^-2)
NA  = 6.022e23;             % Avogadro's number (particles/mol)
Kw=1E-14;                   % Self-ionization constant of water (Molar^2)
Kpl = 10^(1.64);            % Equilibrium constant
                            % for SiOH2+<-> SiOH + H+ (Molar)
Kmi = 10^(-6.64);           % Equilibrium constant for
                            % SiOH <-> SiO- + H+ (Molar)
pHpzc = -1/2*(log10(Kpl)+log10(Kmi)); % Point of zero charge
Cs = 0.2;                   % Stern capacitance (F m^-2)
thetaAS = 0.0;              % Aminosilane coverage
%%

%% Channel dimensions:
h = 200e-9;                 % Channel height in [m]
L = 1.2e-2;                 % Channel length in [m]
w = 5e-6;                   % Channel width in [m]

constant = [epsl, el, kT, ...
            GamTot, NA, Kpl, ...
            Kmi, NaN, NaN,...
```

```
45              NaN, Cs, Kw, ...
46              pHpzc,w,L,thetaAS];
47
48  c_CO2 = 1.18*10^(-5);       % Formal concentration of H2CO3 at 25 degrees C
49                              % at normal atm. pressure (Molar)
50  cHCl = 0;                   % HCl conc. added (Molar)
51  cvec = logspace(-7,0,50);   % KCl conc. vector (Molar)
52
53  cvec = flipdim(cvec,2);             % Reverse conc. vector
54  Svec = zeros(length(cvec),1);       % Init conductance vector
55  Zetavec = zeros(length(cvec),1);    % Init zeta portential vector
56
57  %% Optimal guess for model 2pK model for 1 M KCl:
58  zetap0 = -1.94e-02; %
59
60  for g = 1:length(cvec);
61      cTot = [cvec(g) (cvec(g)+cHCl) c_CO2]; % Solutes conc. vector (Molar)
62
63      % Calculate the zeta potential assuming phi_m = 0
64      [zetap0 ,phiMidChan, delta0, pHb ,S] =...
65          ElecKinFunctions(INP,cTot,constant,h,zetap0,0);
66
67      zetap = zetap0;
68      % Debye Overlap correction:
69      phiMidChanB = 100;  % Initial dummy value of phi_m (V)
70      tole = 1e-4;        % Tolerance for convergence of phi_m
71      while abs((phiMidChan-phiMidChanB)) > tole
72          phiMidChanB = phiMidChan;
73          [zetap ,phiMidChan, delta0, pHb ,S] =...
74          ElecKinFunctions(INP,cTot,constant,h,zetap,phiMidChan);
75      end
76
77      Zetavec(g) = zetap;     % Store solved zeta potential (V)
78      Delta0vec(g) = delta0;  % Store solved surface charge density (C m^2)
79      Svec(g) = S;            % Store calc. channel conductance (S)
80  end
81
82  function [zetap ,phiMidChan, delta0, pHb, S] = ElecKinFunctions(...
83      INP,cTot,constant,h,x01,phiMidChan)
84
85  % Calling the (original) Santiago script:
86  [cH,zMat,muMat,muEffVec,cizMat]  =  Santiago(INP,cTot);
87
88  pHb = -log10(cH);
89  F=9.65E4;
90  muMat = muMat*F;
91  % Calculating the Debye length:
92  [lD IS]             =  DebyeLength(pHb,zMat,cizMat,constant);
93
94  % Solving for the zeta potential in the 2pK-model:
95  [zetap, delta0]     =  Find_zeta_2pKmodel(x01,phiMidChan,cizMat,zMat,...
96                          pHb,constant);
97  % Calculate channel conductance:
98  [phiMidChan, S]     =  Find_channel_conductance(zetap,pHb,zMat,cizMat,...
```

```
                        muMat,h,lD,IS,constant);

function [lD IS] = DebyeLength(pHb,zMat,cizMat,constant)
% Calculates the Debye length
% Input: bulk pH, ionic valence of species, bulk conc. of species,constants
epsl = constant(1);    % Permittivity for water (F/m).
el = constant(2);      % Elementary charge (coulomb)
kT = constant(3);      % Thermal energy (J)
NA = constant(5);      % Avogadro's number (particles/mol)

% Hydron (H+) and hydroxide (OH-) conc. in reservoir
cHb = 10^(-pHb)*1e3*NA;          % (m^-3)
cOHb = 10^(-14+pHb)*1e3*NA;      % (m^-3)

cizMat = cizMat*1e3*NA;          % Bulk conc. of species (m^-3)
ISd = sum(sum( cizMat.*zMat.^2 ));
ISd = ISd + cHb*(1)^2 + cOHb*(1)^2;

IS =ISd/2;                       % Ionic strength (m^-3)

lD = sqrt(epsl*kT/(2*el^2*IS)); % Debye length (m)
```

C.10 Main Script for the Metal Adsorption Model

```
% Main script for the Metal Absorbtion Model:
% Calling the function ElecKinFunctions which returns the zeta potential,
% the bulk pH, and the Weighted pH for the species.
clear all;
close all;
clc;
format long e

%% INPUT DATA
% (ionic valence, pKa, ionic valence, pKa, ...)
INP={
[   1       13.7                                    ];  % NaOH
%[   -1      -7                                      ];  % HCl
[   -1      6.352    -2     10.33                   ];  % CO2
[    -1 9.24 -2 12.74  -3 13.8                      ];  % Borate
% [ 1  8.076                                        ];  % TRIS
};

c_CO2 = 1.18*10^(-5);       % Formal concentration of H2CO3 at 25 degrees C
                            % at normal atm. pressure (Molar)
c_Titration = 23.3e-3;      % Formal concentration of titrate (Molar)
c_Buffer = 50e-3;           % Formal concentration of buffer (Molar)

%% CONSTANTS
eps0 = 8.85e-12;        % Permittivity of vacuum (F/m)
epsr = 78;              % Relative permittivity of water
```

```
epsl = epsr*eps0;       % Permittivity of water (F/m)
el = 1.602e-19;         % Elementary charge (coulomb)
kT = 0.0259*el;         % Thermal energy (J)
GamTot = 5/(1e-9)^2;    % Total number of chargeable sites (m^-2)
NA  = 6.022e23;         % Avogadro's number (particles/mol)
pHpzc = 2.5;            % Point of zero charge
Kmi = 10^(-6.73);           % Equilibrium constant for
                            % SiOH <-> SiO- + H+ (Molar)
Kpl = 10^(-2*pHpzc)/Kmi;    % Equilibrium constant
                            % for SiOH2+<-> SiOH + H+ (Molar)
KM  = 10^(-0.25);           % Equilibrium constant for
                            % SiO- + M+ <-> SiOM (Molar^-1)
KW  = 1e-14;                % Water equilibrium constant
C1 = 1.07;               % Inner Stern capacitance (F m^-2)
C2 = 0.2;                % Outer Stern capacitance (F m^-2)

%% Channel dimensions:
h = 100e-9;    % Channel height in [m]

%% Formal concentrations of species(Molar)
cTot = [c_Titration c_CO2 c_Buffer];

cMb = cTot(1); % Formal concetration of the solute dissociating into
               % metal cations e.g. NaOH -> Na+ or KCl -> K+

constant = [epsl, el, kT, ...
                    GamTot, NA, Kpl, ...
                    Kmi, KM, cMb,...
                    C1, C2, KW, ...
                    pHpzc]; %Entry 9: cMb = cTot(1)

if size(INP,1) ≠ length(cTot)
    error('Concentrations for exact number of species must be given.')
    % Error when INP and cTot do have the same number of species.
end

%% Optimal guess for Metal Absorbtion Model:
 x0 = [-2.620366645735209e-001   -1.188386998748549e-001]; %psi0, psid

[zetap, pHb, pHcWeight] = ElecKinFunctions(INP,cTot,constant,h,x0);

function [zetap, pHb, pHcWeight] = ...
    ElecKinFunctions(INP,cTot,constant,h,x0)

% Calling the modified Santiago script:
[pHb,zMat,cizMat] = Santiago_pHb(INP,cTot,constant(12))

% Calculating the Debye length:
[lD, IS] = DebyeLength(pHb,zMat,cizMat,constant);

% Solving for the phi0 and phid potential in the metal adsorption model:
sol = FindZetaMetalModel(x0,zMat,cizMat,pHb,constant)

zetap = sol(2); % zeta potential (V)
```

```
81
82 % Calculating the Weighted pH for the species:
83 pHcWeight = Find_pHweighted(zetap,pHb,zMat,cizMat,h,lD,IS,constant)
84
85 function [zetap, pHb, pHcWeight] = ...
86     ElecKinFunctions(INP,cTot,constant,h,x0)
87
88 % Calling the modified Santiago script:
89 [pHb,zMat,cizMat] = SantiagoMADS(INP,cTot,constant(12));
90
91 % Calculating the Debye length:
92 [lD, IS] = DebyeLength(pHb,zMat,cizMat,constant);
93
94 % Solving for the phi0 and phid potential in the metal absorbtion model:
95 sol = FindZetaMetalModel(x0,zMat,cizMat,pHb,constant)
96
97 zetap = sol(2); % Zeta potential (V)
98
99 % Calculating the Weighted pH for the species:
100 pHcWeight = Find_pHweighted(zetap,pHb,zMat,cizMat,h,lD,IS,constant)
101 end
102
103 function [lD IS] = DebyeLength(pHb,zMat,cizMat,constant)
104 % Calculates the Debye length
105 % Input: bulk pH, ionic valence of species, bulk conc. of species,constants
106 epsl = constant(1);    % Permittivity for water (F/m).
107 el = constant(2);      % Elementary charge (coulomb)
108 kT = constant(3);      % Thermal energy (J)
109 NA = constant(5);      % Avogadro's number (particles/mol)
110
111 % Hydron (H+) and hydroxide (OH−) conc. in reservoir
112 cHb = 10^(−pHb)*1e3*NA;         % (m^−3)
113 cOHb = 10^(−14+pHb)*1e3*NA;     % (m^−3)
114
115 cizMat = cizMat*1e3*NA;         % Bulk conc. of species (m^−3)
116 ISd = sum(sum( cizMat.*zMat.^2 ));
117 ISd = ISd + cHb*(1)^2 + cOHb*(1)^2;
118
119 IS =ISd/2;                      % Ionic strength (m^−3)
120
121 lD = sqrt(epsl*kT/(2*el^2*IS)); % Debye length (m)
```

Bibliography

[1] W. Sparreboom, A. van den Berg, and J. C. T. Eijkel,
Transport in nanofluidic systems: a review of theory and applications,
New J. Phys. **12**, 015004 (23 pp.) (2010).

[2] F. H. J. van der Heyden, D. J. Bonthuis, D. Stein, C. Meyer, and C. Dekker,
Electrokinetic energy conversion efficiency in nanofluidic channels,
Nano Lett. **6**, 2232–2237 (2006).

[3] F. H. J. van der Heyden, D. J. Bonthuis, D. Stein, C. Meyer, and C. Dekker,
Power generation by pressure-driven transport of ions in nanofluidic channels,
Nano Lett. **7**, 1022–1025 (2007).

[4] S. Pennathur, J. C. T. Eijkel, and A. van den Berg
Energy conversion in microsystems: is there a role for micro/nanofluidics.,
Lab on a Chip **7**, 1234-1237 (2007).

[5] R. Charmas, W. Piasecki, and W. Rudziński,
Four layer complexation model for ion adsorption at electrolyte/oxide interface: Theoretical foundations,
Langmuir **11**, 3199–3210 (1995).

[6] A. Persat, R. D. Chambers, and J. G. Santiago,
Basic principles of electrolyte chemistry for microfluidic electrokinetics. Part I: Acid–base equilibria and pH buffers,
Lab on a Chip **9**, 2437–2453 (2009).

[7] Staffan W. *The history of electrokinetic phenomena* Department of Chemistry/Physical Chemistry, University of Gothenburgh, SE 412 96 Gothenburgh, Sweden.

[8] O. Stern,
Z. Electrochem. **30**, 508 (1924).

[9] D. E. Yates, S. Levine, and T. W. Healy,
Site-binding model of the electrical double layer at the oxide/water interface,
J. Chem. Soc., Faraday Trans. 1 **70**, 1807–1818 (1974).

[10] D. Chan, J. W. Perram, L. R. White, and T. W. Healy,
Regulation of surface potential at amphoteric surfaces during particle-particle interaction,
J. Chem. Soc., Faraday Trans. 1 **71**, 1046–1057 (1975).

[11] J. W. Bowden, S. Nagarajah, N. J. Barrow, A. M. Posner, and J. P. Quirk
Describing the adsorption of phosphate, citrate and selenite on a variable-charge mineral surface,
Australian Journal of Soil Research **18**, 49–60 (1980).

[12] J. W. Bowden, A. M. Posner, and J. P. Quirk,
Soils with variable charge,
B. K. G. Theng Ed. New Zealand Society of Soil Science: Lower Hutt, 147 (1980).

[13] L. Bousse, N. F. de Rooij, and P. Bergveld,
The influence of counter-ion adsorption on the ψ_0/pH characteristics of insulator surfaces,
Surf. Sci. **135**, 479–496 (1983)

[14] Link to Santiago script (buffer calculator):
`http://microfluidics.stanford.edu/download/index.html`
(visited 15 June 2010).

[15] C. W. Davies,
The extent of dissociation of salts in water.
Part VIII. An equation for the mean ionic activity coefficient of an electroltye in water, and a revision of the dissociation constants of some sulphates,
J. Chem. Soc. **397**, 2093–2098 (1938).

[16] M. Wang and A. Revil,
Electrochemical charge of silica surfaces at high ionic strength in narrow channels,
J. Colloid Interface Sci. **343**, 381–386 (2010).

[17] H. S. Harned and R. Davis Jr.,
The ionization constant of carbonic acid in water and the solubility of carbon dioxide in water and aqueous salt solutions from 0 to 50°,
J. Am. Chem. Soc. **65**, 2030–2037 (1943).

[18] Link to different bond types on an amorphous silica surface:
`http://hplccourse.com/Silicasurface.php`
(visited 19 June 2010).

[19] T. Jesionowski
Influence of aminosilane surface modification and dyes adsorption on zeta potential of spherical silica particles formed in emulsion system,
Colloids and Surfaces A: Physicochemical and Engineering Aspects **222**, 87-94 (2003).

[20] W. Rudzinski, R. Charmas, J. M. Cases, M. Francois, F. Villieras, and L. J. Michot, *Calorimetric effects and temperature dependence of simple ion adsorption at oxide-electrolyte interface: A theoretical analysis based on the triple-Layer complexation model*,
Langmuir **13**, 483–495 (1997).

[21] D. Stein, M. Kruithof, and C. Dekker,
Surface-charge-governed ion transport in nanofluidic channels,
Phys. Rev. Lett. **93**, 035901 (23 pp.) (2004).

[22] K. D. Huang and R. J. Yang,
Electrokinetic behaviour of overlapped electric double layers in nanofluidic channels,
Nanotechnology **18**, 115701 (6 pp.) (2007).

[23] S. H. Behrens and D. G. Grier,
The charge of glass and silica surfaces,
J. Chem. Phys. **115**, 6716–6721 (2001).

[24] M. S. Kilic, M. Z. Bazant, and A. Ajdari,
Steric effects in the dynamics of electrolytes at large applied voltages. I. Double-layer charging,
Phys. Rev. E **75**, 021502 (16 pp.) (2007).

[25] P. Pham, M. Howorth, A. Planat-Chrétien, and S. Tardu,
Numerical Simulation of the Electrical Double Layer Based on the Poisson–Boltzmann Models for AC Electroosmosis Flows,
Excerpt from the Proceedings of the COMSOL Users Conference 2007 Grenoble.

[26] A. Persat, M. E. Suss, and J. G. Santiago,
Basic principles of electrolyte chemistry for microfluidic electrokinetics. Part II: Coupling between ion mobility, electrolysis, and acid–base equilibria,
Lab on a Chip **9**, 2454–2469 (2009).

[27] R. A. Robinson and R. H. Stokes,
Electrolyte solutions,
Butterworths Scientific Publications, London (1959).

[28] B. E. Conway,
Electrochemical data,
Elsevier Pub. Co., Amsterdam (1952) .

[29] D. R. Lide,
CRC Handbook of chemistry and physics, 87th Edition,
CRC Press/-Taylor and Francis, Boca Raton, FL (2006).

[30] P. W. Atkins,
Physical chemistry, 5th edn.,
Oxford Univeristy Press, Oxford (1994).